MASARYKOVA UNIVERZITA
Přírodovědecká fakulta
Ústav teoretické fyziky a astrofyziky

Diplomová práce

Brno 2024 **Mária Lauková**

MASARYKOVA
UNIVERZITA
PŘÍRODOVĚDECKÁ FAKULTA
ÚSTAV TEORETICKÉ FYZIKY A ASTROFYZIKY

Spektroskopické studium promměnných bílých trpaslíků dalekohledy VLT

Diplomová práce

Mária Lauková

Vedoucí práce: prof. Mgr. Jiří Krtička, Ph.D., Brno 2024

Bibliografický záznam

Autor:	Mária Lauková Přírodovědecká fakulta, Masarykova univerzita Ústav teoretické fyziky a astrofyziky

Název práce:	Spektroskopické studium promněnných bílých trpaslíků dalekohledy VLT
Studijní program:	Fyzika
Studijní obor:	Astrofyzika
Vedoucí práce:	prof. Mgr. Jiří Krtička, Ph.D.,
Akademický rok:	2023/2024
Počet stran:	xiv + 87
Klíčová slova:	bílý trpaslík; dvojhvězdy; spektroskopie; radiální rychlost

Bibliographic Entry

Author:	Mária Lauková Faculty of Science, Masaryk University Department of Theoretical Physics and Astrophysics

Title of Thesis:	Spectroscopic study of variable white dwarfs using VLT telescopes
Degree Programme:	Physics
Field of Study:	Astrophysics
Supervisor:	prof. Mgr. Jiří Krtička, Ph.D.,
Academic Year:	2023/2024
Number of Pages:	xiv + 87
Keywords:	white dwarf; binary stars; spectroscopy; radial velocity

Abstrakt

V této diplomové práci jsme se věnovali analýze spekter dvou hvězd patřících k bílým trpaslíkům. Konkrétně se jednalo o hvězdy s označením BD+08 102 a GD 803. Tyto hvězdy byly naším předmětem zájmu díky jejich předchozí fotomerické analýze, která odhalila jejich pravidelnou světelnou proměnnost. Vysvětlením této proměnnosti by mohl být dvouhvězdný charakter. V této práci jsme provedli spektrální analýzu, abychom odhalili pravděpodobnou příčinu této proměnnosti. Analyzovaná spekra byla zhotovena dalekohledy VLT na Evropské jižní observatoři. Při studiu dvouhvězdného charakteru jsme sestrojili křivky radiálních rychlostí a diskutovali jejich možnou proměnnost.

Abstract

In this diploma thesis, we analyzed the spectra of two stars identified as white dwarfs. Specifically, the white dwarfs with identifiers BD+08 102 and GD 803. These stars were of interest to us due to their previous photomeric analysis, which revealed their regular luminosity variability. Binary origin of these stars could be the explanation of these photometric changes. In this work we performed spectral analysis to reveal the probable cause of the light variability. The analyzed spectra were taken by the VLT telescopes at the European Southern Observatory. While studying the binary character we constructed radial velocity curves and discussed their possible variability.

MUNI
SCI

MASARYKOVA UNIVERZITA
PŘÍRODOVĚDECKÁ FAKULTA
KOTLÁŘSKÁ 2, 611 37 BRNO
IČ: 00216224
DIČ: CZ00216224

ZADÁNÍ
DIPLOMOVÉ PRÁCE

Akademický rok: 2023/2024

Ústav:	Ústav teoretické fyziky a astrofyziky
Studentka:	Bc. Mária Lauková
Program:	Fyzika
Specializace:	Astrofyzika

Ředitel *ústavu* PřF MU Vám ve smyslu Studijního a zkušebního řádu MU určuje diplomovou práci s názvem:

Název práce:	Spektroskopické studium proměnných bílých trpaslíků dalekohledy VLT
Název práce anglicky:	Spectroscopic study of variable white dwarfs using VLT telescopes
Jazyk závěrečné práce:	angličtina

Oficiální zadání:
Analýza družicové fotometrie odhaluje desítky bílých trpaslíků jenž vykazují pravidelnou fotometrickou proměnnost. Pravděpodobným vysvětlením proměnnosti mnohých z těchto trpaslíků je přítomnost druhé složky gravitačně svázané s bílým trpaslíkem. Cílem diplomové práce je podrobné studium spektroskopie fotometricky proměnných bílých trpaslíků, kteří jsou možnými složkami dvojhvězdy. Pro studium budou využita spektra získané dalekohledy VLT Evropské jižní observatoře. Bude provedena analýza proměnnosti radiálních rychlostí těchto trpaslíků a bude ověřeno, zda jsou složkami dvojhvězd a zda jejich proměnnost může být způsobena interakcí složek.

Literatura

- Hilditch, R. W., An introduction to close binary stars, Cambridge University Press, 2001
- Krtička, J. a kol., EPIC 206197016: A very hot white dwarf orbited by a strongly irradiated red dwarf, Astronomy & Astrophysics, v přípravě
- Lauková, M., Hledání rotačně proměnných bílých trpaslíků v datech z družice TESS, bakalářská práce, Masarykova univerzita, 2022

Vedoucí práce:	prof. Mgr. Jiří Krtička, Ph.D.
Konzultant:	RNDr. Jan Janík, Ph.D.
Datum zadání práce:	21. 11. 2022
V Brně dne:	13. 3. 2024

Zadání bylo schváleno prostřednictvím IS MU.

Bc. Mária Lauková, 21. 11. 2022
prof. Mgr. Jiří Krtička, Ph.D., 30. 11. 2022
Mgr. Dušan Hemzal, Ph.D., 5. 12. 2022

Poděkování

Moja vďaka na prvom mieste patrí vedúcemu mojej diplomovej práce prof. Mgr. Jiřímu Krtičkovi, Ph.D. za ochotu, čas a rady, ktoré mi venoval pri písaní mojej diplomovej práce. Spektroskopické dáta k mojej diplomovej práci boli získané na základe návrhu ESO 0103.D-0194(A), preto by som sa na tomto mieste chcela poďakovať aj im za možnosť spracovať dáta v rámci tejto diplomovej práce. Poďakovať by som sa chcela aj mojej rodine a blízkym za podporu a povzbudenie.

Prohlášení

Prohlašuji, že jsem svoji diplomovou práci vypracovala samostatně pod vedením vedoucího práce s využitím informačních zdrojů, které jsou v práci citovány.

Brno 04.května 2024 .....

Mária Lauková

Contents

Introduction

White dwarfs are remnants of stars which have exhausted their fuel for fusion. These stars, which are in their final stage of evolution are slowly cooling over time as they radiate away their residual thermal energy. The remnant in the form of white dwarf has a large density and consist of electron degenerate matter. The upper limit for their mass was derived in the 1930's by scientist Chandrasekhar and it is equal to 1.4 $M_{\odot}$ (Shapiro et al., 1983 [36]). White dwarfs were originally found as companions of bright stars (e.g. Sirius B). The study of white dwarfs is an important tool for revealing and understanding the evolution, structure and history of most stars (Toonen et al., 2017 [38]).

Chapter 1

Physics of binary star systems

A significant fraction of the stars in the Sun's proximity are in fact members of binary star systems. Such stars are gravitationally bound and are orbiting each other around the common centre of gravity. There are also systems which are composed of three or more stars. In order for these stars to be stable, they need to form close binary system with the third or fourth component orbiting around the binary. Thus, the binary star system is fundamental even in multiple star systems (Mikulášek & Krtička, 2005 [28]).

1.1 Classification of binary star systems

The binary star systems can be divided into four categories according to the way they have been observed:

1. visual binaries (observed optically using telescope or interferometer),
2. astrometric binaries (deviation in star's position),
3. spectroscopic binaries (periodic changes of position of spectral lines),
4. photometric binaries (changes in star brightness),

(Mikulášek & Krtička, 2005 [28]).

1.1.1 Visual binaries

The first discoveries of binary stars are dated to the 17th century, when Galileo Galilei and Benedetto Castelli found series of binary star systems. They made this happen through telescope observations. The observation is limited due to resolution of telescope 1.1. The equation is comparing the angular resolution of the observational instrument η, with the wavelength of monochromatic radiation, which we see from distant object λ and D the diameter of the instrument

$$\eta = 1.22\frac{\lambda}{D}. \tag{1.1}$$

Ground based observations of distant objects with telescopes are negatively infulenced by effect called seeing. This phenomenon is caused by the motion of the air in the earth atmosphere and dramatically reduces the resolution of the telescope. There are in fact

ways to improve this effect, for example by using the active optics or space observations (Mikulášek & Krtička, 2005 [28]).

1.1.2 Astrometric binaries

The astrometric binaries are resolved as binaries by deviations of proper motion of one of the star components. In some cases there is a binary system in which one of the components has lower mass and it does not radiate as much as its companion. Thus we can not detect the star by visual method. When studying the proper motion of stars we expect the motion to be uniform and straightforward. In the case of another "invisible" companion, the proper motion shows deviations from the uniform and straightforward motion (Mikulášek & Krtička, 2005 [28]).

1.1.3 Spectroscopic binaries

Spectroscopic binaries are detected by studies of stellar spectra. The first spectroscopic binaries were discovered by Maury and Pickering in the 19th century, while studying the spectra of Mizar. It was noticed that the spectra of Mizar has doubled spectral lines. These changes in spectra occured with period of 20 days. Later it was confirmed that this happened due to Doppler effect of orbital motion of the two stellar components (Mikulášek & Krtička, 2005 [28]).

1.1.4 Photometric binaries

The photometric binaries are a type of binary systems discovered thanks to light variations. The first discovered system of this type was Algol (β Per). Light curve of eclipsing binary can be seen in Fig.1.1. The effect which needs to be considered in interpretation of the light curve of binary star systems is limb darkening. The radiation emitted from stellar source vary in respect to the depth from which we see the radiation. From the observer point of view the central part of the stellar disk appears to be hotter than the edge. And thus it comes to the limb darkening of the stellar disc (Mikulášek & Krtička, 2005 [28]).

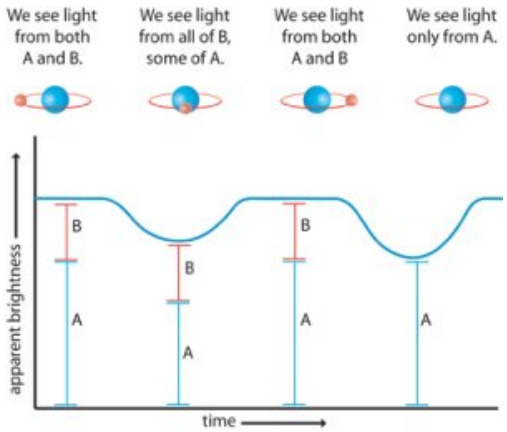

Figure 1.1: Light curve of eclipsing binary [credit: ESA [E16]].

1.2 Effects of photometric variability in close binaries

The close binaries are star systems in which the two star components can interact with each other. The interaction between the components is gravitational as well as radiative. The objects in such system can be close enough to fill their effective potential surface and the mass accretion can be triggered. There are several effects which take place in the physical description of interacting binaries such as tidal deformation, reflection effect and Doppler beaming (Mikulášek & Zejda, 2013 [29]).

The gravitational interaction in close binaries results in deformation of the shape of the star components. Due to this interaction the stars are altered into drop like shapes rather then the standard spherical surface. The radiation of the star depends on the gravitational acceleration, which is not constant among the irregularly shaped object. Thus the binary shows light variability due to the tidal deformation of the star shape (Mikulášek & Zejda, 2013 [29]). This effect is also referred to as ellipsoidal variability.

An another important effect that leads to light variability of binary stars is the reflection effect. In the binary star system, there are two radiating components. Lets assume there is one star A and the other star B, star A emits electromagnetic radiation into its surroundings and illuminates part of the star B. This radiation will be partially dispersed and consequently emitted in the photosphere of star B and partially absorbed by the neighbour star B. The consequence of this effect is that the near sides of the stars are always radiating more than their far sides. As the system rotates, different parts of the stars are visible from the observer point of view and the periodic light variability is seen in the light curve (Mikulášek & Zejda, 2013 [29]).

Doppler beaming or relativistic beaming is an effect during which the luminosity of the star is changing due to orbital motion around the center of mass. This effect was first mentioned in the late 20th century by Hills & Dale (Hills & Dale, 1974 [15]). The stars are orbiting and the flux from the part of the object which is moving towards the observer appears to be higher than the flux from the part which is moving away respectively to the observer (Groot, 2012 [13]). In binary star system this effect is applied thanks to the line-of-sight motion of its components. In the case of the binaries with period $P > 10$ days, the effect of Doppler beaming is more significant than reflection effect and ellipsoidal effect (Zucker et.al., 2007 [40]).

1.3 The Two-body Problem

The motion in binary system can be approximated by solving the two body problem. Lets assume we have two bodies with mass m_1 and m_2 and the positional vectors with the origin in the common centre of gravity are $\mathbf{r_1}$ and $\mathbf{r_2}$ (Benacquista, 2013 [7]). The schematic visualisation can be seen in Fig. 1.2.

The barycentric coordinate system gives

$$m_1\mathbf{r_1} + m_2\mathbf{r_2} = 0. \tag{1.2}$$

The relative separation is

$$\mathbf{r} = \mathbf{r_1} - \mathbf{r_2}. \tag{1.3}$$

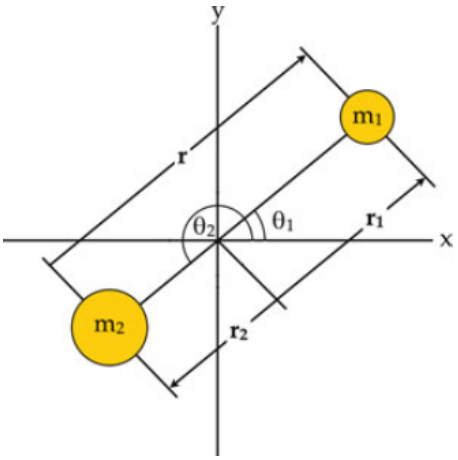

Figure 1.2: Barycentric coordinate description of a binary system [Benacquista, 2013 [7]].

For $\mathbf{r_1}$ and $\mathbf{r_2}$ we can write using equations 1.2 and 1.3

$$\mathbf{r_1} = \frac{m_2}{M}\mathbf{r}, \tag{1.4}$$

$$\mathbf{r_2} = -\frac{m_1}{M}\mathbf{r}, \tag{1.5}$$

where $M = m_1 + m_2$.

The motion of two bodies is found from Lagrangian $\mathscr{L}$

$$\mathscr{L} = \frac{1}{2}m_1 v_1^2 + \frac{1}{2}m_2 v_2^2 + \frac{Gm_1m_2}{|\mathbf{r_1} - \mathbf{r_2}|}. \tag{1.6}$$

From the figure 1.2 we can express θ_1 as $\theta_1 = \theta_2 - \pi = \theta$, since π is constant angle in radians $\dot{\theta}_1 = \dot{\theta}_2 = \dot{\theta}$,

$$v_1^2 = \dot{r_1^2} + r_1^2\dot{\theta_1^2} = \left(\frac{m_2}{M}\right)^2(\dot{r^2} + r^2\dot{\theta^2}), \tag{1.7}$$

$$v_2^2 = \dot{r_2^2} + r_2^2\dot{\theta_2^2} = \left(\frac{m_1}{M}\right)^2(\dot{r^2} + r^2\dot{\theta^2}). \tag{1.8}$$

For Lagrangian we then have

$$\mathscr{L} = \frac{1}{2}\frac{m_1m_2^2}{M^2}(\dot{r^2} + r^2\dot{\theta^2}) + \frac{1}{2}\frac{m_2m_1^2}{M^2}(\dot{r^2} + r^2\dot{\theta^2}) + \frac{Gm_1m_2}{r}, \tag{1.9}$$

$$\mathscr{L} = \frac{1}{2}\frac{m_1m_2}{M}\dot{r^2} + \frac{1}{2}\frac{m_1m_2}{M}r^2\dot{\theta^2} + \frac{Gm_1m_2M}{Mr}. \tag{1.10}$$

We will mark $\frac{m_1m_2}{M} = \mu$ which is reduced mass

$$\mathscr{L} = \frac{1}{2}\mu\dot{r^2} + \frac{1}{2}\mu r^2\dot{\theta^2} + \frac{G\mu M}{r}. \tag{1.11}$$

From the equation 1.11, we can see that the two-body problem is reduced to the solution of motion of one body mass μ in central force field with potential $V(r) = -\frac{GM}{r}$. So, the potential energy is proportional to $\propto \frac{1}{r}$. This is known as the Keppler problem. The solution for Lagrange equation for elliptic orbits is

$$r = \frac{a(1-e^2)}{1+e\cos\theta}, \tag{1.12}$$

where a is the semimajor axis, defined as $a = \frac{l}{(1-e^2)}$, l is semilatus rectum and e is eccentricity which is describing the deviation from the circular shape (Nipoti, 2018 [31]).

1.4 The Roche model

In this section we will study the gravitational potential around binary system in non-inertial rotating frame. We assume that the bodies move in circular orbits. Another assumption is that in the system there is a fictional third body and its mass is negligible in relation to the masses of the two body system m_1 and m_2. The rotational frequency of such system is

$$\omega = \sqrt{\frac{G(m_1+m_2)}{a^3}}. \tag{1.13}$$

In the equation 1.13 there is a quantity a, which represents the distance from one point of mass m_1 to the second body m_2 .

The potential of such system consists of sum of three components proportional to potential of body m_1, potential of body m_2 and the fictional centrifugal force potential.

$$\Phi = \frac{Gm_1m}{r_1} + \frac{Gm_2m}{r_2} + \frac{1}{2}m\omega^2(x^2+y^2) \tag{1.14}$$

The r_1 and r_2 in the equation 1.14 are the distances from the fictional body to the bodies m_1 and m_2.

The equipotential surfaces are calculated by determining the points in which the potential Φ is constant. The figure 1.3 shows the cross section of equipotential surfaces in orbital plane. The inner surface called Roche surface is crucial in understanding the process of the mass transfer within the binary star systems (Benacquista, 2013 [7]).

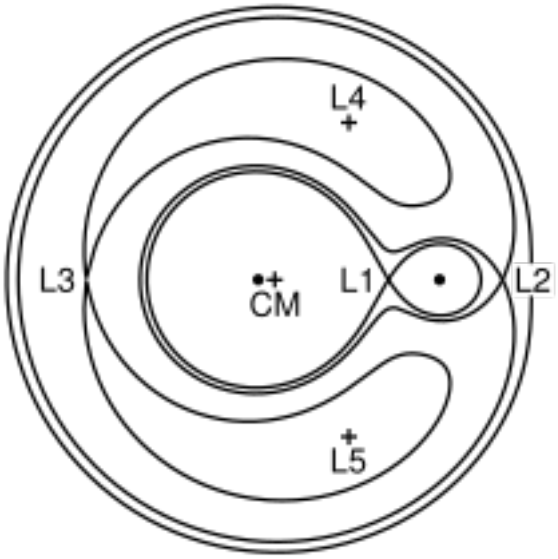

Figure 1.3: Contours of the Roche equipotentials in an equatorial plane of the binary. L_1 - L_5 are Lagrange points and CM is common centre of the mass [Hall, 2016 [E17]].

Chapter 2

Evolution of stars in binary systems

A significant number of stars are found in binary systems and approximately 50 % of such binaries are close enough to start the mass accretion from one star component to the other in the future. This can happen in all different kinds of binary systems, e.g. two non-degenerate stars, one compact star/object (white dwarf, neutron star, black hole) and one normal star or even double degenerate systems (Podsiadlowski, 2012 [32]).

2.1 The Roche Lobes

Assume we have a binary system with circular orbit, we will describe this system in a non-inertial coordinate system that rotates along with the objects or so called comoving frame. In such system we can define an effective potential as mentioned above in previous chapter 1.4. This potential has five points where the gradient of the effective potential is equal to zero. These points are called the Lagrange points. In the figure 2.1 we can see the Lagrange points, points L_1, L_3 and L_2 are laying along the line that connects the two stars. The point L_1 plays an important role in matter accretion, since this point connects the gravitational influence of the two stars. The mechanism of mass flow lays in the filling of so called Roche lobe of one star. If this lobe is fully filled mass transfer from one star to the other through the Lagrange point L_1 can occur. This is called Roche-lobe overflow (Podsiadlowski, 2012 [32]).

According to how stars fill their Roche lobes we can divide binaries into three categories:

1. detached binaries (both stars underfill their Roche lobes) - no mass transfer,
2. semi-detached binaries (one star fills its Roche lobe) - mass transfer,
3. contact binaries (both stars fill their Roche lobes) - when stars fill their Roche lobes, a common envelope is formed. If the common envelope is big enough to reach Lagrange point L_2 the mass can flow out of this point and therefore form a circumbinary disc around the binary system (Podsiadlowski, 2012 [32]).

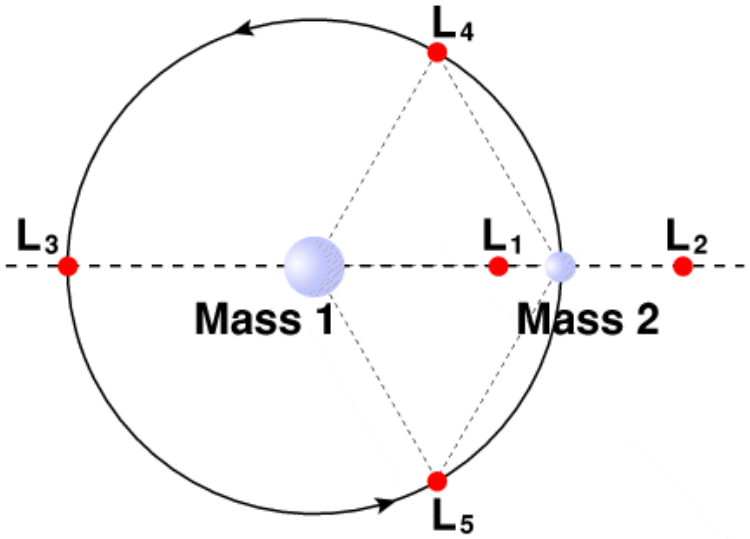

Figure 2.1: Lagrange points [NASA, 1999 [E18]].

2.2 Common-envelope phase (CE)

In star system in which Roche-lobe overfill occurs we distinguish two modes of mass transfer. The transfer can be either stable or unstable. In the case of stable mass transfer there is mass accreted by the companion star, which leads to widening of the binary. This transfer ends when the envelope of a donor star has been transferred to its companion. On the other hand there is an unstable mass accretion. Mass transfer becomes unstable when the star receiving matter cannot handle all the material being transferred from the donor star. This accumulated material then leads to filling the Roche lobes and the common envelope is formed. After the CE is formed, friction between binary system and the envelope causes the two stars in binary system spiral towards each other. This leads to release of orbital energy and ejection of the envelope. When the binary system undergoes the common envelope phase it can lead to formation of star binary that consists of compact object and companion. Common envelope phase can produce cataclysmic variables, X-ray binaries and close white dwarf binaries (Podsiadlowski, 2012 [32]).

It is important to mention that the interaction between the stars in the binary system can happen even when the star does not fill the Roche lobe. The processes through the interaction can occur are tidal effects, irradiation of the star or wind-orbit coupling. The binary stellar system can also form stable contact systems (Marchant & Bodensteiner, 2023 [25]).

2.3 White dwarfs in binary systems

White dwarf stars are found in binary systems as well as isolated stars. In case of binary system in which accretion of matter takes place there can be various phenomena alternating the evolution of the binary system (Saumon et.al., 2022 [35]). The first discovered white dwarfs were in fact white dwarfs in binary systems e.g. Sirius B or Eri B. White dwarfs

found in binary systems can be categorized into Sirius-like binaries, white dwarf and low mass star binaries and white dwarf - white dwarf binaries also called double degenerate systems (Holberg, 2009 [17]).

2.3.1 Cataclysmic variables

The cataclysmic variables are pairs of normal star (Sun-like star) and white dwarf star. These systems are rather smaller in size. In these systems the donor star is accreting material onto the white dwarf's surface. While accreting the material onto the white dwarf with large gravitational potential energy there is an X-ray emission. Thus the cataclysmic variables are brighter in X-ray than typical stars. The source of energy of white dwarf is from accretion and fusion. According to the phase in which the binary is we can divide the cataclysmic variables into fusion-dominated phase and accretion-dominated phase (Camendiz, 2007 [9]).

2.3.2 Symbiotic binaries

The term symbiotic binaries denotes an interacting binary star pair that generally consist of evolved red giant and compact white dwarf. The non-compact companion is covered in dust envelope from which the mass is transferred onto the white dwarf. Such systems tend to have long orbital periods and large separation of its components, due to large scale of the evolved red giant. Symbiotic binaries also belong to the variable star group. The timescales of the variability differ from minutes usually linked with period oscillations of the compact star to years associated with pulsations of cooler stellar companion (Mikolajewska, 2007 [27]). The mass transfer in symbiotic binaries usually occurs thanks to stellar wind of the red giant. The wind is ionized by the white dwarf and creates hot dust envelope with temperatures 7 000 - 15 000 K. In the stellar spectra we can observe emissions due to the stellar winds (Mikulášek & Zejda, 2013 [29]).

2.4 Mass transfer in binary systems

In the binary system in which the mass accretion occurs we distinguish several types of mass transfer from the star that the material is being accreted from (donor) and the star onto which is the material accreted (accretor).

The main objects of interest are the binaries in which at least one of the stars being a compact object such as white dwarf, neutron star or black hole. Since the compact objects typically posses large magnetic and gravitational fields, such binaries with the active mass transfer show impressive effects.

Cataclysmic binaries and low mass X-ray systems consist of evolved white dwarf star and main sequence star or red giant. The accretion of matter generally takes place by the material transfer onto the compact object, in this case onto a white dwarf. During the transfer, donor star will emit a stellar wind or the accretor will eject matter. This is commonly observed in novae and galactic jet sources (Negu & Tessema, 2015 [30]).

2.4.1 Classification of mass transfer

According to work of Kippenhahn & Weigert (1967) [22] and Lauterborn (1970) [24], we can classify the mass transfer into three categories following:

Type A - mass transfer occurs in the main sequence phase,
Type B - mass transfer occurs before the helium burning,
Type C - mass transfer occurs after helium exhaustion,
(Thomas, 1977 [37]).

For the case of type A mass transfer, the orbital period of the two objects is in order of a few days and the star can expand slowly through the main-sequence phase while still burning hydrogen in its core and fill its Roche lobe. Type A mass transfer is triggered during the so called slow growth phase.

For the mass transfer type B the initial orbital period is less than 100 days and the star fills its Roche lobe while expanding to the red giant. This newly formed red giant has a helium core which can ignite and therefore it can stop the accretion. The rapid expansion phase is the origin for the type B mass transfer.

Lastly, in the case of mass transfer type C the star may enter the asymptotic giant branch before reaching the point of filling its Roche lobe. The orbital period is over 100 days and the star in this scenario can be left with CO and ONe core. Type C mass transfer starts while the star is in the final expansion phase.

Thus the properties of the stellar remnant depends strongly on the state in which the Roche lobe overflow occurs. The orbital properties of a binary system after the accretion is influenced by the mechanisms of the mass transfer (Negu & Tessema, 2015 [30]).

2.5 Subdwarfs in binary systems

In the early 20th century Adams (1935) was working on the luminosity classification of stellar spectra. During his research he discovered three A type stars that were not very luminous. After his study on these faint objects he characterized them as intermediate white dwarfs. This intermediate white dwarfs had absolute magnitute approximately +5 mag and were located about 2 mag bellow the main sequence on the Hertzsprung-Russell diagram 2.2.

Later Kuiper (1938) worked on stellar spectra and found large group of stars which were shifted down 2-3 magnitudes from the main sequence stars and were stretched along the full length of the main sequence. The notation subdwarfs in short sd came from Kuiper since the stars in this section have similar properties as the main sequence star but are brighter than white dwarfs (Buscome, 1959 [8]).

The subdwarf star class can be divided to the cool and hot subdwarfs. Hot subdwarfs are stars with spectral type B or O (sdB and sdO) and in their core there comes to the helium burning. A notable portion of subdwarfs are in fact the members of binary systems with the other component being low-mass main sequence star or white dwarf. SdB and sdO stars indicate the late evolutionary stage of a low-mass stars (Heber, 2016 [14]).

2.5.1 Evolution from subdwarf to the white dwarf

Star binary pairs that consist of hot subdwarfs sdB and a white dwarfs stars can interact by Roche-lobe overflow and therefore start mass accretion from sdB star to white dwarf. In the case of sdB there is still ongoing nuclear helium burning. When the mass transfer between the subdwarf and white dwarf is possible the hot subdwarf's nuclear helium burning can be terminated and the hot subwarf contracts forming a white dwarf (Bauer & Kupfer, 2021 [5]).

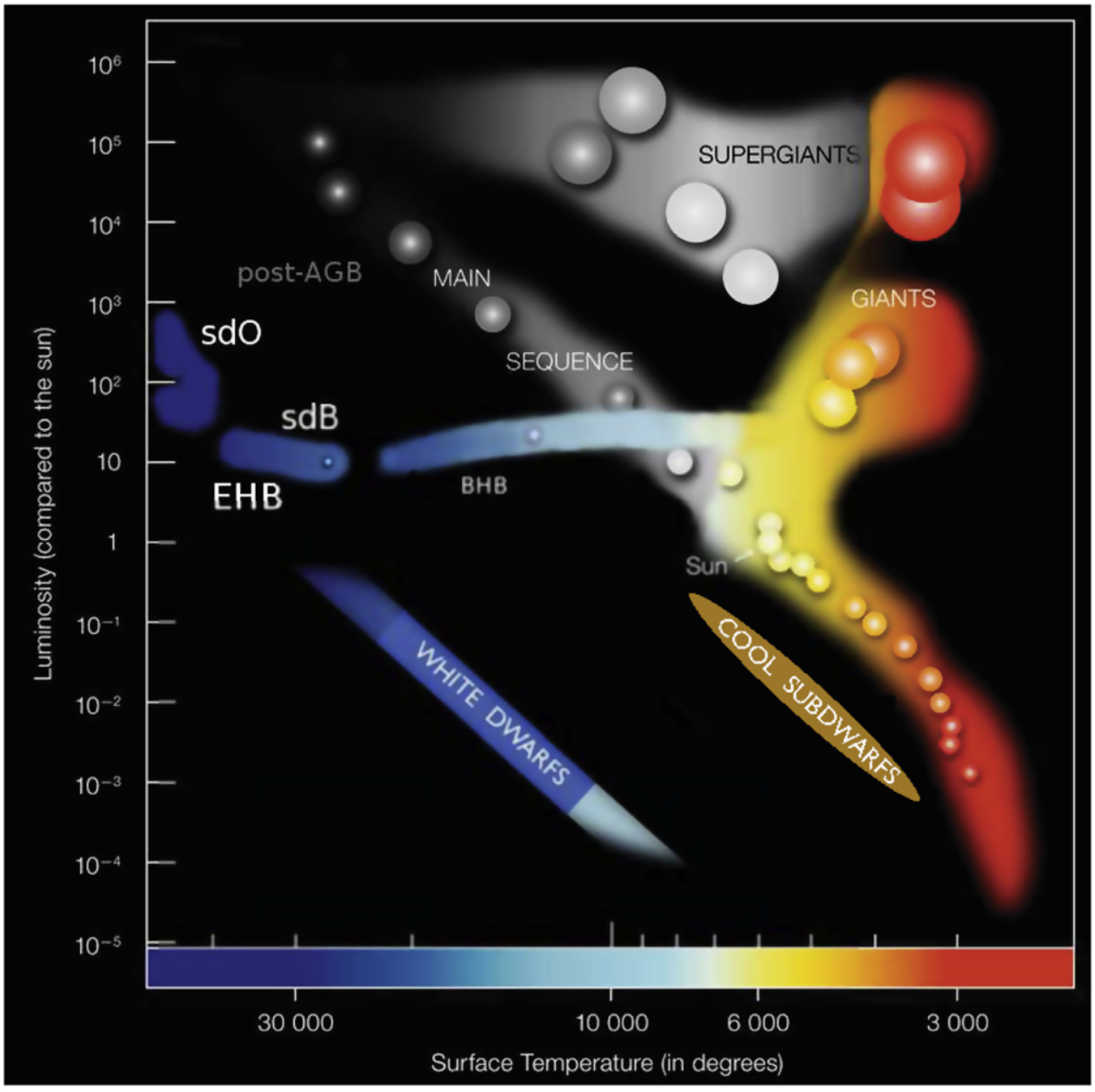

Figure 2.2: Position of Subdwarfs sdO & sdB on Hertzsprung-Russell diagram [Heber, 2016 [14]].

Chapter 3

Evolution of single stars towards white dwarfs

The evolutionary prospects of the majority of stars include eventually becoming white dwarfs. This is a fate of approximately 97% of all stars in the Galaxy. Thus, the study of these last evolutionary states of stars is key to understanding the nature of the stellar life (Fontaine, et al., 2000 [11]). White dwarfs in the binary systems such as cataclysmic variables also play an important role in stellar evolution. Since the interaction between the stars can lead to the mass transfer, it is believed that white dwarf binaries are progenitors of Type Ia supernovae. When the white dwarf exceeds so called Chandrasekhar limit which sets a boundary on the maximum mass of white dwarf 1.4 $M_{\odot}$ by accretion of material from its stellar companion it can lead to explosion of the white dwarf (Althaus, et al., 2010 [2]).

3.1 From Main Sequence Star to White Dwarf

For the large portion of life the star remains in the main sequence phase during which the central hydrogen burning is the main source of the star's energy. When the star runs out of the hydrogen in its core the central hydrogen burning stops and the star becomes a red giant. As the star evolves from the main sequence star into the red giant the hydrogen shell burning takes place. The stellar core is contracting and heating up while the outer layers expand and cool down. As the helium core heats up the temperature eventually becomes high enough for helium to ignite. After this phase of red giant the star eventually burns down the central helium and evolves into the asymptotic giant branch (AGB). As the star enters the AGB stage the thermal instabilities occur in the helium shell so called thermal pulses. In the AGB phase the star's carbon-oxygen core is gaining mass and most of the hydrogen envelope is being ejected. After the mass of star's envelope reaches the mass of 10^{-3} $M_{\odot}$ the star becomes the central star of planetary nebulae. The star may experience additional thermal pulses and reduce its envelope's mass to approximately 10^{-4} $M_{\odot}$ and the star continues to its final life stage as white dwarf (Althaus, et al., 2010 [2]).

In the stage of white dwarf the star's source of energy is provided by gravitational and thermal energy and the single white dwarf starts to cool down over time (Althaus, et al., 2010 [2]).

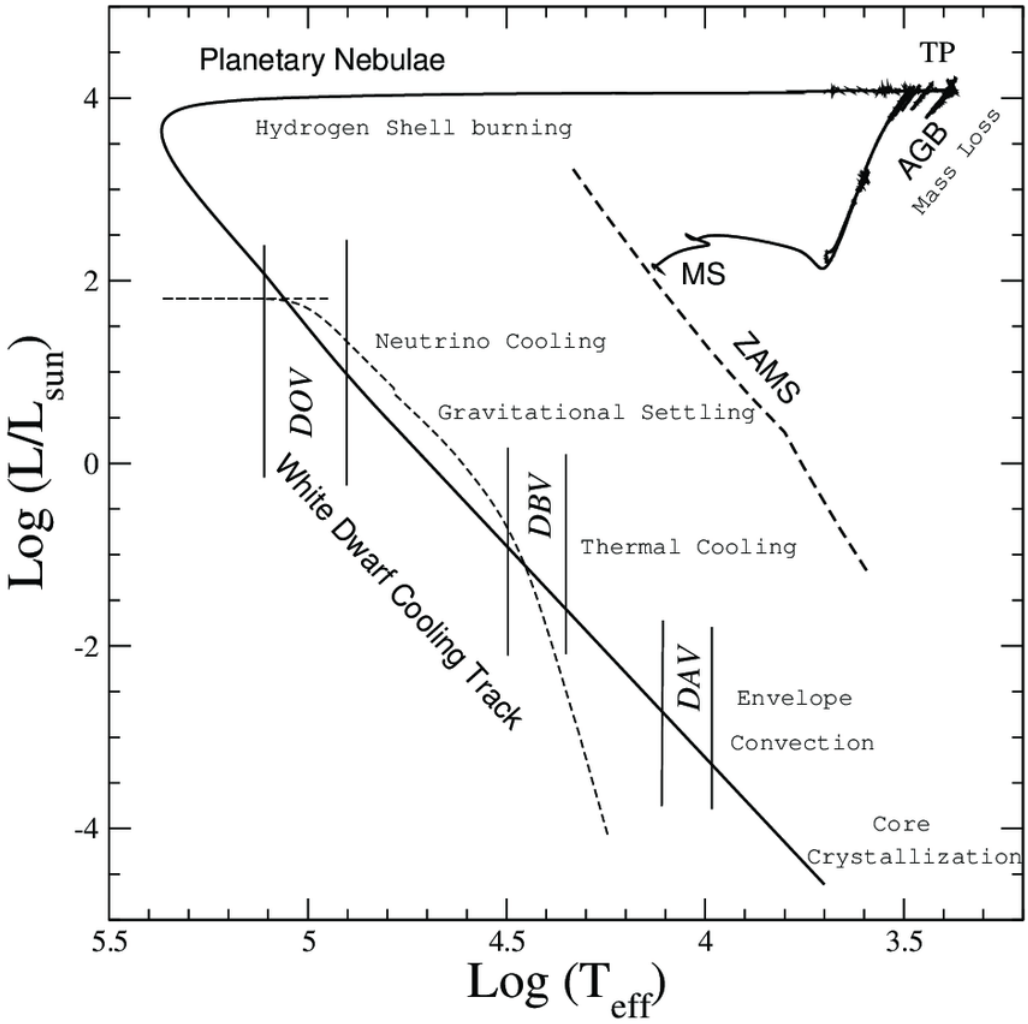

Figure 3.1: HR diagram of the evolutionary stages of main sequence star to the white dwarf stage. The initial mass of the star is 3.5 $M_{\odot}$ [Althaus, et al., 2010 [2]].

3.2 Properties of white dwarf stars

After the star enters the final stage as a white dwarf and expels its outer layers, only the hot core of a star is left. The stellar core remnant called white dwarf has a temperature $T > 100\,000$ K. In single star scenario the core cools down over the course of billions of years and eventually becomes a black dwarf. In the case of white dwarfs in binary systems the accretion of material can increase the temperature of white dwarf.

The typical mass of a white dwarf is a fraction of the Sun mass, with its maximum at 1.4 $M_{\odot}$ so called Chandrasekhar limit. Typical white dwarf's radius is measured in orders of few Earth's radii. With their masses and much smaller radii the white dwarfs are one of the densest objects in the universe. The material that makes up a white dwarf is in a degenerate state (Camendiz, 2007 [9]).

Chapter 4

Description of data sources ESO and Kepler

4.1 European Southern Observatory

European Organization for Astronomical Research in the Southern Hemisphere (ESO) is an institution located in Chile that consist of 16 member states. The organisation was found in 1962 and the main goal is to convey the possibility of space research to over 22 000 users worldwide. From 2007 Czech Republic is one of the member countries of the ESO (ESO, [E5]).

4.2 Instruments of ESO

The instruments for observations are situated in Chilean Atacama Desert thanks to its great observing possibilities. There are currently three sites for sky observations, specifically in La Silla, Paranal and Chajnantor. The first observatory is homed in La Silla with its largest 4-metre telescope. Paranal's Very Large Telescope (VLT) with its Very Large Telescope Interferometer (VLTI) is popular amongst the scientific public. The Paranal site is also going to posses the Cherenkov Telescope Array which is the biggest gamma-ray observatory with great sensitivity. Last but not least there is the Chajnantor site with its Atacama Large Milimeter/submilimeter Array (ALMA) which is operated thanks to ESO and international members of the organisation (ESO, [E5]).

4.3 History of ESO

The idea of building the European Southern Observatory came in the early 1954 from twelve astronomers in six European countries including Germany, Belgium, France, Great Britain, Netherlands and Sweden. They proposed a construction of a shared observatory in southern hemisphere. The need for such institution came from the lack of opportunities of european astronomers to make southern sky observations (Blaauw, 2010 [1]).

4.4 Very Large Telescope

The Very Large Telescope is ESO's complex consisting of four main unit telescopes with mirror diameter 8.2 m as well as four additional 1.8 m movable telescopes. VLT is situated in Paranal site in the altitude of 2635 m above the sea level. The figure 4.1 shows the Very Large Telescope complex.

The first launch of the site of four unit telescopes is dated in early 1999. To this day all four main telescopes are fully operational individually as well as simultaneously. The large diameter of the instruments allows to observe object as faint as 30 mag. VLT observations are possible in the broad section of wavelengths ranging from UV 300 nm to mid-infrared 24 μm.

Each of the single unit telescopes are equiped with instruments such as specrographs, large-field imagers or adaptive optics modules (ESO, [E6]).

4.4.1 X-shooter Spectrograph

X-shooter is and important tool for spectroscopy in the large range of wavelenghts from ultraviolet to near-infrared. The instrument was a component of the Unit Telescope 2. The spectrograph consist of three individual parts called arms which provide the dispersion of light into different wavelengths creating a spectrum.

The main aim of the X-shooter is to provide broad-range spectroscopy of many objects of interest such as white dwarfs, supernovae progenitors and gamma-ray bursts. The outcomes of this observations are discoveries of binary stars, formation of stardust in supernovae, galaxies, etc (ESO, [E7]).

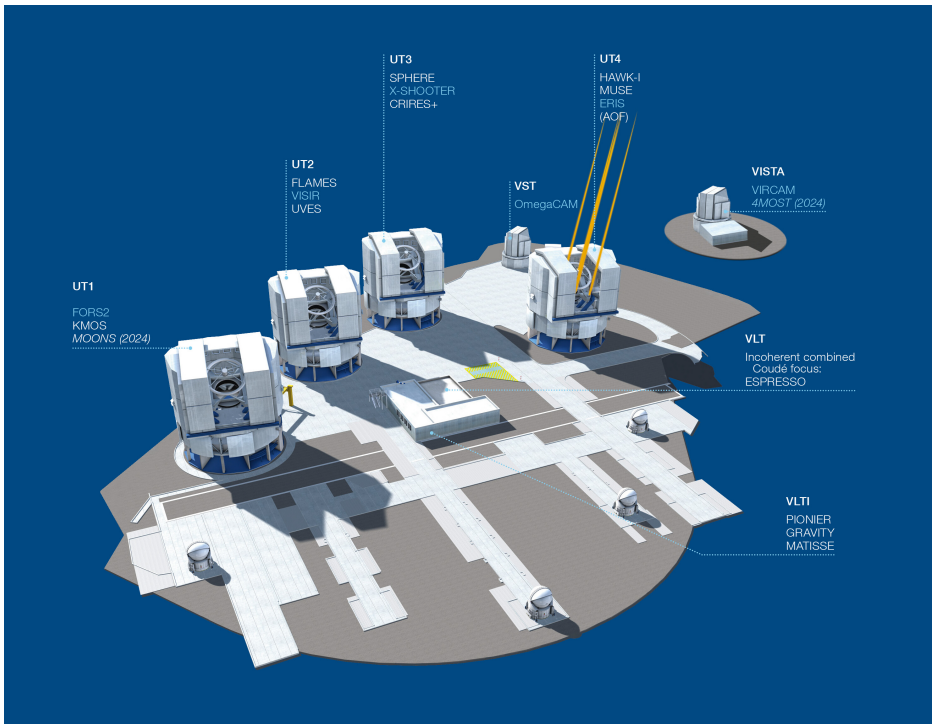

Figure 4.1: VLT telescopes and instruments in Paranal Observatory [ESO, 2009 [E13]].

4.5 Kepler Mission

The Kepler space telescope was launched in 2009 by NASA. The goal of launching the Kepler telescope was primarily the search for exoplanets, more specifically earth-like planets. The method of searching for the exoplanets lies in the monitoring of transits. The small changes in star brightness indicate the transit of an exoplanet (NASA, 2018 [E8]). The photometric observations were done in the position of the Cygnus and Lyra constellations (Howell et al., 2014 [18]).

After only 4 years after being lunched unfortunately the two out of four reaction wheels have failed, meaning that the precise pointing of the Kepler space telescope was disabled. After the major failure of reaction wheels the proposal of the K2 mission also called "Second Light" was approved. The K2 used the solar wind for stabilization of the instrument (NASA, 2018 [E9]). The new mission K2 was providing the observations of approximately 40 000 objects a year in both northern and southern hemisphere (Howell et al., 2014 [18]). With the launch of K2 mission came the possibilities to study star clusters, active galaxies, old stars and supernovae (NASA, 2013 [E10]).

The Kepler mission came to the end in the 2018 after the fuel tank of the spacecraft ran out (SPACE, 2021 [E11]).

4.6 Properties of Kepler space telescope

The telescope consisted of a single telescope with mirror diameter 1.4m and image sensor array. The goal was to monitor 100 000 stars over several years. The Kepler's photometer was assembled from the series of charge-coupled devices (CCDs). The bandpass of the spacecraft was established from 400 nm to 850 nm (NASA, 2018 [E12]). The figure 4.2 shows a schematic image of Kepler telescope with its components.

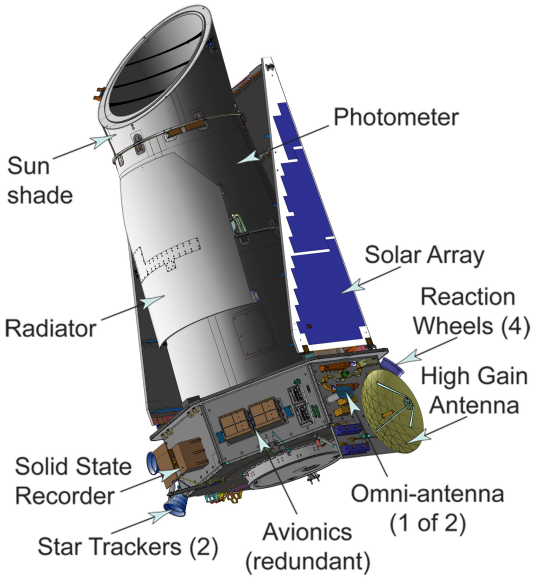

Figure 4.2: Description of devices in Kepler space telescope [NASA, 2017 [E14]].

Chapter 5

Analyzed white dwarfs

White dwarfs that are part of binary stellar systems, especially white dwarf and bright main sequence star pairs were hard to detect on optical frequencies. Therefore spectroscopy and ultraviolet photometry are crucial tools for the detection of the less luminous white dwarf companions (Kawka & Vennes, 2010 [20]). For the spectroscopic study of possible white dwarf binaries, we used the available data from VLT telescope obtained via proposal 0103.D-0194(A). The objects that were analyzed are both white dwarfs with identifiers BD+08 102 and GD 803.

5.1 BD+08 102

According to Simbad [E3] the star BD+08 102 also known under the identifier EPIC 220623236 is identified as a cataclysmic binary. The star's celestial coordinates are right ascension $00^{h}44^{m}01.16^{s}$ and declination $+09^{\circ}33^{'}02.2^{"}$ (Mason et al., 1995 [26]).

The star systems like BD+08 102 are thought to be white dwarf binaries because of UV or EUV emission. Though many of the binary candidates including BD+08 102 still remain photometrically unresolved systems. There were not detected any variations of radial velocity from observation in order of a few days, suggesting longer orbital period. The upper limit for the orbital period is roughly $P_{\mathrm{upper}} = 9.7$ yr (Barstow et.al, 2001 [3]). The high resolution spectra of this object have shown the strong Ca II H and K emission lines corresponding to the active companion (Barstow et al., 1994 [4]). Calcium spectral lines K and H are shown in the figure 5.1.

Spectral classification as well as derivation of stellar parameters of this binary was done by Holberg and others [16]. According to Holberg, the binary BD+08 102 belongs to so called Sirius-like star system in which the white dwarf is part of a binary star system with younger star. The primary component of BD+08 102 binary system is a white dwarf with spectral type DA 2.1 and the secondary component is a K2V star. Holberg's work [16] provides estimate of temperature of white dwarf T_{eff} = 23 740 K. Distance of the white dwarf binary is approximately 81 pc (Gaia EDR3, 2020 [12]). The estimate of the white dwarf's surface gravity as well as its mass was done by using ultraviolet spectroscopy. Logarithm of surface gravity $\log g = 7.31 \pm 0.04$ and the mass of white dwarf is $M_{\mathrm{WD}} = 0.39 \pm 0.01$ $\mathrm{M}_{\odot}$ (Kawka & Vennes, 2010 [20]). In comparison the mass of both stellar components derived by the Holberg's analysis are the mass of white dwarf

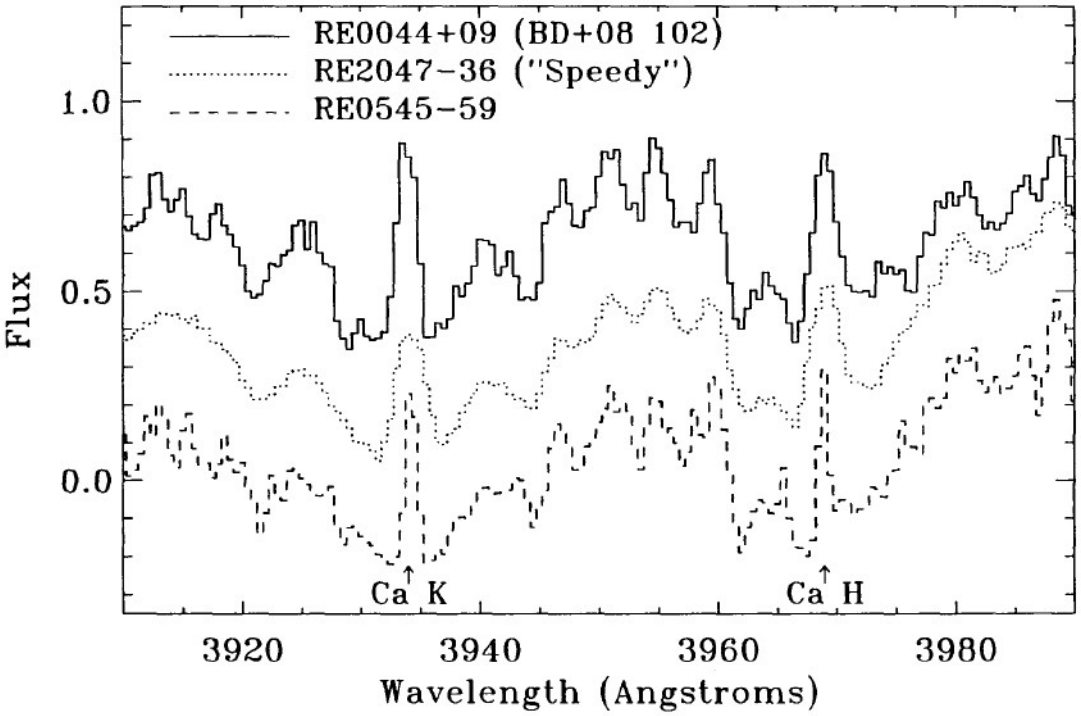

Figure 5.1: UV spectrum of BD+08 102 showing Ca K and Ca H emission lines. For comparison are also shown spectra of stars RE 2047-36 and RE 0545-59. Broadening of the BD+08 102 spectra is noticable [Kellet, et al., 1995 [21]].

$M_{WD} = 0.39$ $M_\odot$ and the estimate of a mass of its companion $M_C = 0.84$ $M_\odot$ (Holberg et al., 2013 [16]). The determined mass of a white dwarf is smaller then expected for hydrogen white dwarf . This implies that the star may have experienced mass loss due to interaction with a binary companion. The white dwarf's radius calculation yields in the result $R_{WD} = 0.0088$ $R_\odot$ (Kellett et al., 1995 [21]).

The BD+08 102 system shows little variations in radial velocity, but the less evolved star component shows significant rotation $v\sin i = 90 \pm 10$ km/s (Kellett et al., 1995 [21]). It is thought that this white dwarf with its K star companion form a wide binary, common proper motion system or completely separate system. The mean value of the measured radial velocity is $v_{radial} = 20.7 \pm 1.7$ km/s. However the photometry suggests an optical variability with best fit of a period $P = 9.992$ h. Light curve of BD+08 102 shows variable amplitude, with differences around ~ 0.04 mag. The light curve of BD+08 102 obtained from 2 year observations can be seen in the figure 5.2 (Kellett et al., 1995 [21]).

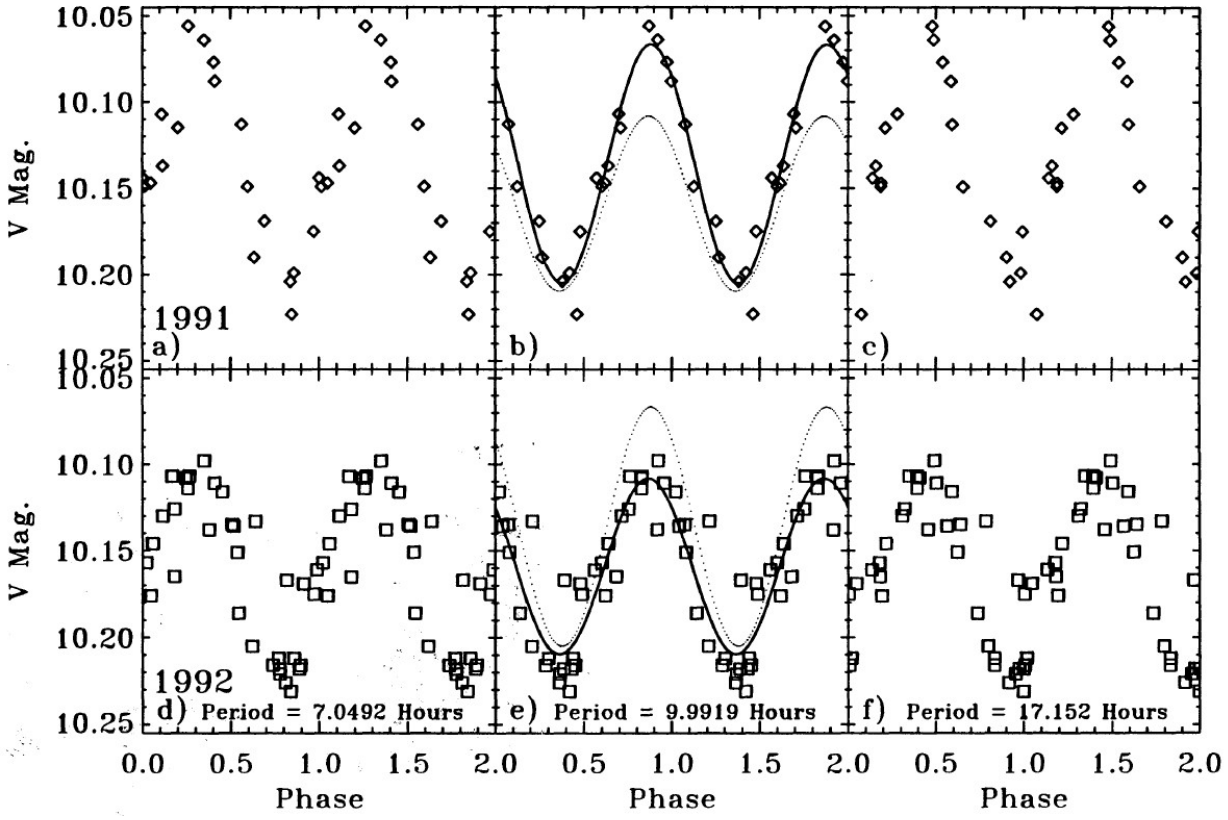

Figure 5.2: Light curve of BD+08 102 done by V band photometry over 2 year observation. Dotted line represents an observation from one year meanwhile the solid line is the fit of the data from the second year [Kellett et al., 1995 [21]].

5.2 GD 803

Star GD 803 known as EPIC 220171396 is classified as a white dwarf type star with coordinates right ascension $01^{h}10^{m}42.02^{s}$ and declination - $01^{\circ}08^{'}39.35^{"}$ (SDSS DR12, 2015 [E19]).

Following stellar parameters of object GD 803 were derived from Sloan Digital Sky Survey data release 12. The study of hot white dwarfs ($T_{\text{eff}} \geq 30\,000$ K) done by Bédard and others [6] analyzed 1806 spectroscopically observed white dwarfs. For each star in the selection, that also included white dwarf GD 803, atmospheric as well as stellar parameters were derived. GD 803 was established as hydrogen white dwarf with companion, therefore DA+M spectral type. The effective temperature of the white dwarf stellar component with rather large uncertainty is $T_{\text{eff}} = 60\ 400 \pm 2\ 700$ K. Derived surface gravity is in logarithmic scale $\log g = 7.54 \pm 0.15$. The stellar mass of GD 803 in units of solar masses is $M_{\text{WD}} = 0.53 \pm 0.05\ \text{M}_{\odot}$. Another important stellar parameter is radius $R = 0.0205 \pm 0.0026\ \text{R}_{\odot}$. Logarithm of luminosity was established to be $\log(L/\text{L}_{\odot}) = 0.70 \pm 0.14$. Nonetheless, the cooling age of white dwarf GD 803 is $\log(\tau/1\text{yr}) = 5.74 \pm 0.58$ (Bédard et al., 2020 [6]).

Similar study of white dwarf binaries was done also in 2010 from Sloan Digital Sky Survey data release 6 [E4]. From the sample data it was possible to identify 440 new white dwarf-main sequence binaries, which when taken into account the previously known pairs, add up to a total of 1602 white dwarf binaries. Applying the decomposition/fitting method it was possible to determine stellar parameters such as effective temperature, surface gravity, stellar mass and distances of the white dwarfs and respectively their companions. Among the studied white dwarf-main sequence pairs was also our object of interest GD 803 (Rebassa-Mansergas et al., 2010 [33]).

The measured effective temperature of GD 803 according to this analysis is for the white dwarf component $T_{\text{eff}} = 70\,500$ K and for the companion star $T_{\text{eff}} = 6\,500$ K. Therefore the spectral type of GD 803 star system was established as DA + K. Surface gravity calculations predict values $\log g_{\text{WD}} = 7.49$ for white dwarf and $\log g_{\text{C}} = 8.91$ for the white dwarf's companion. GD 803 masses of both components are $M_{\text{WD}} = 0.55\ \text{M}_{\odot}$ and $M_{\text{C}} = 1.15\ \text{M}_{\odot}$. The distance to white dwarf GD 803 in parsecs is $D_{\text{WD}} = 322$ pc (Gaia EDR3, 2020 [12]). For the measurement of radial velocity they have used Na I doublet as well as Hα spectral line. Value of radial velocity measured from Na I doublet is $v_{\text{rad}} = 79.1 \pm 14.9$ km/s. The radial velocity determined according to Hα is $v_{\text{rad}} = 73.5 \pm 11.7$ km/s (Rebassa-Mansergas et al., 2010 [33]).

Chapter 6

Analysis of the VLT Spectra

6.1 Kepler photometric results

The selection of the white dwarf stars GD 803 and BD+08 102 for spectral analysis was done based on their periodic light variability. The origin of photometric variability can be the existence of a second component gravitationally bound to the white dwarf. The light curves of inspected stars were derived from Kepler data and are shown in the figures 6.1 and 6.2. The x axis in the plots is phase calculated from photometric period. The y-axis represents flux difference divided by the mean value of the flux. The light curve data was obtained from MAST: Barbara A. Mikulski Archive for Space Telescopes (MAST, [E15]). Light curves of both objects were fitted by sine wave function $f(\varphi) = a\sin(2\pi\varphi + b)$. The phase calculation of BD+08 102 was done with period 0.416486 d and epoch 2458669.9168 d. For the white dwarf GD 803 period used in phase determination was 0.471987 d and epoch 2458711.7022 d.

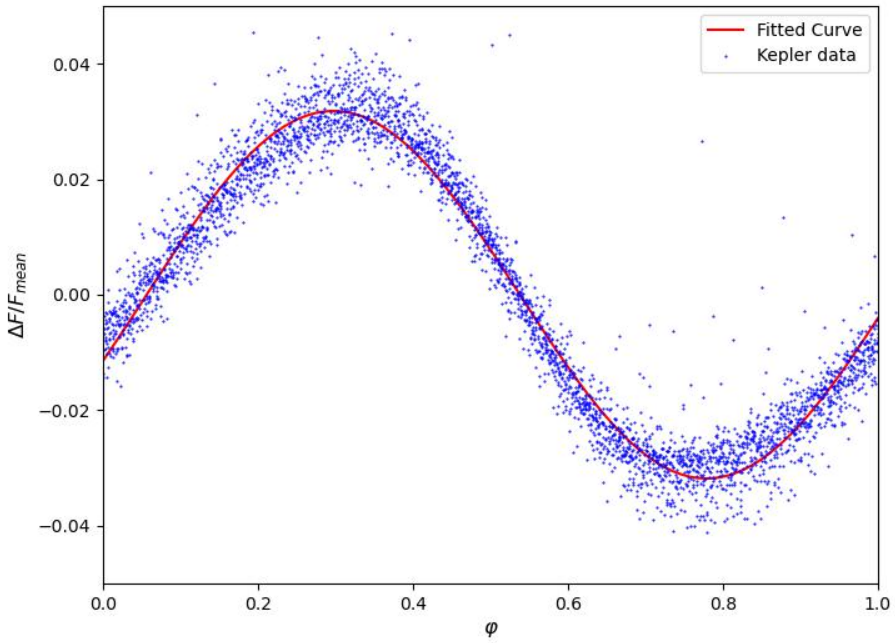

Figure 6.1: Phase-folded light curve of GD 803.

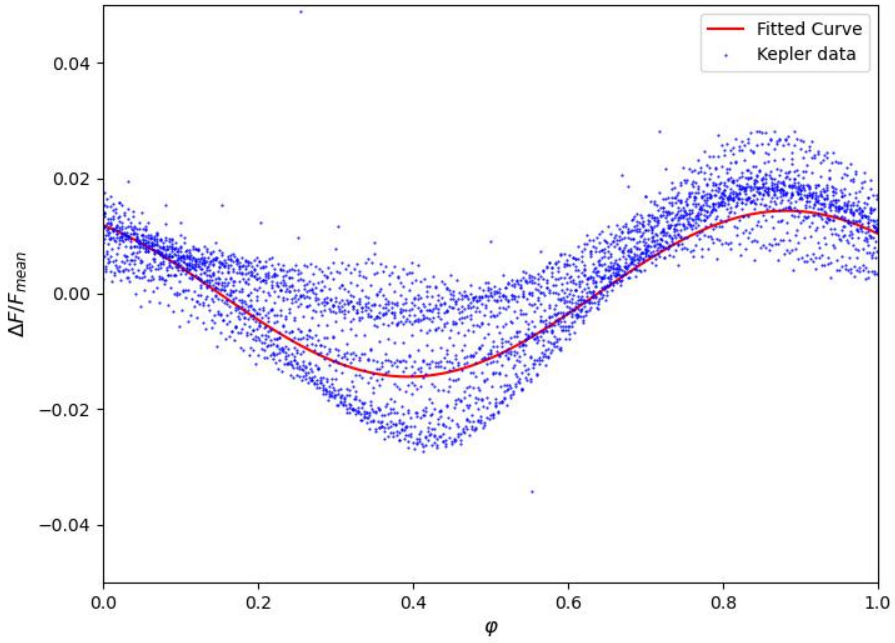

Figure 6.2: Phase-folded light curve of BD+08 102.

6.2 Spectral analysis

Our goal in this work was to calculate radial velocities of photometrically variable white dwarfs and analyze the variability in radial velocities to test the binary origin of these stars.

The spectra that was used for spectral analysis of the two stars were obtained based on the ESO proposal 0103.D-0194(A). The data are from X-shoooter spectrograph 4.4.1. For each of the investigated object, we had spectra from near infrared wavelength range (NIR) , visual wavelength range spectra (VIS) and lastly spectra from near ultraviolet and visual wavelength range (UVB). The specific information about the individual spectra are summarized in the table 6.1. The wavelength range for NIR region is from 994.02 nm to 2478.96 nm. For VIS region the wavelength region is from 533.66 nm to 1020.0 nm and lastly for the UVB part of the spectra the range is from 298.92 nm to 555.98 nm. It is important to mention that not all data in respective wavelengths were eligible for doing spectral analysis. All spectra had noise at the short wavelength part of the spectra, so for the purpose of spectral analysis these parts of the spectra were excluded 6.3. The graphs and fits of the spectra were done using Python and its respective libraries [E2].

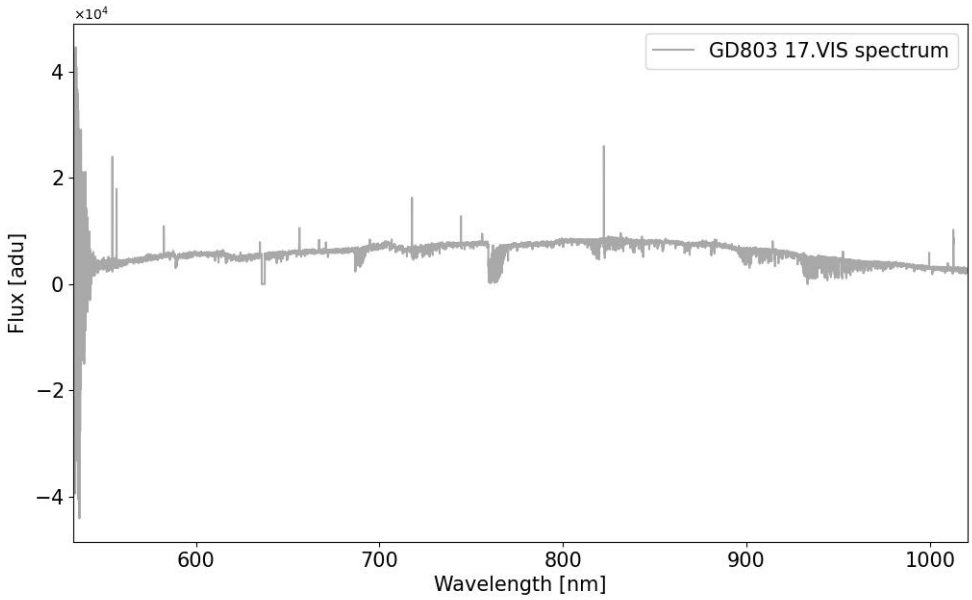

Figure 6.3: Example of unedited 17 VIS spectrum of GD 803.

No.	Object	Region	Date of obs.	Mid exp. time UT	MJD mid exp. [d]	Time elapsed [s]
1	BD+08 102	NIR	15.08.2019	09:46:37.197	58710.40824302	150
2	BD+08 102	UVB	15.08.2019	09:46:39.016	58710.40826407	150
3	BD+08 102	VIS	15.08.2019	09:47:26.006	58710.40826396	56
4	BD+08 102	NIR	15.09.2019	07:29:04.026	58741.31272020	150
5	BD+08 102	UVB	15.09.2019	07:29:06.004	58741.31274310	150
6	BD+08 102	VIS	15.09.2019	07:29:53.009	58741.31274314	56
7	BD+08 102	NIR	06.08.2019	09:47:00.220	58701.40850948	150
8	BD+08 102	UVB	06.08.2019	09:47:02.005	58701.40853015	150
9	BD+08 102	VIS	06.08.2019	09:47:49.023	58701.40853035	56
10	BD+08 102	NIR	05.07.2019	09:59:00.510	58669.41684618	150
11	BD+08 102	UVB	05.07.2019	09:59:02.004	58669.41686347	150
12	BD+08 102	VIS	05.07.2019	09:59:49.018	58669.41686363	56
13	BD+08 102	NIR	16.08.2019	04:29:13.325	58711.18782783	150
14	BD+08 102	UVB	16.08.2019	04:29:15.006	58711.18784729	150
15	BD+08 102	VIS	16.08.2019	04:30:02.010	58711.18784733	56
16	GD 803	UVB	20.09.2019	08:56:35.003	58746.38015050	1300
17	GD 803	VIS	20.09.2019	08:57:22.007	58746.38015054	1206
18	GD 803	NIR	20.09.2019	08:57:22.960	58746.38012685	1200
19	GD 803	UVB	15.09.2019	07:41:02.005	58741.32768524	1300
20	GD 803	VIS	15.09.2019	07:41:49.027	58741.32768549	1206
21	GD 803	NIR	15.09.2019	07:41:50.440	58741.32766712	1200
22	GD 803	UVB	16.08.2019	04:40:24.014	58711.20224552	1300
23	GD 803	VIS	16.08.2019	04:41:11.008	58711.20224546	1206
24	GD 803	NIR	16.08.2019	04:41:12.100	58711.20222337	1200
25	GD 803	UVB	01.09.2019	07:58:50.000	58727.34004630	1300
26	GD 803	VIS	01.09.2019	07:59:37.004	58727.34004634	1206
27	GD 803	NIR	01.09.2019	07:59:37.547	58727.34001790	1200

Table 6.1: Information about spectral dataset obtained from VLT.

The standard procedure in astrophysics related to processing the spectra is their normalization. For the process of spectra normalization we used an available software for stellar spectra analysis SPLAT VO [E1]. The normalization was done by estimating of a curve describing a continuum which was then subtracted from the original spectrum. For the calculation of the radial velocities we needed to perform identification of the prominent spectral lines. The identification itself was done by comparison of the VLT spectra with the SYNSPEC model spectra (Lanz & Hubeny, 2017 [19]). The model was calculated for temperature $T = 4250$ K and logarithm of surface gravity $\log g = 4$. With the identified individual spectral lines in hand, we knew their rest wavelengths and we needed to establish their observed wavelengths.

6.3 Fitting of the spectral lines

The initial attempt to obtain the observed wavelengths of the spectral lines was done by fitting the lines by Gaussian profile 6.1. Parameters of the Gauss function c, λ_0, σ represent the amplitude of the curve, mean value and deviation in this order. The observed wavelength was estimated from the Gaussian fit as the mean value of the fitted curve.

$$f(\lambda) = 1 - ce^{-\frac{(\lambda-\lambda_0)^2}{2\sigma^2}} \tag{6.1}$$

However, under closer inspection not all spectra were possible to normalize properly, so for the better estimate of the observed wavelengths we decided to fit the lines by Gaussian profile multiplied by a linear function 6.2. This step was done to better describe the profiles of spectral lines.

$$f(\lambda) = (a\lambda + b)\left(1 - ce^{-\frac{(\lambda-\lambda_0)^2}{\sigma^2}}\right) \tag{6.2}$$

The demonstration of the difference between the initial fit of the spectral line Hε by Gaussian profile and the fit by adjusted Gaussian profile is shown in the figure 6.4 and 6.5.

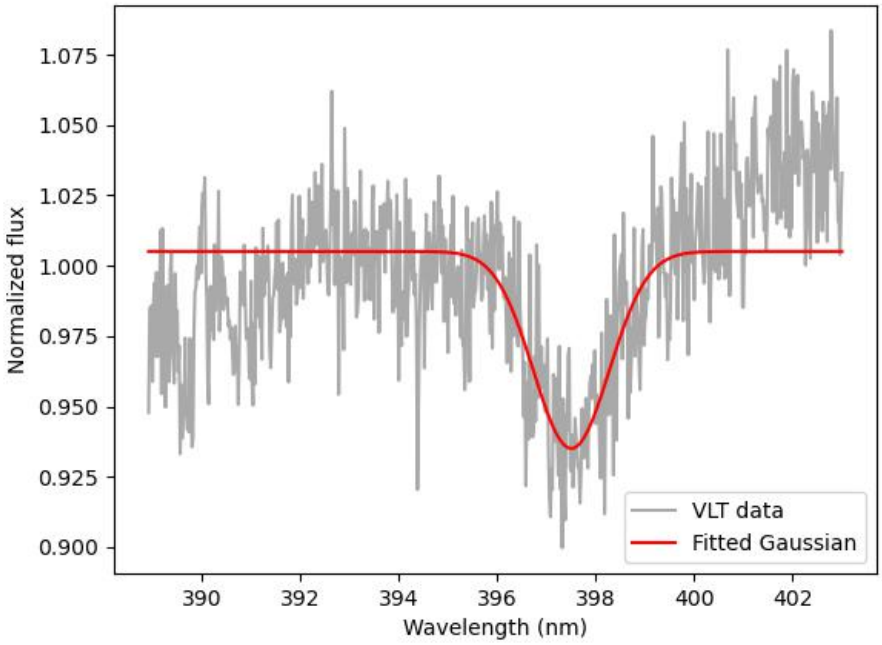

Figure 6.4: Fitting of the Hε line in 16 UVB spectrum of GD 803 by Gaussian profile.

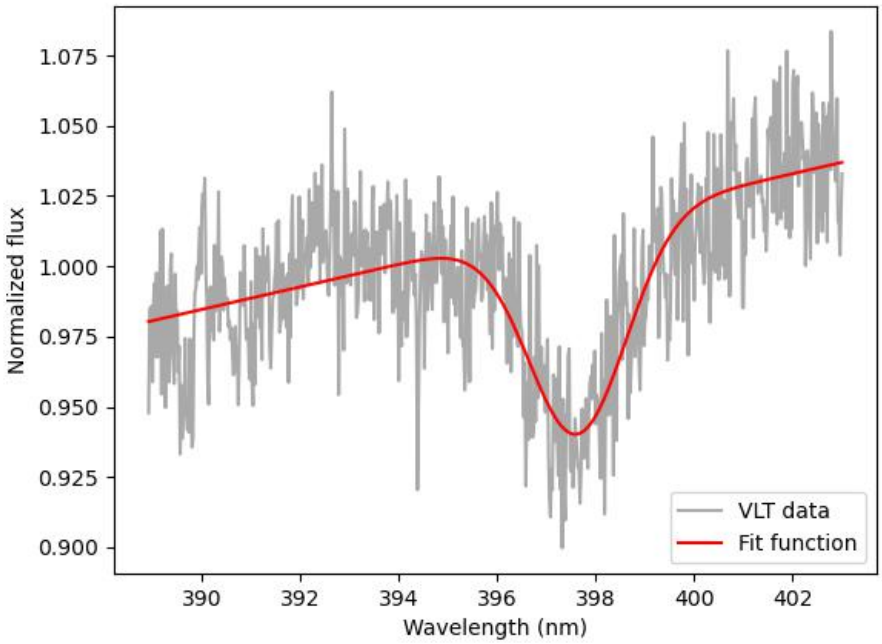

Figure 6.5: Fitting of the Hε line in 16 UVB spectrum of GD 803 by adjusted Gaussian profile.

6.4 Radial velocity

After the fitting the spectral lines by adjusted Gaussian profile, we acquired the observed wavelengths of the lines. This allowed us to determine the Doppler shifts of the lines. The radial velocity for each of the line was then calculated from the Doppler shift of the spectral line as is in equation 6.3.

$$v_{\text{rad}} = c \, \frac{|\Delta\lambda|}{\lambda_0} \tag{6.3}$$

Where c denotes the speed of light, $\Delta\lambda$ is the shift in wavelength observed for the object compared to the rest wavelength and λ_0 is rest wavelength.

6.5 GD 803 Spectra

6.5.1 UVB spectra

With the analysis we started firstly on white dwarf spectra of GD 803. In the UVB spectra we could identify the wide spectral lines of Balmer series of hydrogen. According to the very broad profile of these lines we can connect these lines to the white dwarf. Particularly, they were lines Hε, Hδ, Hγ and Hβ . The hydrogen lines were present in all available UVB spectra of GD 803 6.6, 6.7, 6.8, 6.9.

Along with hydrogen lines there is also another absorption line visible in the spectra at wavelength around 478 nm. We suspect that this absorption line is the ultra-high excitation (UHE) line observed in hot white dwarfs. UHE lines belong to ultra-high excited metals such as NVII, OVIII. The temperature for formation of such highly excited lines is much higher than the typical effective temperature of white dwarf, therefore UHE lines do not have photospheric origin. Unfortunately, the formation of the UHE lines in white dwarf spectra is not yet fully understood. According to research done by Werner and others it was proposed that these lines originate in hot stellar wind (Werner et al., 1995 [39]). Approximately 10 % of white dwarfs in their cooling sequence show UHE absorption lines. Majority of the white dwarfs showing the UHE phenomenon are photometrically variable (Reindl et al., 2021 [34]). Reindl and others studied ultra-high excitation absorption lines in the spectra of hot white dwarfs and detected new UHE lines around 3872, 4330, 4655, 4785, 5280, 6060 and 6477 Å. Hence, the absorption line around 478 nm or 4780 Å observed in GD 803 matches the ultra-high excitation line detected by Reindl et al., 2021 [34].

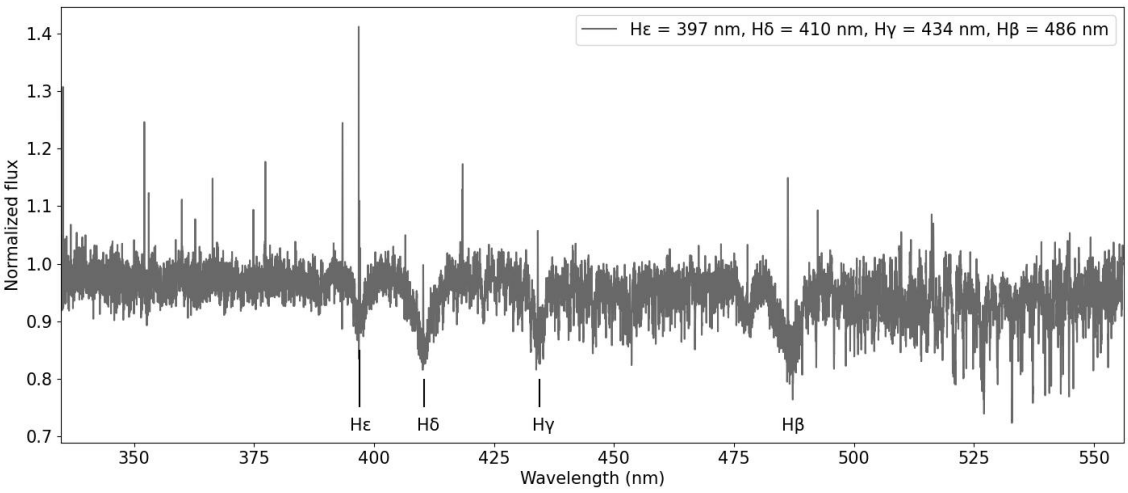

Figure 6.6: Identified white dwarf spectral lines in GD 803 16 UVB spectrum.

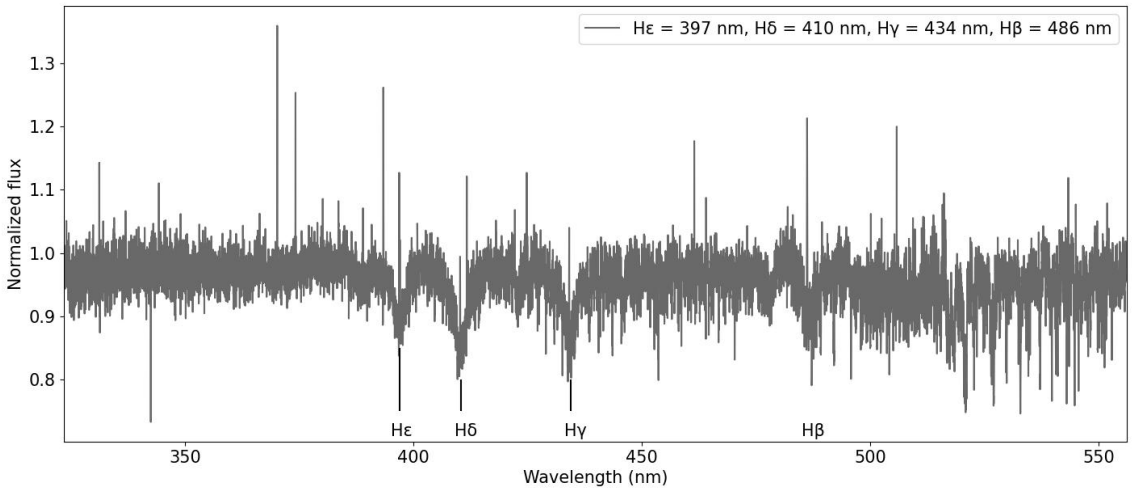

Figure 6.7: Identified white dwarf spectral lines in GD 803 19 UVB spectrum.

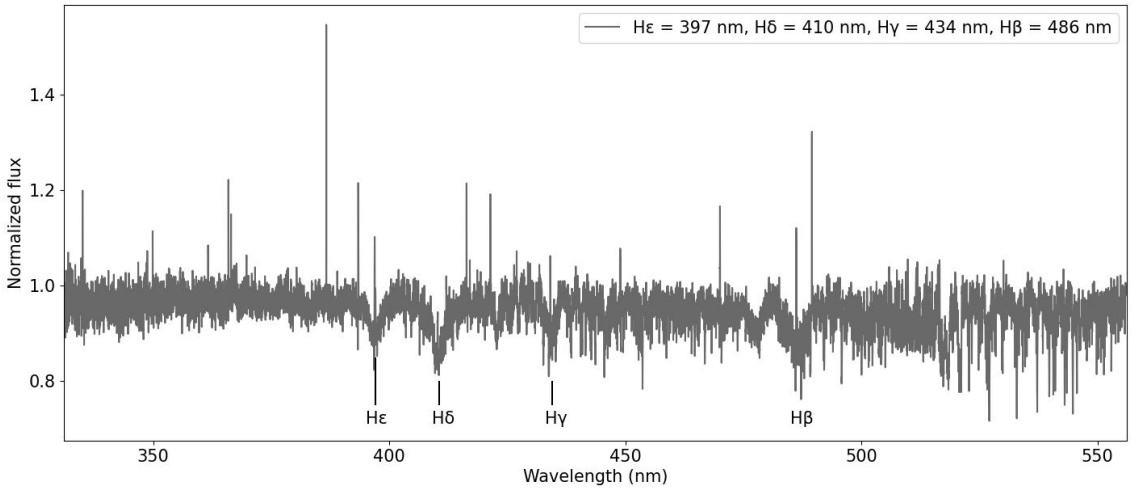

Figure 6.8: Identified white dwarf spectral lines in GD 803 22 UVB spectrum.

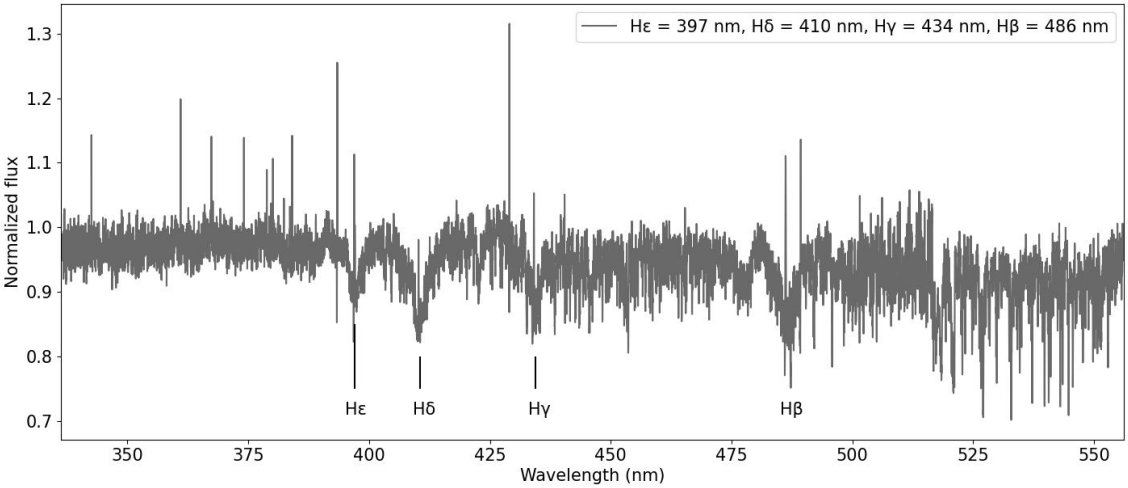

Figure 6.9: Identified white dwarf spectral lines in GD 803 25 UVB spectrum.

From the analysis of the UVB spectra we can see there are noticeable central emissions in the hydrogen lines. For the purpose of determination of observed wavelengths we did not consider this part of the spectrum. Overall there were 4 individual UVB spectra from which we could identify 4 hydrogen lines giving us 16 radial velocity measurements. In the figure 6.10 there are shown hydrogen lines fitted by adjusted Gaussian profile. Measured radial velocities of the hydrogen lines from ultraviolet spectra are shown in the table 6.2. The radial velocities values differ among each spectra with rather large deviation.

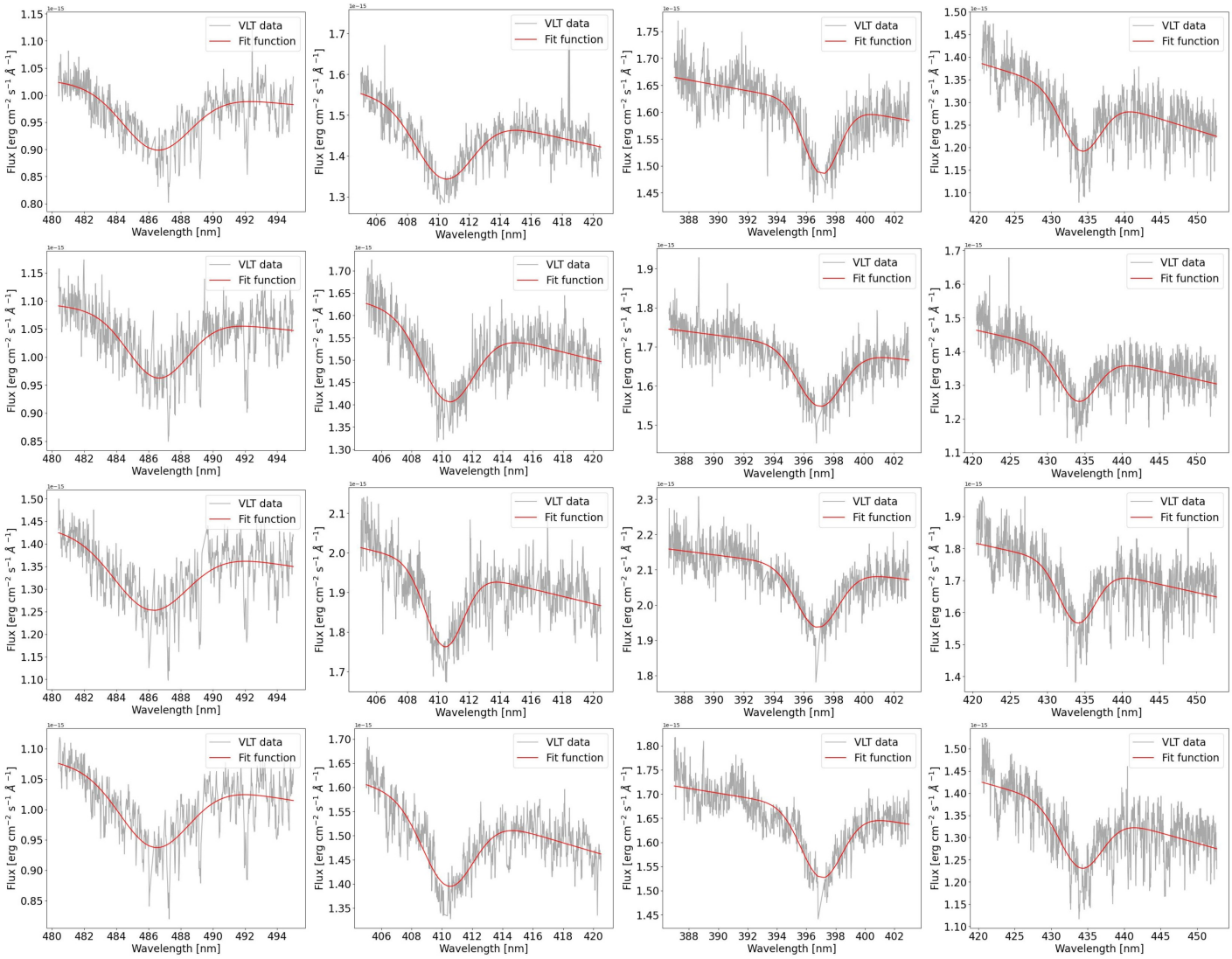

Figure 6.10: Hydrogen Balmer series of GD803, in the rows from top to bottom there are different spectra 16, 19, 22, and 25, in the columns there are hydrogen lines from left to right Hβ, Hδ, Hε, Hγ.

No.	Spectral line	Rest wavelength [nm]	Obs. wavelength [nm]	Radial velocity [km/s]
16	Hε	397.0075	397.6311	471.2
	Hδ	410.1734	410.7029	387.3
	Hγ	434.0472	434.1774	90.0
	Hβ	486.1350	486.3959	161.0
19	Hε	397.0075	397.0297	16.8
	Hδ	410.1734	410.3715	144.9
	Hγ	434.0472	434.0858	26.7
	Hβ	486.1350	486.5669	266.6
22	Hε	397.0075	396.9007	80.7
	Hδ	410.1734	410.3686	142.8
	Hγ	434.0472	433.9745	50.3
	Hβ	486.1350	486.1487	8.4
25	Hε	397.0075	397.0306	17.5
	Hδ	410.1734	410.4168	178.0
	Hγ	434.0472	434.0029	30.7
	Hβ	486.1350	486.3539	135.1

Table 6.2: Calculated radial velocity of Balmer series for different UVB spectra.

To investigate potential variations in radial velocity, we plotted the mean radial velocity from each of the spectra against the time in units of Julian date. The result is in the figure 6.11. The radial velocity curve does not exhibit clear trend in radial velocity variability. Additionally, the radial velocity was plotted as a function of phase 6.12. The phase was determined by relation 6.4 , as the decimal part of the quotient of the time difference and the period, where t_0 is the epoch detected as the first value of the time measurement. The photometric period used for the phase estimation was acquired from personal calculation of prof. Mikulášek. The value of the period is 0.471987(6) days and $t_0 = 2458711.7022$ d. In the table 6.3 there is mean value of radial velocity from UVB spectra with its standard deviation.

$$\varphi = \mathrm{frac}\left(\frac{t - t_0}{P}\right) \tag{6.4}$$

No.	Region	Radial velocity [km/s]
16	UVB	277 ± 157
19	UVB	114 ± 101
22	UVB	71 ± 49
25	UVB	90 ± 68

Table 6.3: Mean values of radial velocity obtained from individual UVB spectra of GD 803.

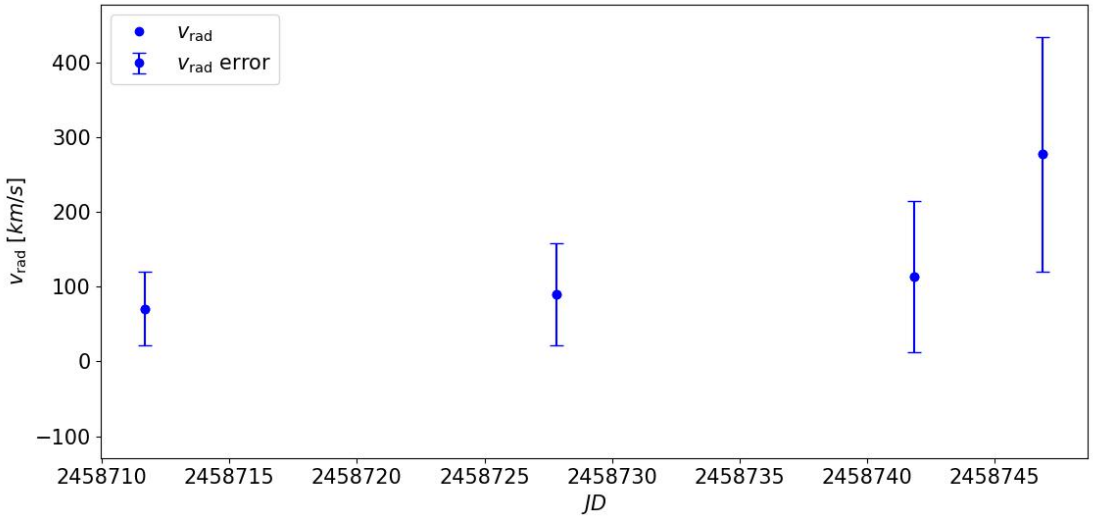

Figure 6.11: Radial velocity curve of GD 803 as a function of time. The blue points represent radial velocity values and vertical lines are respective error bars for each value.

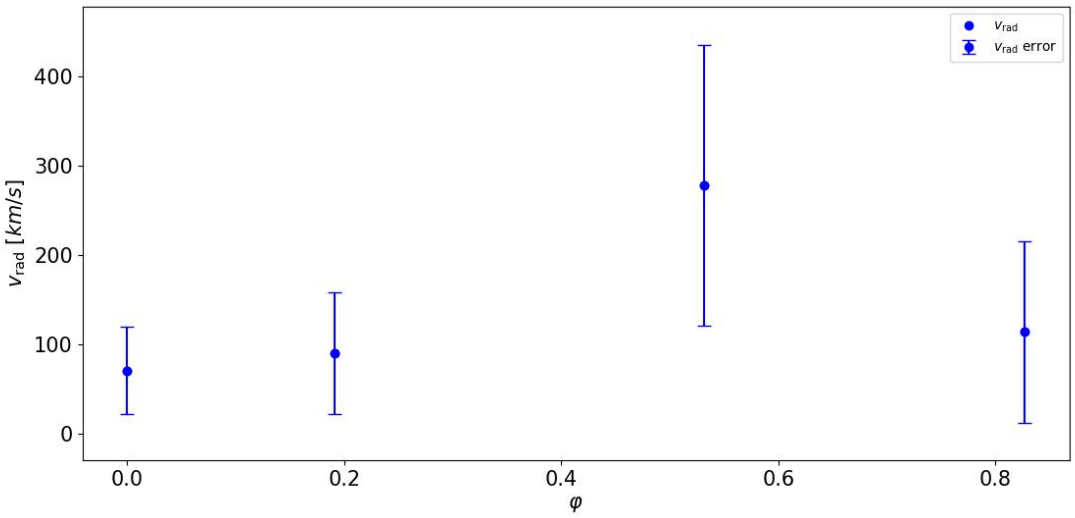

Figure 6.12: Radial velocity curve of GD 803 as a function of phase. The blue points represent radial velocity values and vertical lines are respective error bars for each value.

6.5.2 Central emissions in Balmer lines

The central parts of the absorption hydrogen lines identified from UVB region revealed noticeable central emissions. For the purpose of determining the wavelength of respective spectral lines we did not consider these central region of the lines. However, the presence of these emissions suggest that such lines originate from binary interaction. The material of the wind from the cooler star can interact with white dwarf which then can ionize this matter. The result of such interaction can explain the central emissions. The following figures 6.13, 6.14, 6.15, 6.16 display the UVB spectra with inlets showing the centres of the hygrogen lines.

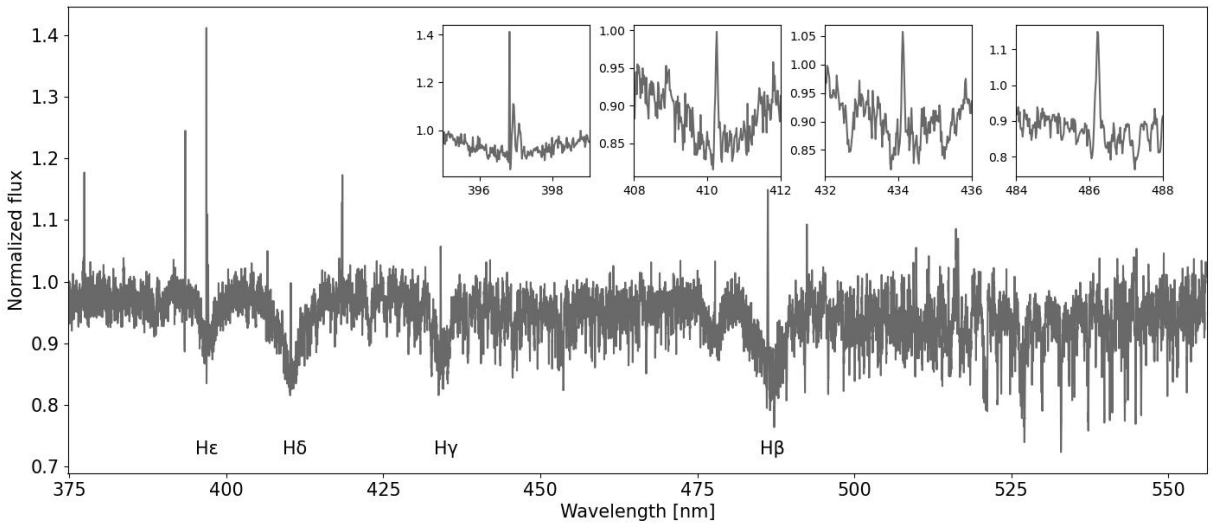

Figure 6.13: 16 UVB spectrum of star GD 803. The spectrum shows hydrogen absorption Balmer lines with central emission.

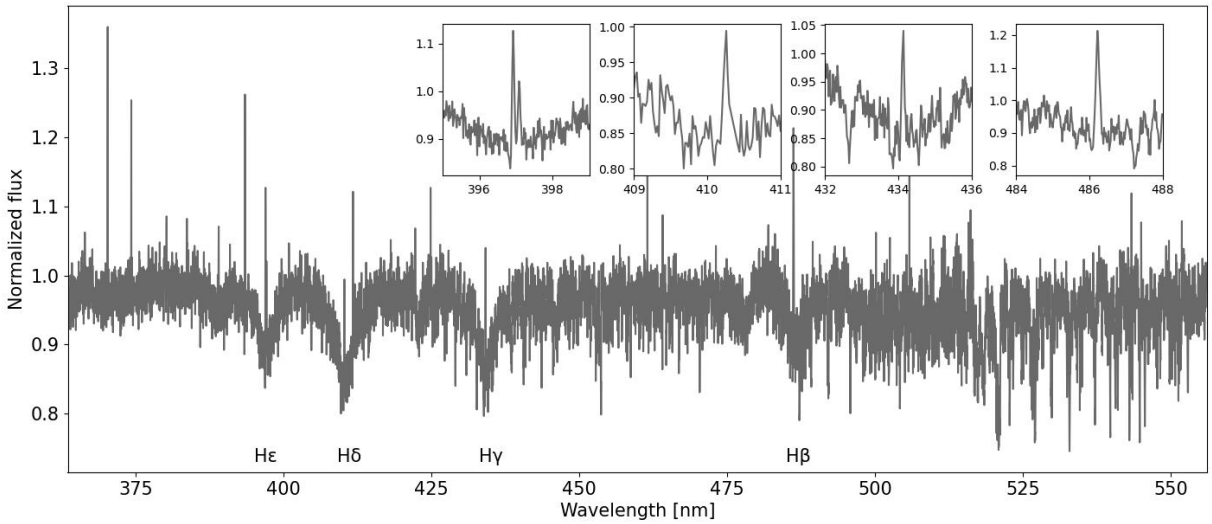

Figure 6.14: 19 UVB spectrum of star GD 803. The spectrum shows hydrogen absorption Balmer lines with central emission.

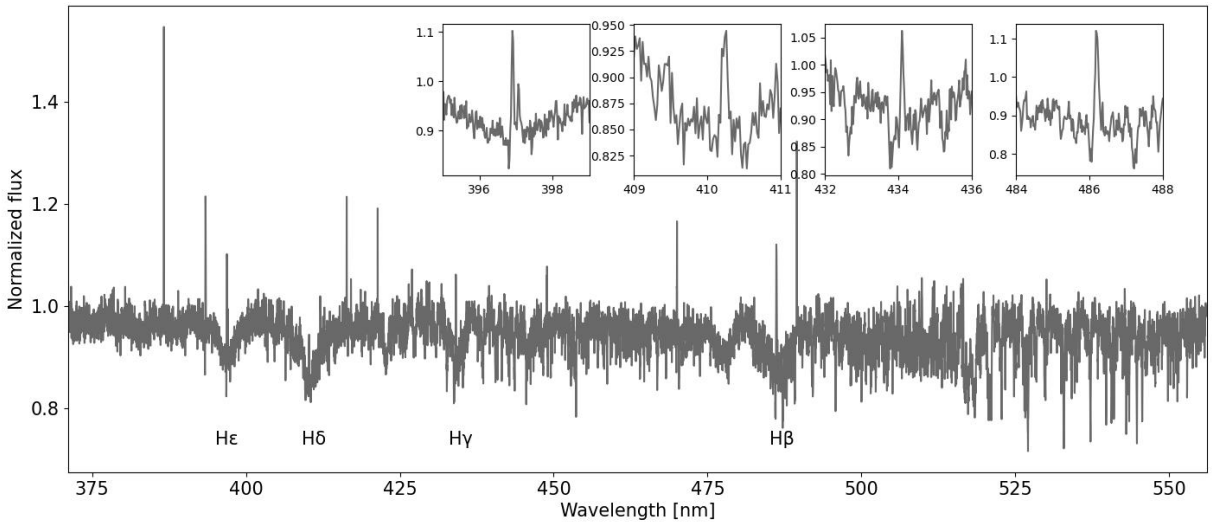

Figure 6.15: 22 UVB spectrum of star GD 803. The spectrum shows hydrogen absorption Balmer lines with central emission.

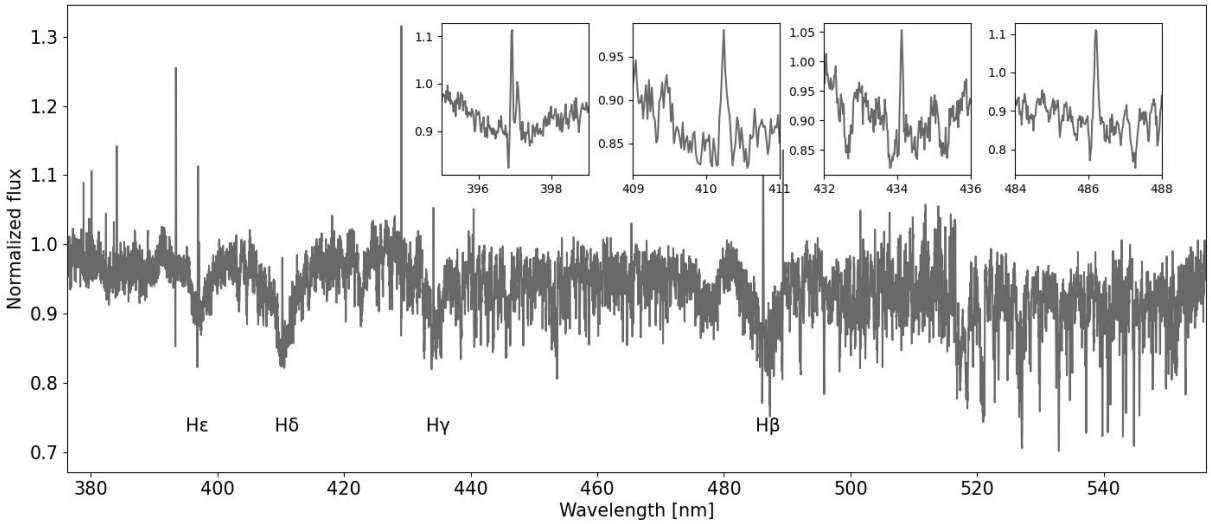

Figure 6.16: 25 UVB spectrum of star GD 803. The spectrum shows hydrogen absorption Balmer lines with central emission.

6.5.3 VIS spectra

The equivalent approach of analysis was performed for obtained visual spectra. Upon examination of visual spectra, the initial observation revealed a significantly higher density of spectral lines compared to the UVB spectra. In addition, the width of the spectral lines in the visual spectra appeared more narrow. Based on this observation, it can be concluded that these lines are actually associated with the cooler star rather than the white dwarf.

The identification reveals the most prominent lines in the visual spectra to be sodium, calcium and iron lines. Since the spectra were obtained from ground observation, Earth's atmosphere absorption lines called telluric lines are present in some sections of the spectra. For our analysis, we specifically selected lines that are outside of telluric lines region. All the visual spectra are plotted in the figures 6.17, 6.18, 6.19 and continuing in Appendix chapter 6.7.

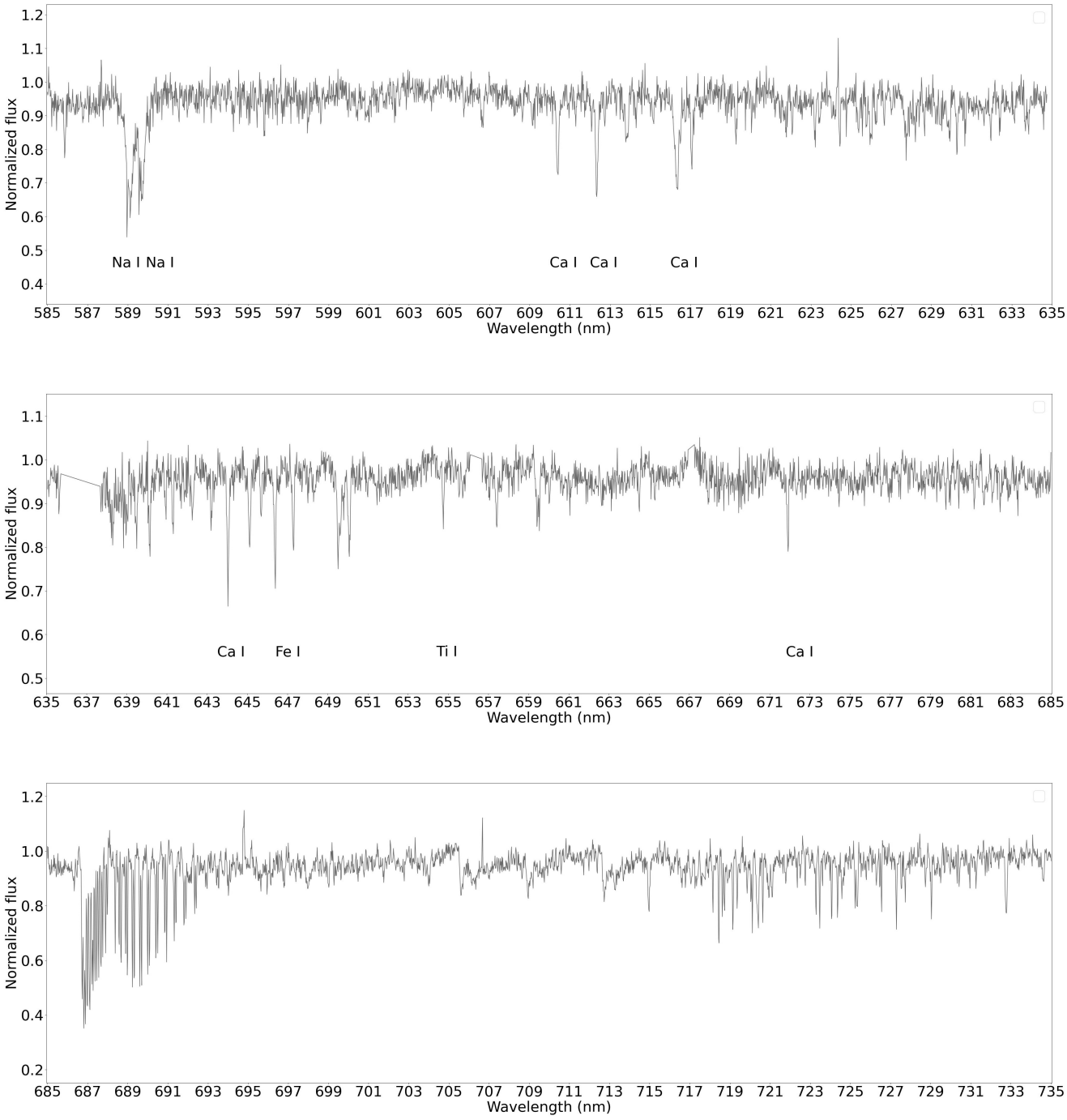

Figure 6.17: Spectral lines identification in 17 VIS spectrum of GD 803

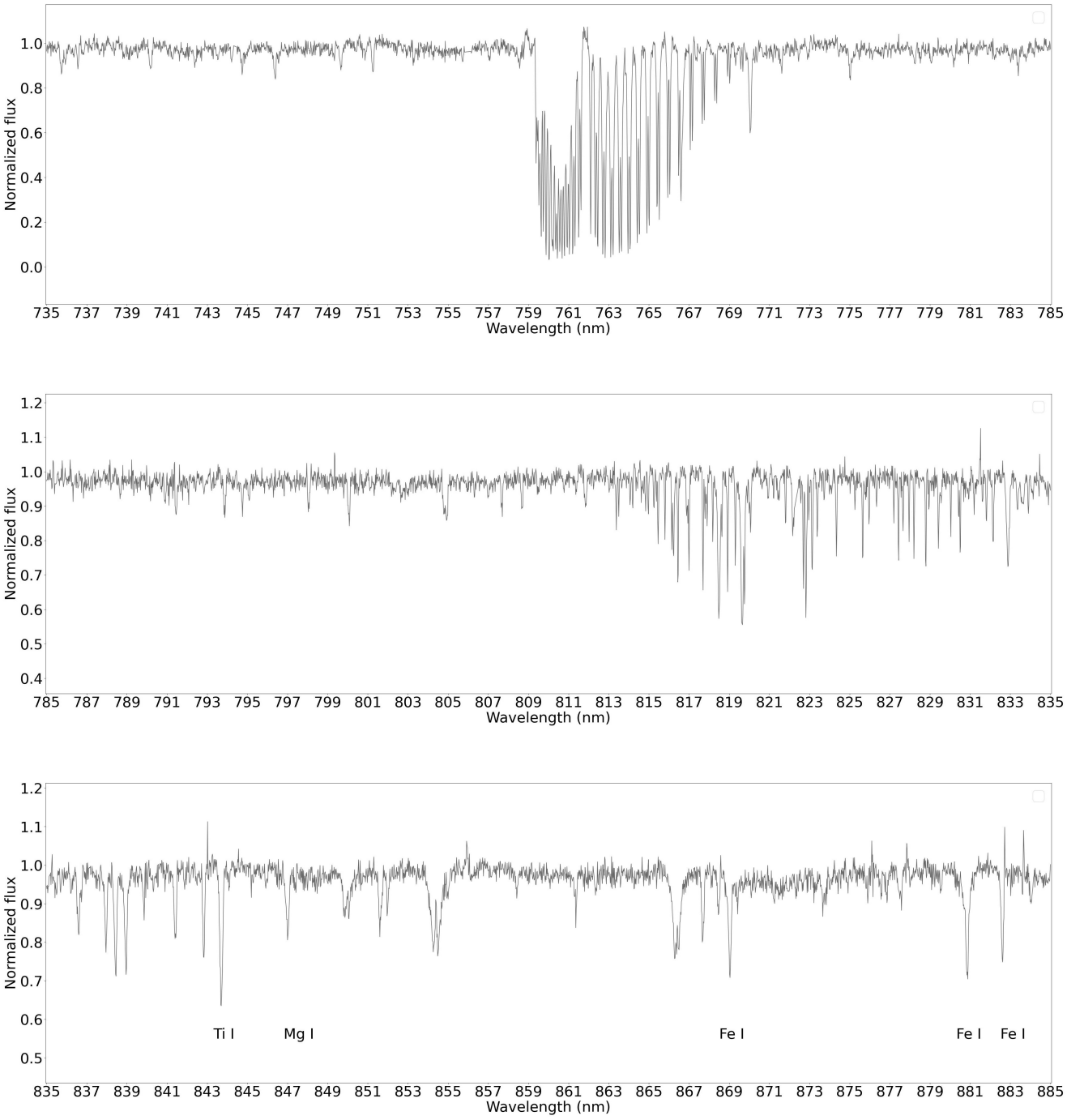

Figure 6.18: Spectral lines identification in 17 VIS spectrum - continued.

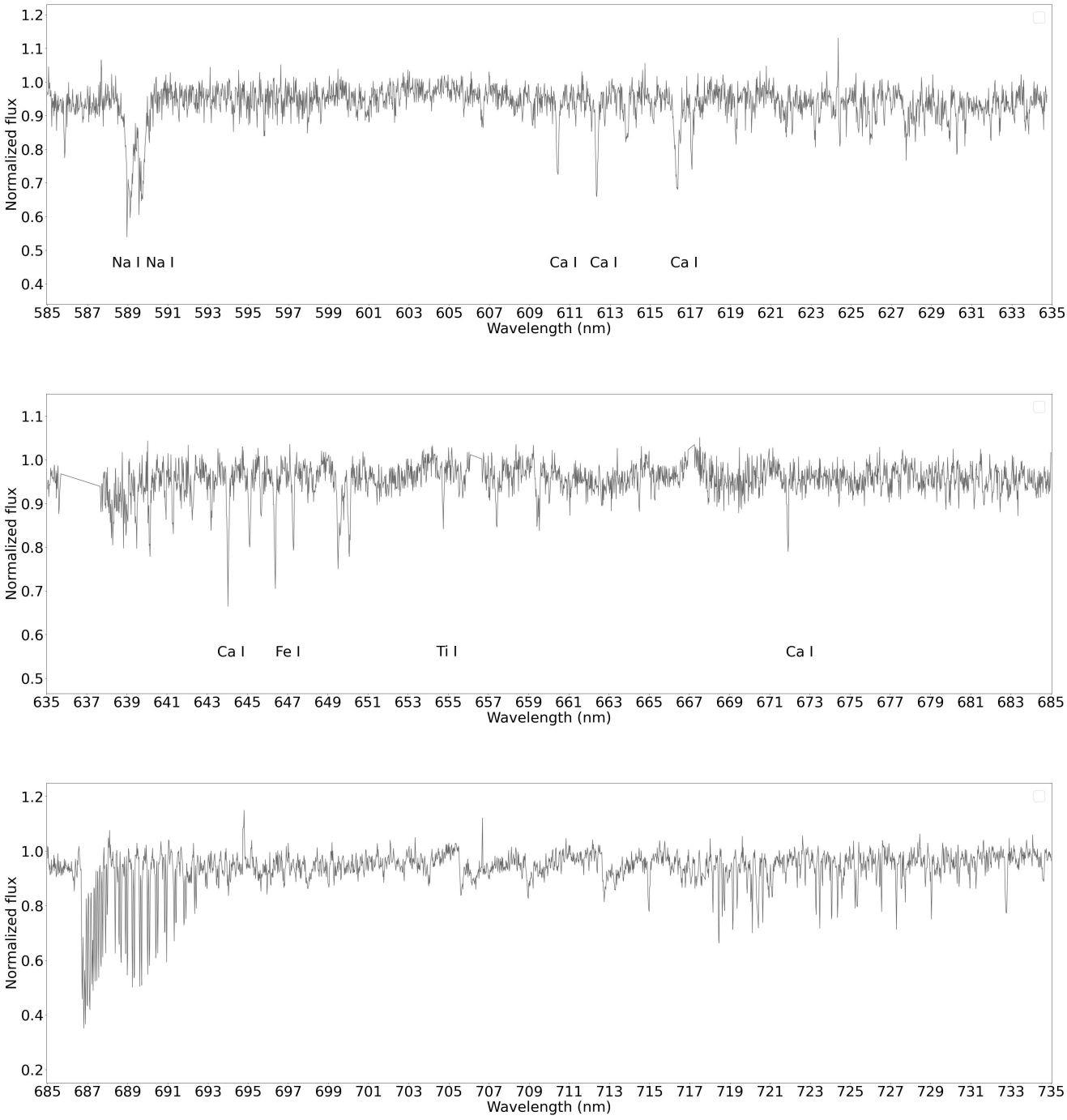

Figure 6.19: Spectral lines identification in 17 VIS spectrum - continued.

As a result of fitting the spectral lines we acquired the needed wavelength estimates of the line centres. Some of the fitted spectral lines can be seen in the figure 6.20.

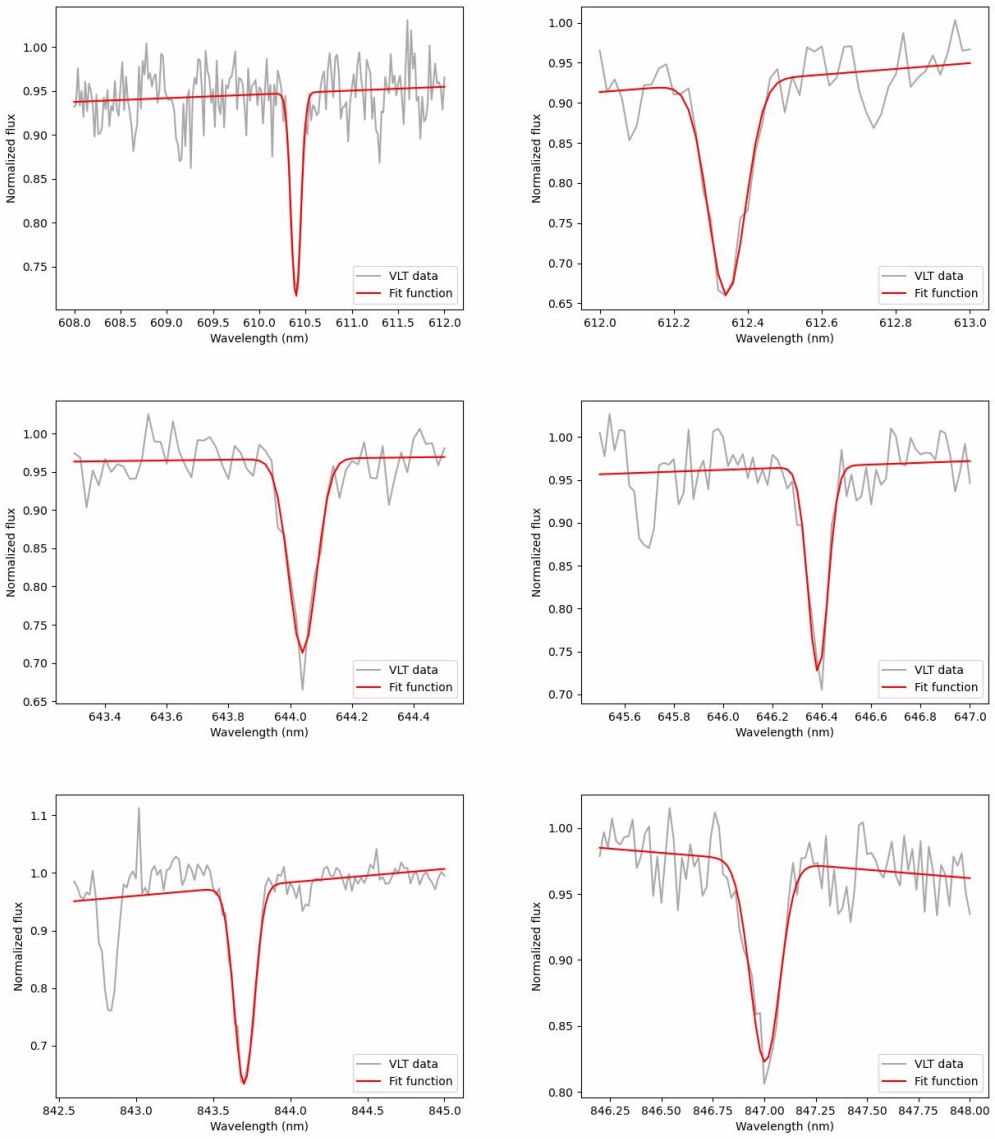

Figure 6.20: Selected identified spectral lines from 17 VIS spectrum. Upper right Ca I 610.2723 nm, upper left Ca I 612.2217 nm, middle right Ca I 643.9075 nm, middle left Fe I 646.4661 nm, lower right Ti I 843.5652 nm and lower left Mg I 846.8849 nm.

As in the case of UVB spectra, the radial velocity was determined. In the tables 6.4 and 6.5 the identified spectral lines with their respect radial velocity from all accessible visual spectra are presented. The mean values of radial velocity from individual VIS spectra are summarized in the table 6.6.

No.	Spectral line	Rest wavelength [nm]	Obs. wavelength [nm]	Radial velocity [km/s]
17	Na I	588.9950	589.0779	42.2
	Na I	589.5924	589.7076	58.6
	Ca I	610.2723	610.3959	60.8
	Ca I	612.2217	612.3432	59.5
	Ca I	616.3755	616.3333	20.6
	Ca I	643.9075	644.0403	61.9
	Fe I	646.4661	646.3844	37.9
	Ti I	654.6269	654.7544	58.4
	Ca I	671.7681	671.9084	62.6
	Ti I	843.5652	843.7018	48.6
	Mg I	846.8849	847.0038	42.1
	Fe I	868.9857	869.0337	16.6
	Fe I	880.8166	880.8488	11.0
	Fe I	882.4221	882.6021	61.2
20	Na I	588.9950	589.0535	29.7
	Na I	589.5924	589.7016	55.5
	Ca I	610.2723	610.3830	54.4
	Ca I	612.2217	612.3377	56.8
	Ca I	616.3755	616.3232	25.5
	Ca I	643.9075	644.0304	57.3
	Fe I	646.4661	646.3731	43.2
	Ti I	654.6269	654.7469	55.0
	Ca I	671.7681	671.8940	56.2
	Ti I	843.5652	843.6881	43.7
	Mg I	846.8849	846.9902	37.3
	Fe I	868.9857	869.0244	13.4
	Fe I	880.8166	880.8384	7.4
	Fe I	882.4221	882.5830	54.7

Table 6.4: Calculated radial velocity from visual spectra.

No.	Spectral line	Rest wavelength [nm]	Obs. wavelength [nm]	Radial velocity [km/s]
23	Na I	588.9950	589.0436	24.7
	Na I	589.5924	589.6644	36.6
	Ca I	610.2723	610.3557	41.0
	Ca I	612.2217	612.3095	11.6
	Ca I	616.3755	616.3022	35.7
	Ca I	643.9075	644.0002	43.2
	Fe I	646.4661	646.3549	51.6
	Ti I	654.6269	654.7224	43.8
	Ca I	671.7681	671.8630	42.4
	Ti I	843.5652	843.6569	32.6
	Mg I	846.8849	846.9606	26.8
	Fe I	868.9857	868.9888	1.1
	Fe I	880.8166	880.8102	2.2
	Fe I	882.4221	882.5533	44.6
26	Na I	588.9950	589.0621	34.1
	Na I	589.5924	589.6969	53.2
	Ca I	610.2723	610.3727	49.4
	Ca I	612.2217	612.3283	52.3
	Ca I	616.3755	616.3131	30.4
	Ca I	643.9075	644.0255	55.0
	Fe I	646.4661	646.3682	45.4
	Ti I	654.6269	654.7332	48.7
	Ca I	671.7681	671.8838	51.7
	Ti I	843.5652	843.6782	40.2
	Mg I	846.8849	846.9876	36.4
	Fe I	868.9857	869.0044	6.5
	Fe I	880.8166	880.8303	4.7
	Fe I	882.4221	882.5799	53.6

Table 6.5: Calculated radial velocity from visual spectra - continued.

No.	Region	Radial velocity [km/s]
17	VIS	49.3 ± 13.7
20	VIS	45.6 ± 12.3
23	VIS	36.7 ± 10.2
26	VIS	44.0 ± 10.1

Table 6.6: Mean values of radial velocity obtained from individual VIS spectra of GD 803.

Once again, we illustrated the the correlation between radial velocity and time. In the figure 6.21 we can see dependence of radial velocity on time expressed in Julian date units. The plot 6.22 shows the relation of radial velocity on phase. For the phase calculation, the same period value was used as for ultraviolet spectra. Under the examination of both radial velocity curves, there is no clear sign of variability. The lack of variability trend in the radial velocity curve can be explained by rather small data sample.

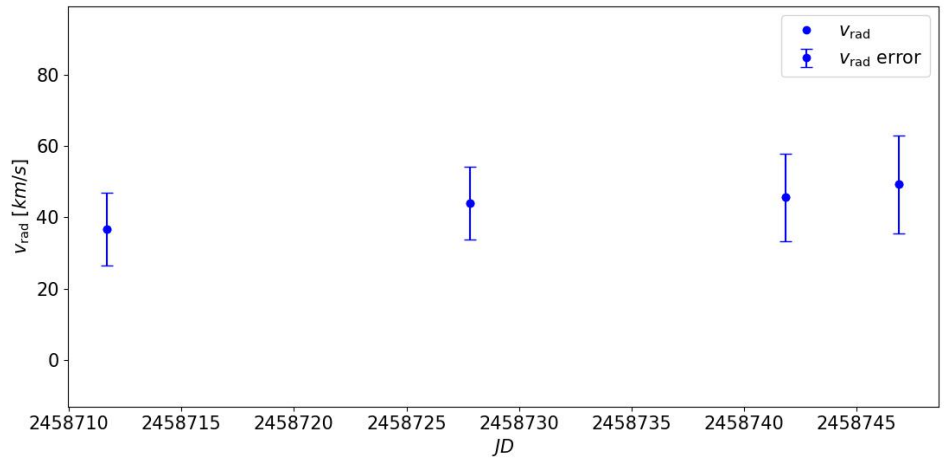

Figure 6.21: Radial velocity curve of GD 803 dependent on Julian Date. The blue points represent radial velocity values and vertical lines are respective error bars for each value.

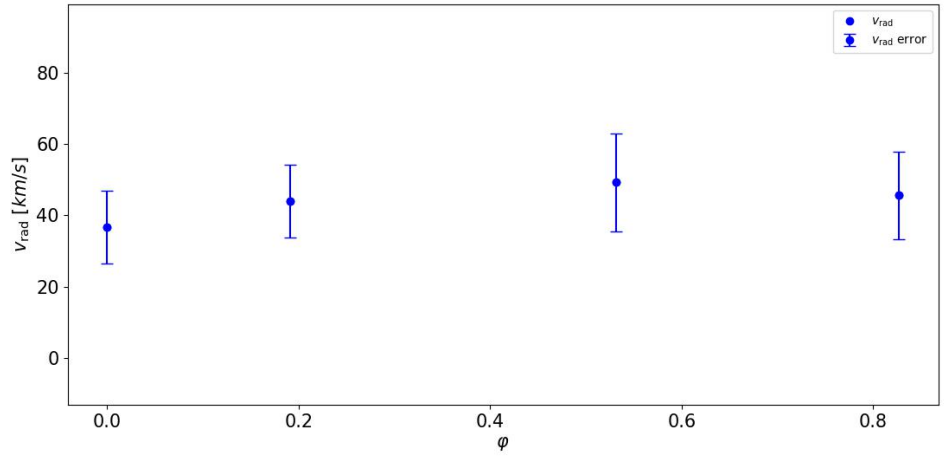

Figure 6.22: Radial velocity curve of GD 803 dependent on phase. The blue points represent radial velocity values and vertical lines are respective error bars for each value.

6.5.4 NIR spectra

The near-infrared spectra did not provide eligible spectral lines for the analysis of radial velocity 6.23.

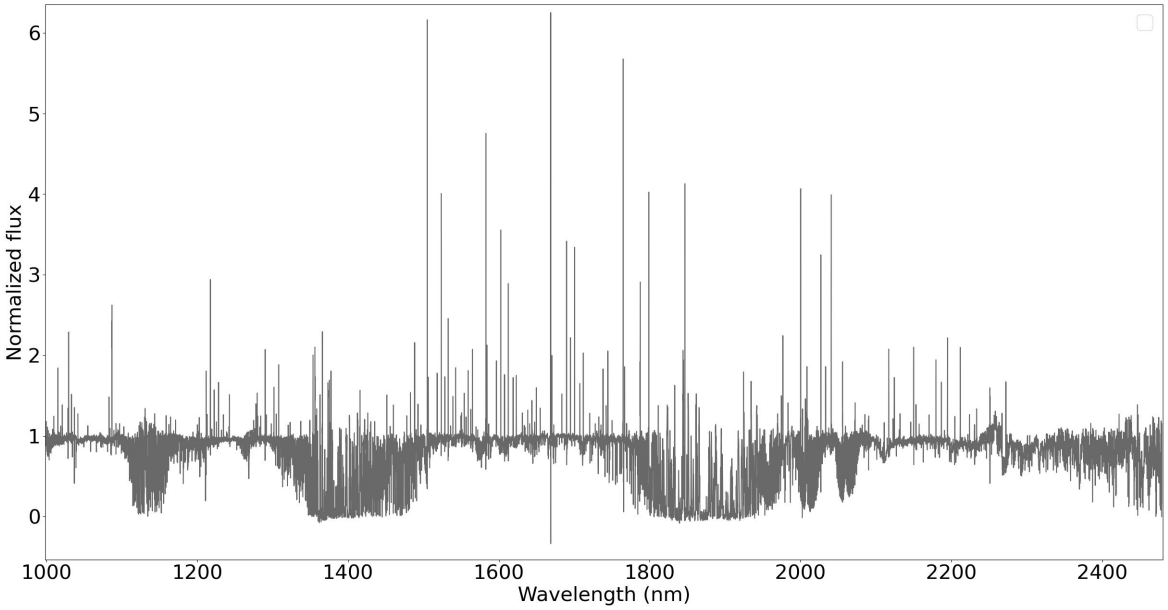

Figure 6.23: NIR wavelength region of 24 spectrum.

6.6 BD+08 102 Spectra

The other analysed star was the white dwarf with identifier BD+08 102.

6.6.1 UVB spectra

The examination of the UVB spectra of object BD+08 102 yielded no apparent white dwarf's spectral lines. The present spectral lines in the UVB region are most likely spectral lines of a cooler component. The ultraviolet spectrum of BD+08 102 is shown in the figure 6.24.

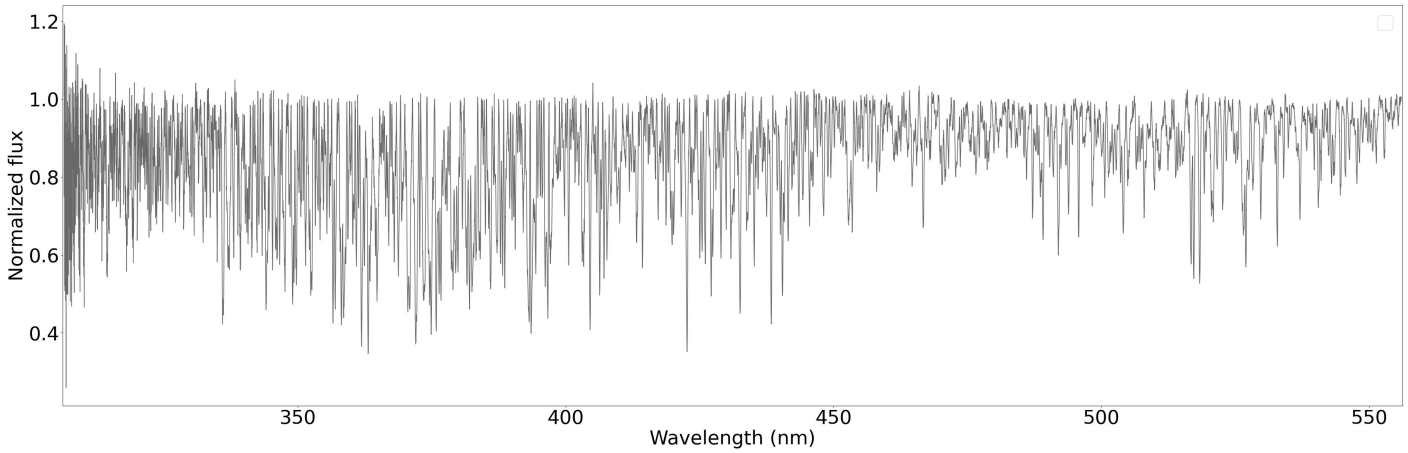

Figure 6.24: 2 spectrum of UVB region of star BD+08 102.

6.6.2 VIS spectra

The analysis of visual wavelength range of the BD+08 102 shows once again narrow spectral lines. These spectral lines most likely belong to the cooler star, possibly the white dwarf's companion. In the spectra, there are strong lines of calcium and iron, but also the sodium doublet same as in the case of GD 803. The identification of spectral lines is presented in figures 6.25, 6.26, 6.27 and in Appendix chapter 6.7.

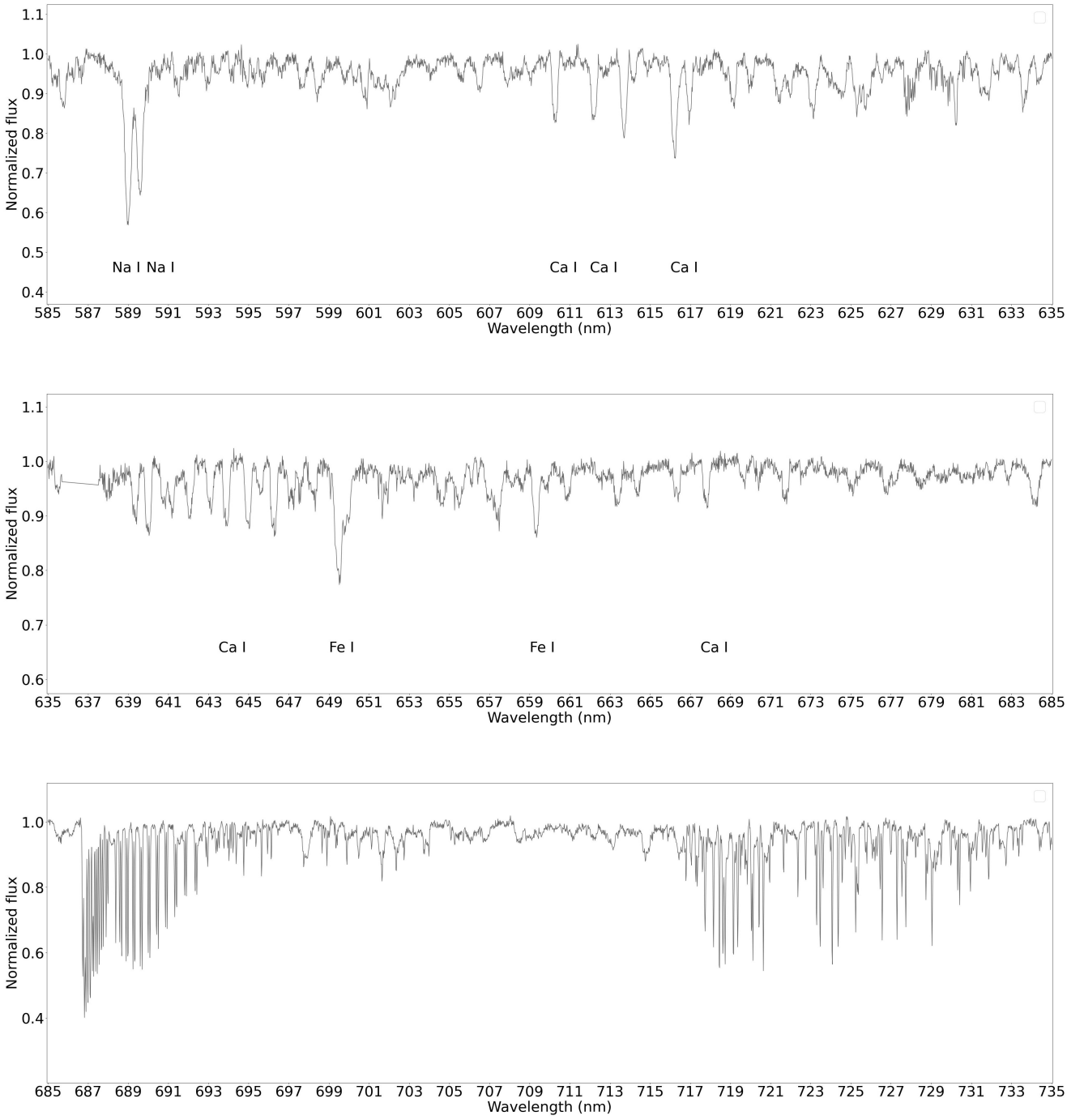

Figure 6.25: Spectral lines identification in 3 VIS spectrum.

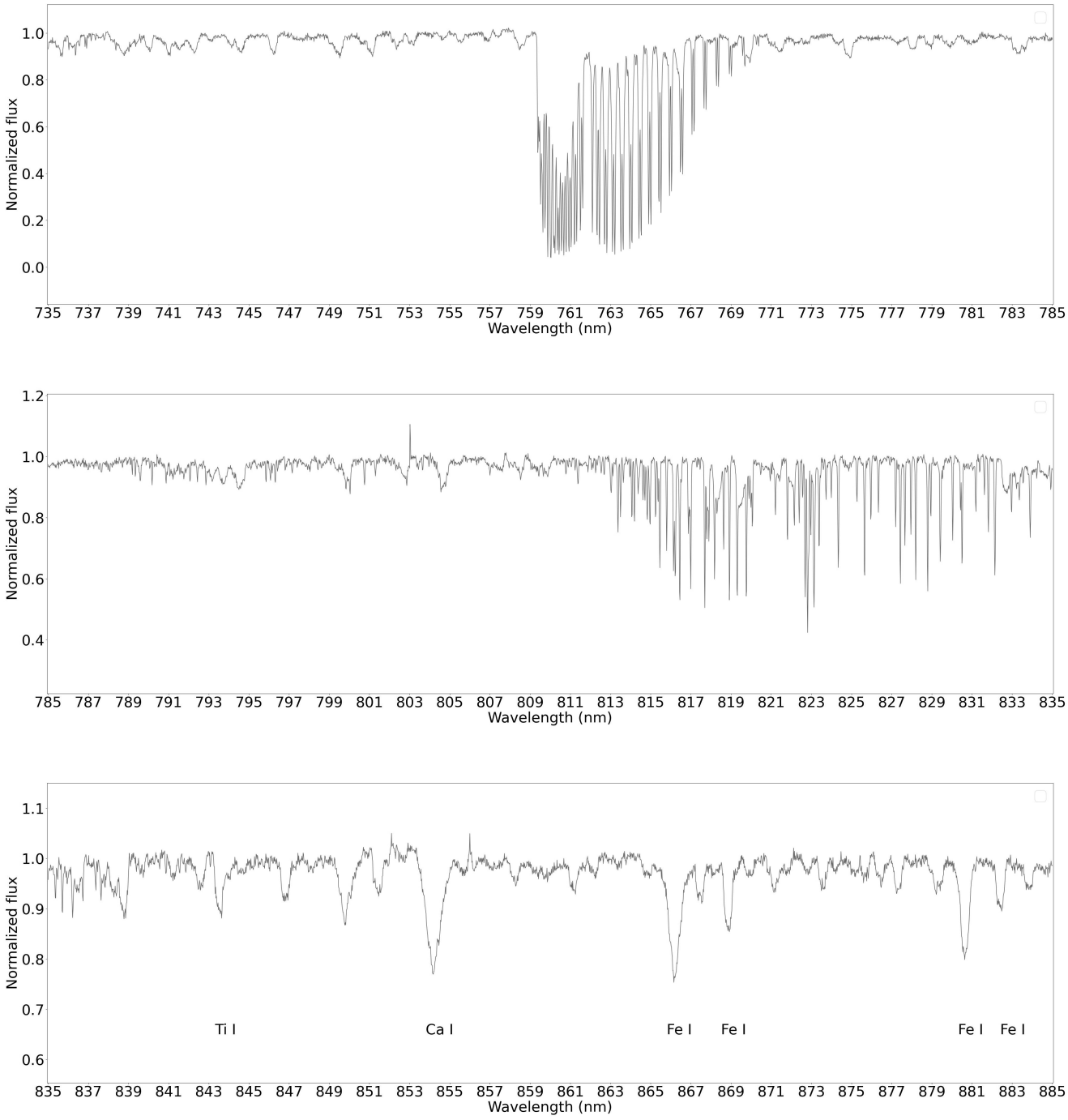

Figure 6.26: Spectral lines identification in 3 VIS spectrum - continued.

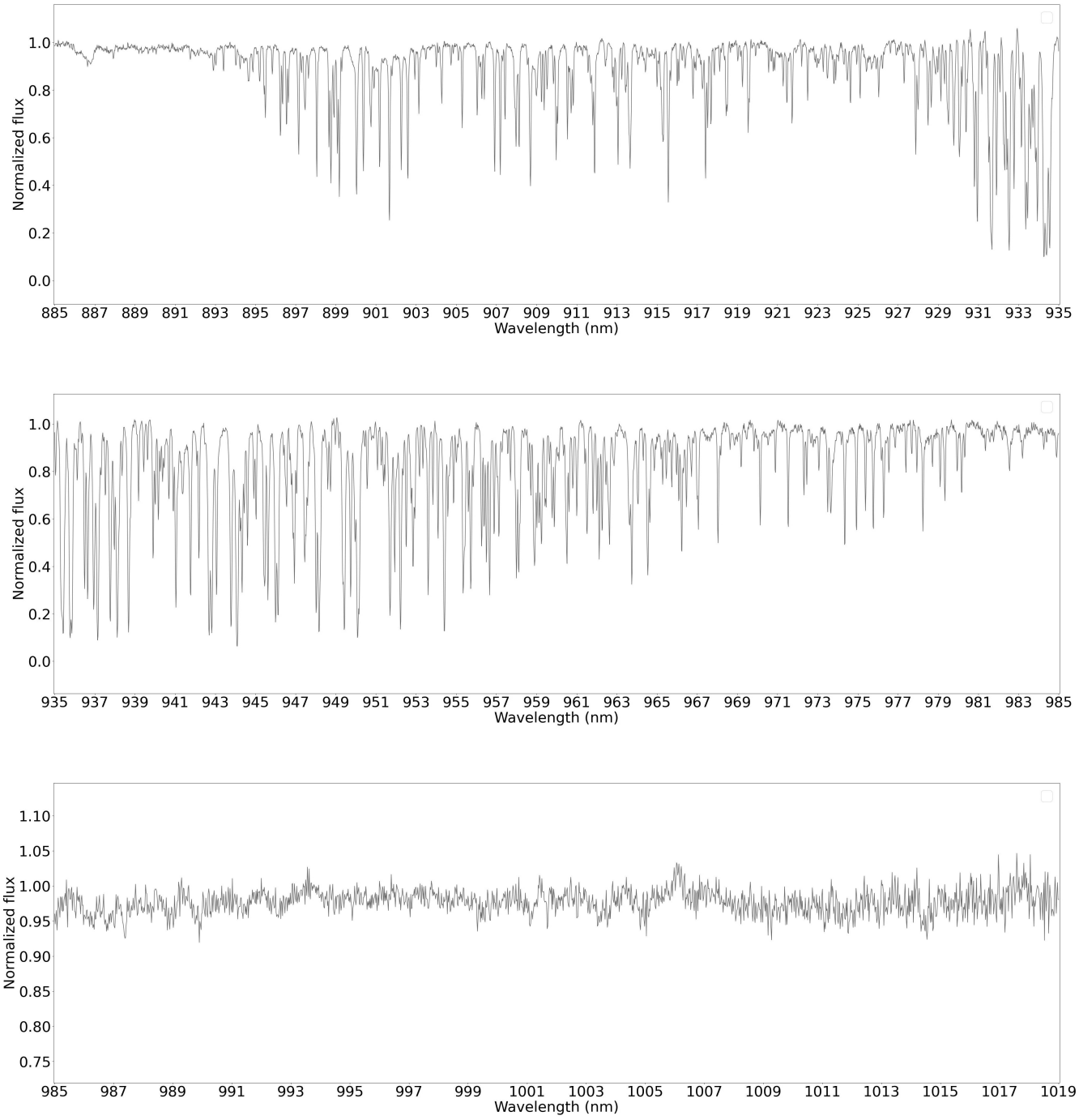

Figure 6.27: Spectral lines identification in 3 VIS spectrum - continued.

The radial velocity determination from the strongest lines identified in visual spectra of the star BD+08 102 are summarized in the tables 6.7 and 6.8.

No.	Spectral line	Rest wavelength [nm]	Obs. wavelength [nm]	Radial velocity [km/s]
3	Na I	588.9950	588.9843	5.5
	Na I	589.5924	589.5954	1.5
	Ca I	610.2723	610.2666	11.2
	Ca I	612.2217	612.1899	15.6
	Ca I	643.9075	643.8930	6.8
	Fe I	649.4980	649.4793	8.7
	Fe I	659.2913	659.3257	15.6
	Fe I	667.7759	667.8043	12.8
	Ti I	843.5652	843.5530	4.3
	Ca I	854.1674	854.1861	6.6
	Fe I	866.1900	866.1982	2.8
	Fe I	868.8626	868.8693	2.3
	Fe I	882.4221	882.4074	5.0
6	Na I	588.9950	589.0108	8.0
	Na I	589.5924	589.6216	14.9
	Ca I	610.2723	610.2996	27.4
	Ca I	612.2217	612.2274	2.8
	Ca I	643.9075	643.9228	7.2
	Fe I	649.4980	649.5038	2.7
	Fe I	659.2913	659.3542	28.6
	Fe I	667.7759	667.8336	25.9
	Ti I	843.5652	843.5852	7.1
	Ca I	854.1674	854.2246	20.1
	Fe I	866.1900	866.2287	13.4
	Fe I	868.8626	868.8962	11.6
	Fe I	882.4221	882.4373	5.2

Table 6.7: Calculated radial velocity from visual spectra of star BD+08 102.

No.	Spectral line	Rest wavelength [nm]	Obs. wavelength [nm]	Radial velocity [km/s]
9	Na I	588.9950	588.9659	15.0
	Na I	589.5924	589.5780	7.4
	Ca I	610.2723	610.2516	3.8
	Ca I	612.2217	612.1851	17.9
	Ca I	643.9075	643.8789	13.3
	Fe I	649.4980	649.4714	12.3
	Fe I	659.2913	659.3116	9.2
	Fe I	667.7759	667.7791	1.5
	Ti I	843.5652	843.5443	7.4
	Ca I	854,1674	854.1681	0.3
	Fe I	866.1900	866.1744	5.4
	Fe I	868.8626	868.8483	4.9
	Fe I	882.4221	882.3828	13.3
12	Na I	588.9950	588.9685	13.6
	Na I	589.5924	589.5842	4.2
	Ca I	610.2723	610.2500	3.0
	Ca I	612.2217	612.1840	18.5
	Ca I	643.9075	643.8751	15.1
	Fe I	649.4980	649.4637	15.9
	Fe I	659.2913	659.3047	6.1
	Fe I	667.7759	667.7753	0.3
	Ti I	843.5652	843.5319	11.8
	Ca I	854.1674	854.1590	3.0
	Fe I	866.1900	866.1676	7.8
	Fe I	868.8626	868.8426	6.9
	Fe I	882.4221	882.3807	14.1
15	Na I	588.9950	588.9909	2.1
	Na I	589.5924	589.6079	7.9
	Ca I	610.2723	610.2713	13.5
	Ca I	612.2217	612.1979	11.7
	Ca I	643.9075	643.8937	6.4
	Fe I	649.4980	649.4871	5.1
	Fe I	659.2913	659.3293	17.3
	Fe I	667.7759	667.8145	17.3
	Ti I	843.5652	843.5599	1.9
	Ca I	854.1674	854.1960	10.1
	Fe I	866.1900	866.2107	7.2
	Fe I	868.8626	868.8563	2.2
	Fe I	882.4221	882.4030	6.5

Table 6.8: Calculated radial velocity from visual spectra of star BD+08 102- continued.

The radial velocity curve of the star BD+08 102 can be seen in the figure 6.28. The mean values of radial velocity obtained from individual spectra are shown in the table 6.9. The dependence of radial velocity on phase is illustrated in the figure 6.29. Photometric period used for the phase calculation was derived by prof. Mikulášek and is equal to 0.416486 d. The epoch in this case is $t_0 = 2458669.9168$ d.

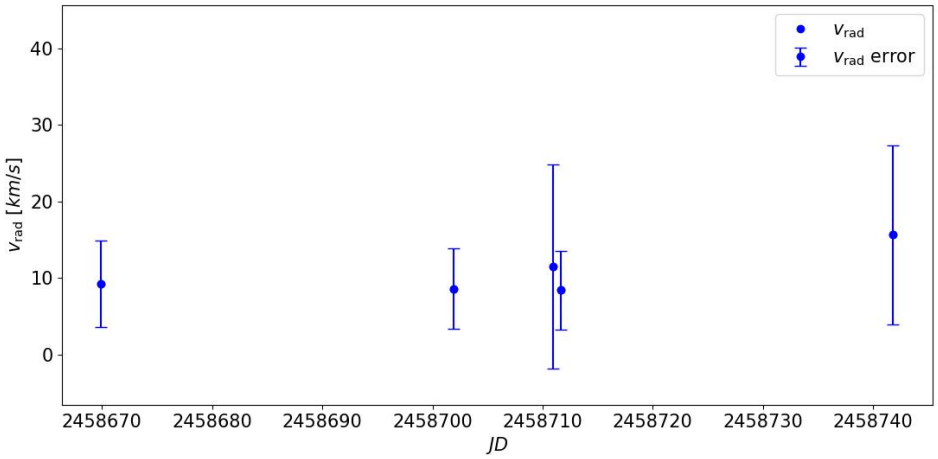

Figure 6.28: Radial velocity curve of BD+08 102 dependent on Julian Date. The blue points represent radial velocity values and vertical lines are respective error bars for each value.

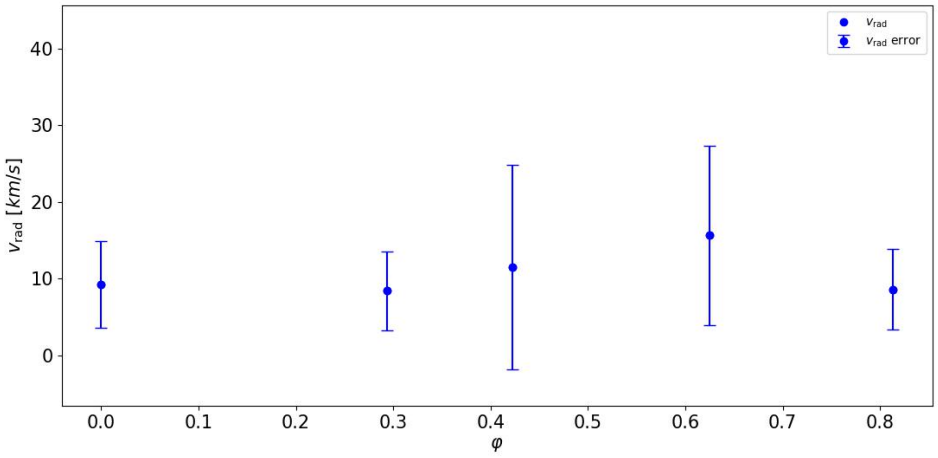

Figure 6.29: Radial velocity curve of BD+08 102 dependent on phase. The blue points represent radial velocity values and vertical lines are respective error bars for each value.

No.	Region	Radial velocity [km/s]
3	VIS	11.5 ± 13.3
6	VIS	15.6 ± 11.7
9	VIS	8.6 ± 5.2
12	VIS	9.2 ± 5.6
15	VIS	8.4 ± 5.1

Table 6.9: Mean values of radial velocity obtained from individual VIS spectra of BD+08 102.

6.7 Discussion

Stellar spectra analysis provided us with the estimation of the radial velocity curves of both stars GD 803 and BD+08 102.

We were able to plot the radial velocity from UVB spectra from hydrogen Balmer lines for the object GD 803, as well as the radial velocity curve from the VIS region of the spectra. The measured radial velocities differ between UVB and VIS observation of this star. This most likely concludes that the UVB hydrogen lines originate from white dwarf while the spectral lines from VIS region belong to the secondary stellar companion. In the case of BD+08 102, we obtained radial velocity curve from VIS wavelength range. No broad hydrogen lines were present in the spectra of BD+08 102.

We performed calculation of orbital separation of the stellar components in the binary system using third Kepler law 6.5.

$$\frac{a^3}{P^2} = \frac{G(M_1 + M_2)}{4\pi^2}. \tag{6.5}$$

The G represents gravitational constant $G = 6.674310^{-11}\mathrm{m}^3\mathrm{kg}^{-1}\mathrm{s}^{-2}$, M_1 and M_2 are the masses of the stars, P is the orbital period and a denotes the semi-major axis or the orbital separation of the two stars.

From the period derived from photometry $P = 0.471987$ d and the estimates of the masses $M_{\mathrm{WD}} = 0.55$ $\mathrm{M}_\odot$, $M_{\mathrm{C}} = 1.15$ $\mathrm{M}_\odot$ (Rebassa-Mansergas et al., 2010 [33]), we can determine the value of a. Hence the orbital separation of the GD 803 would be $a = 3.04$ $\mathrm{R}_\odot$.

The same calculation can be done for the other star BD+08 102 with photometric period $P = 0.416486$ d and masses of the two components $M_{\mathrm{WD}} = 0.39$ $\mathrm{M}_\odot$, $M_{\mathrm{C}} = 0.84$ $\mathrm{M}_\odot$ (Holberg et al., 2013 [16]). Kepler third law's result for the orbital separation calculation of BD+08 102 gives $a = 2.51\mathrm{R}_\odot$.

To look further into results from the radial velocity variations we estimated the expected value of semi-amplitude of radial velocity K. The relation between the semi-amplitude $K = K_1 + K_2$ and semi-major axis $a = a_1 + a_2$ is shown in the equation 6.6 (Benaquista, 2013 [7]).

$$K_1 + K_2 = \frac{2\pi \sin i}{P\sqrt{1-e^2}}(a_1 + a_2). \tag{6.6}$$

The i is inclination, e is eccentricity of the trajectory and P is the orbital period. In our calculation we assumed the inclination $i = 90$ ° and circular orbit $e = 0$. The assumption comes from the observations of the spectroscopic binaries. Since the spectroscopic binaries

are not possible to resolve visually we assume they tend to form close binary stellar systems. In such binary, tidal interactions between the stars cause the orbits to become almost circular. Hence, the orbital eccentricity $e \ll 1$. When the orbital plane of the system lies in the line of sight of the observer $i = 90°$, we expect the observed radial velocity curves form a sinusoidal shape (Carrol & Ostlie, 2007 [10]). Given the assumptions made, we consider these results to be an estimate rather than precise values.

The estimated semi-amplitude of radial velocity is $K = 326.4$ km/s for GD 803. The BD+08 102 semi-amplitude estimation yielded in result $K = 305.5$ km/s. It is possible to determine the value of radial velocity semi-amplitude from observation as half of the difference between minimum and maximum of the observed radial velocity 6.7 (Benaquista, 2013 [7]).

$$K = \frac{1}{2}(v_{\max} - v_{\min}) \tag{6.7}$$

The observed semi-amplitude of GD 803 the radial velocity curve is $K_{\mathrm{UVB}} = 103.4$ km/s and $K_{\mathrm{VIS}} = 6.3$ km/s. Figures 6.30 and 6.31 show radial velocity curves of GD 803 obtained from UVB and VIS spectra. We fitted the observed values by sine wave function $f(\varphi) = a\sin(2\pi\varphi + b)$.

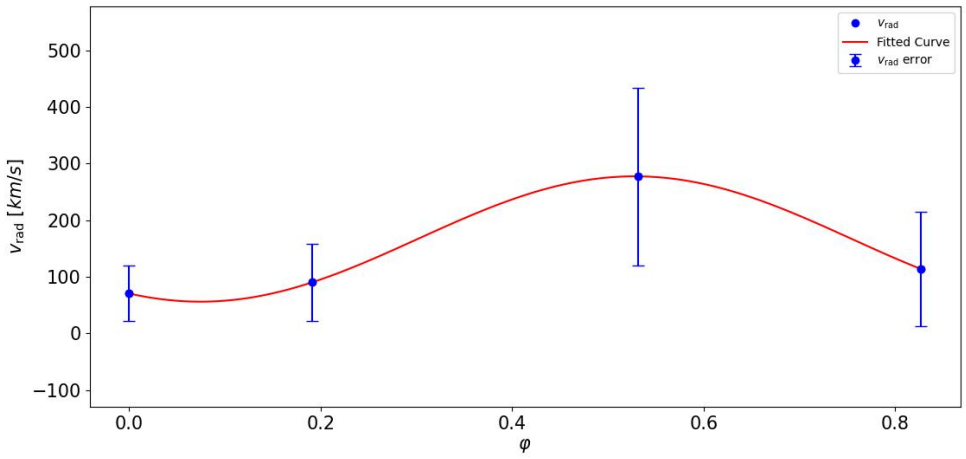

Figure 6.30: Radial velocity curve of GD 803 derived from UVB spectra. The radial velocity curve was fitted by sine wave function.

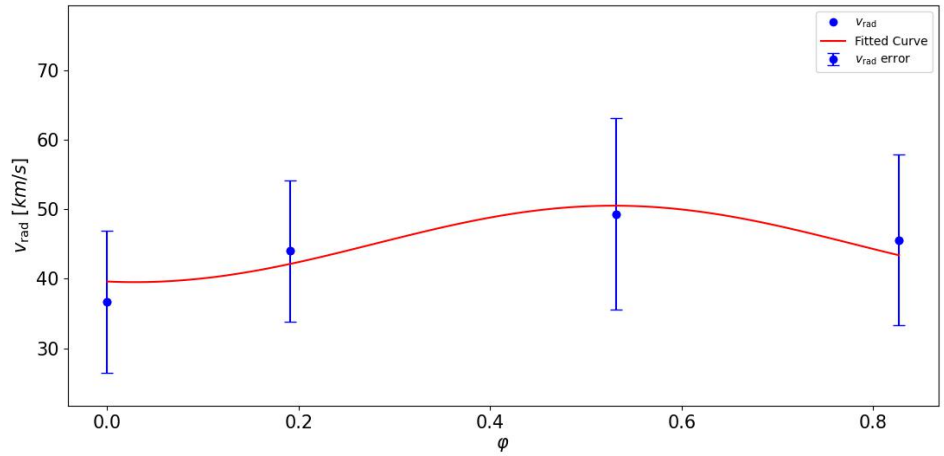

Figure 6.31: Radial velocity curve of GD 803 derived from VIS spectra. The radial velocity curve was fitted by sine wave function.

In the case of BD+08 102, we were not able to identify spectral lines from UVB spectra. Thus, we can only establish the semi-amplitude from VIS region of wavelengths. Since the measurement of the other radial velocity curve is not possible for both components, we used the relation, where only one star's spectral lines are accessible 6.8 (Carrol & Ostlie, 2007 [10]).

$$M_1 + M_2 = \frac{P}{2\pi G} \frac{K_1^3}{\sin^3 i} \left(1 + \frac{M_1}{M_2}\right)^3 \tag{6.8}$$

From the equation 6.8 the estimated semi-amplitude of radial velocity $K_1 = 96.9$ km/s. In the figure 6.32, there is phase folded radial velocity curve of BD+08 102. The observed semi-amplitude in the case of BD+08 102 is 7 km/s. The discrepancy between the estimate and observation is substantial. For the estimation of semi-amplitude as well as orbital separation we used the period which was obtained from photometry. Thus, the photometric period can be in fact only the rotational period of the star and not the orbital period as thought before. This would explain why the values don't match.

The fitted sine wave function in the radial velocity curves shows slight periodic variability in the radial velocity. However, it is important to emphasize that our radial velocity values were determined with large uncertainty. This uncertainty affected our results and so the changes in the radial velocity may be due to the uncertainty of determining the radial velocities and not the actual variability of these stars.

We also tested whether the photometric light variations could be reproduced by reflection effect in binary system. Model light curves of irradiated binary were calculated from input stellar parameters with code made by prof. Krtička (Krtička et al., 2023 [23]) . The model predicts amplitude of light variations for GD 803 to be 0.26 mag for inclination $i = 90°$. Hence, the light curve of GD 803 could result from reflection effect. For the star BD+08 102 the modeled amplitude was 0.006 mag, so in this case the reflection effect does not explain the photometric variability. The larger predicted amplitude in GD 803 is given by its higher effective temperature.

As previously mentioned in 5.1 the star BD+08 102 is classified as cataclysmic binary in Simbad [E3]. Nonetheless, our analysis indicates that a symbiotic binary is the more likely scenario.

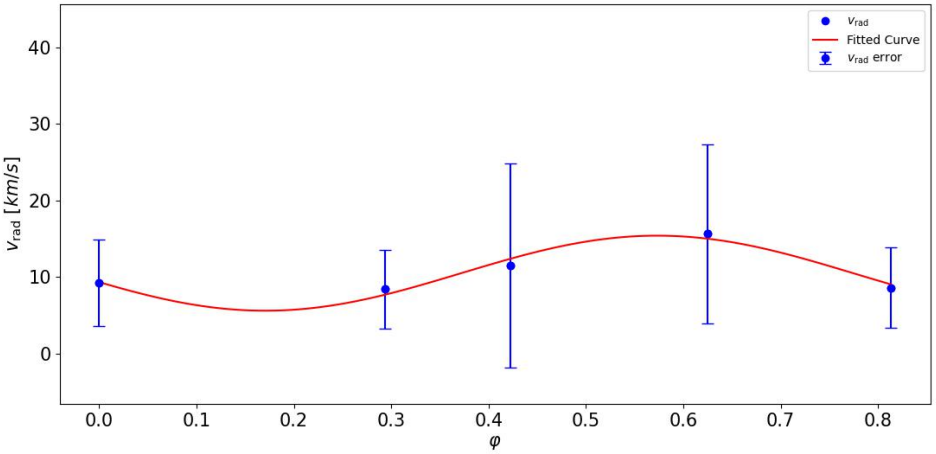

Figure 6.32: Radial velocity curve of BD+08 102 derived from VIS spectra. The radial velocity curve was fitted by sine wave function.

Conclusions

In this work we analysed the spectra of two photometrically variable white dwarfs with identifiers BD+08 102 and GD 803. The periodic light variability of these stars was detected thanks to Kepler mission and our goal in this work was to explain the origin of these changes by performing spectral analysis.

We determined the radial velocity curves from obtained X-shooter data and analyzed the possible periodic variability in radial velocity.

In the case of the star BD+08 102 we were able to identify spectral lines in the VIS part of the spectra. The strongest spectral lines used for the radial velocity measurements were sodium, calcium, magnesium and iron absorption spectral lines. Radial velocity curve shows the slight periodic nature after we plotted the radial velocity as a function of phase with period determined from photometry. However, the measured radial velocity was clouded by significant error therefore the changes in radial velocity values can arise from uncertainties. We also estimated the expected orbital separation of the two stellar components with the assumption of the binary origin. The orbital separation estimation yielded in result $a = 2.51$ R$_\odot$. From the approximate of the orbital separation we could determine the predicted semi-amplitude of the radial velocity $K = 96.9$ km/s. Observation and radial velocity calculation resulted in value $K = 7$ km/s. This result is unfortunately not consistent with observation. The inconsistency of the results can be interpreted in several ways. We assumed that the period derived from photometry is the orbital period of the binary, this affected the deviation of the observed and predicted semi-amplitudes. The other simplification we used when estimating the semi-amplitude was inclination angle to be $i = 90\ ^\circ$. If the actual inclination angle of the binary was small, the estimated semi-amplitude of the radial velocity would correspond to the observed value better. Lastly, the star BD+08 102 itself could be a single star and the periodic light variability has different origin.

The spectral analysis of the star GD 803 introduced better results. The process of identification of the spectral lines provided us with results from UVB and VIS region of wavelengths. In the UVB spectra there were prominent hydrogen absorption lines of Balmer series. We encounter such broadened lines among the white dwarf's spectra. The wide profiles of these lines are result of pressure broadening. In the VIS part of the spectra we once again identified narrow lines of heavier elements such as calcium or iron. Since the radial velocity measurement was eligible both from UVB and VIS region, we could plot radial velocity curves from both regions and compare them. As it was in the case of BD+08 102 we tried to make an estimate of the semi-amplitude of the radial velocity. From the third Kepler law we established the orbital separation of the binary using the photometric period, which gave us the result $a = 3.04$ R$_\odot$. The estimated semi-amplitude

of radial velocity was $K = 326$ km/s. The calculation of the radial velocity in the case of UVB region resulted in $K_{\mathrm{UVB}} = 103$ km/s. The measurement of radial velocity from VIS region yielded in value $K_{\mathrm{VIS}} = 6.3$ km/s. Comparing this result with the observed semi-amplitude we arrived to disagreement of observation and prediction once again. The actual orbital period could be longer than the period estimated from photometry. Hence, the inspection of the radial velocity variability did not provide sufficient proof of binary origin. Once again, the determined radial velocity values are clouded by error and so the variability in radial velocities could be in fact conditioned by this error. However, the central parts of the Balmer spectral lines showed apparent emissions. These emissions suggest the presence of material from winds of the cooler stellar component ionized by white dwarf and can serve as an indication of binary origin.

Another result we obtained from the spectral analysis of GD 803 was the possible presence of ultra-high excitation line at 478 nm. Only a small fraction of hot white dwarfs are showing such UHE spectral lines and the cause of origin is yet to be explained.

Light variations could be explained by reflection effect in the case of binary system. We obtained results from modeled light curve with assumption that the photometric variations are caused by irradiation. For the star GD 803 the modeled reflection effect light predicts amplitude 0.27 mag . Therefore, in principle, the light curve could be given by reflection. In the case of BD+08 102 the resulting amplitude from the model is 0.006 mag, which means that light changes cannot be caused by reflection effect. The observed light curve of BD+08 102 shows variable amplitude of light changes, the probable explanation is that the star has time-varying spots on its surface.

Bibliography

[1] Blaauw A. *ESO's Early History*. European Southern Observatory, 1991. ISBN 3-923524-40-4.

[2] Althaus, L. G., Córsico , A. H., Isern , J., and García-Berro , E. Evolutionary and pulsational properties of white dwarf stars. *The Astronomy and Astrophysics Review*, 18:471, 2010.

[3] Barstow, M. A., Bond, Howard E., Burleigh, M. R., and Holberg, J. B. Resolving Sirius-like binaries with the Hubble Space Telescope. *Monthly Notices of the Royal Astronomical Society*, 322:891, 2001.

[4] Barstow, M. A., Holberg, J. B., Fleming, T. A., Marsh, M. C., Koester, D., and Wonnacott, D. A ROSAT survey of hot DA white dwarfs in non-interacting binary systems. *Monthly Notices of the Royal Astronomical Society*, 270:499, 1994.

[5] Bauer, E. B. and Kupfer, T. Phases of mass transfer from hot subdwarfs to white dwarf companions and their photometric properties. *The Astrophysical Journal*, 922:245, 2021.

[6] Bédard, A., Bergeron, P., Brassard, P., and Fontaine, G. On the Spectral Evolution of Hot White Dwarf Stars. I. A Detailed Model Atmosphere Analysis of Hot White Dwarfs from SDSS DR12. *The Astrophysical Journal*, 901:93, 2020.

[7] Benacquista, M. *An Introduction to the Evolution of Single and Binary Stars*. 2013. ISBN 978-1-4419-9990-0.

[8] Buscombe, W. The Characteristics of Subdwarf Stars. *Journal of the Royal Astronomical Society of Canada*, 53:7, 1959.

[9] Camenzind, M. *Compact objects in astrophysics : white dwarfs, neutron stars, and black holes*. Springer Berlin Heidelberg, 2007. ISBN 978-3-540-25770-7.

[10] Carroll, B. W. and Ostlie, D. A. *An Introduction to Modern Astrophysics*. Cambridge University Press, 2007. ISBN 9781108422161.

[11] Fontaine, G., Brassard, P., and Bergeron, P. The Potential of White Dwarf Cosmochronology. *Publications of the Astronomical Society of the Pacific*, 113:409, 2001.

[12] Gaia Collaboration. VizieR Online Data Catalog: Gaia EDR3 (Gaia Collaboration, 2020). VizieR On-line Data Catalog: I/350. Originally published in: 2021A&A...649A...1G; doi:10.5270/esa-1ug, November 2020.

[13] Groot, P. J. Rotational Doppler Beaming in Eclipsing Binaries. *Astronomy & Astrophysics Library*, 745:55, 2012.

[14] Heber, U. Hot Subluminous Stars. *Publications of the Astronomical Society of the Pacific*, 128, 2016.

[15] Hills, J. G. and Dale, T. M. The orbit evolution of the eclipsing binary system BD +16 516 and the rotation period of its white dwarf. *Astronomy & Astrophysics Library*, 30:135, 1974.

[16] Holberg, J. B., Oswalt, T. D., Sion, E. M., Barstow, M. A. , and Burleigh, M. R. Where are all the Sirius-like binary systems? *Monthly Notices of the Royal Astronomical Society*, 435:2077, 2013.

[17] Holberg, J.B. What fraction of white dwarfs are members of binary systems? *Journal of Physics: Conference Series*, 172, 2009.

[18] Howell, S. B., Sobeck, C., and Haas, M. et al. The K2 Mission: Characterization and Early Results. *Publications of the Astronomical Society of the Pacific*, 126:398, 2014.

[19] Hubeny, I. and Lanz, T. A brief introductory guide to TLUSTY and SYNSPEC. *arXiv e-prints*, page arXiv:1706.01859, 2017.

[20] Kawka , A. and Vennes, S. White Dwarf Companions to Luminous Stars. In Prša, A. and Zejda, M., editors, *Binaries - Key to Comprehension of the Universe*, volume 435 of *Astronomical Society of the Pacific Conference Series*, page 189, 2010.

[21] Kellett, B. J., Bromage , G. E., and Brown, A. et al. RE 0044+09: A New K Dwarf Rapid Rotator with a White Dwarf Companion? *The Astrophysical Journal*, 438:364, 1995.

[22] Kippenhahn, R., Weigert, A. , and Hofmeister , E. Methods for Calculating Stellar Evolution. *Methods in Computational Physics*, 7:129, 1967.

[23] Krtička, J., Kawka, A., Mikulášek, Z., Fossati, L., Krtičková, I., Prvák, M., Janík, J., Liptaj, R., Zejda, M., and Paunzen, E. Epic 206197016: A very hot white dwarf orbited by a strongly irradiated red dwarf. *Astronomy & Astrophysics*, 674:A94, 2023.

[24] Lauterborn , D. Evolution with mass exchange of case C for a binary system of total mass 7 Msun. *Astronomy & Astrophysics*, 7:150, 1970.

[25] Marchant, P. and Bodensteiner, J. The Evolution of Massive Binary Stars. 2023.

[26] Mason, K. O., Hassall, B. J. M., and Bromage, G. E. et.al. Optical identification of EUV sources from the ROSAT Wide Field Camera all-sky survey. *Monthly Notices of the Royal Astronomical Society*, 274:1194, 1995.

[27] Mikolajewska, J. Symbiotic Stars: Continually Embarrassing Binaries. *Baltic Astronomy*, 16:1, 2007.

[28] Mikulášek, Z. and Krtička, J. *Základy fyziky hvězd*. 2005.

[29] Mikulášek, Z. and Zejda, M. *Proměnné hvězdy*. 2013.

[30] Negu S. H. and Tessema S. B. Mass Transfer in Binary Stellar Evolution and Its Stability. *International Journal of Astronomy and Astrophysics*, 5:222, 2015.

[31] Nipoti, C. Celestial mechanics. *Dipartimento di Fisica e Astronomia, Universita di Bologna*, 2018.

[32] Podsiadlowski, P. The evolution of binary systems. *Accretion Processes In Astrophysics: XXI Canary Islands Winter School Of Astrophysics*, page 45, 2012.

[33] Rebassa-Mansergas, A., Gänsicke, B. T., and Schreiber, M. R. et al. Post-common envelope binaries from sdss - vii. a catalogue of white dwarf-main sequence binaries: A catalogue of wdms binaries. *Monthly Notices of the Royal Astronomical Society*, 402:620, 2009.

[34] Reindl, N., Schaffenroth, V., Filiz, S., Geier, S., Pelisoli, I., and Kepler, S. O. Mysterious, variable, and extremely hot: White dwarfs showing ultra-high excitation lines. I. Photometric variability. *Astronomy & Astrophysics*, 647:A184, 2021.

[35] Saumon, D., Blouin, S., and Tremblay, P.-E. . Current challenges in the physics of white dwarf stars. *Physics Reports*, 988:1, 2022.

[36] Shapiro, S. L. and Teukolsky, S. A. *Black holes, white dwarfs and neutron stars. The physics of compact objects*. 1983. ISBN 9780471873167.

[37] Thomas, H. C. Consequences of mass transfer in close binary systems. *Annual Review of Astronomy and Astrophysics*, 15:127, 1977.

[38] Toonen, S., Hollands, M., Gänsicke, B. T., and Boekholt, T. The binarity of the local white dwarf population. *Astronomy & Astrophysics Library*, 602, 2017.

[39] Werner, K., Dreizler, S., Heber, U., Rauch, T., Wisotzki, L., and Hagen, H. -J. Discovery of two hot DO white dwarfs exhibiting ultrahigh-excitation absorption lines. *Astronomy & Astrophysics*, 293:L75, 1995.

[40] Zucker , S., Mazeh , T., and Alexander , T. Beaming Binaries: A New Observational Category of Photometric Binary Stars. *The Astrophysical Journal*, 670:1326, 2007.

Electronic sources

[E1] SPLAT VO: Spectral Analysis Tool.
https://www.g-vo.org/pmwiki/About/SPLAT

[E2] Python Software Foundation. Python Language Reference, version 3.7.
http://www.python.org

[E3] CDS/SIMBAD. Centre de données astronomiques de Strasbourg.
https://simbad.cds.unistra.fr/simbad/

[E4] Sloan Digital Sky Survey data release 6.
https://classic.sdss.org/dr6/

[E5] ESO - the European Southern Observatory.
https://www.eso.org/public/about-eso/

[E6] ESO - the European Southern Observatory, VLT.
https://www.eso.org/public/teles-instr/paranal-observatory/vlt/

[E7] ESO - the European Southern Observatory, X-shooter.
https://www.eso.org/public/teles-instr/paranal-observatory/vlt/vlt-instr/x-shooter/

[E8] NASA - Kepler mission.
https://science.nasa.gov/mission/kepler

[E9] NASA - Kepler mission K2.
https://www.nasa.gov/image-article/keplers-second-light-how-k2-will-work/

[E10] NASA - Kepler second light.
https://www.nasa.gov/kepler/a-sunny-outlook-for-nasa-keplers-second-light

[E11] Space - Kepler space telescope.
https://www.space.com/24903-kepler-space-telescope.html

[E12] NASA - Kepler properties.
https://www.nasa.gov/mission_pages/kepler/spacecraft/index.html

[E13] Figure 4.1: ESO - Paranal Observatory.
https://www.eso.org/public/archives/images/screen/vlt.jpg

[E14] Figure 4.2: Description of Kepler devices.
https://www.universetoday.com/wp-content/uploads/2019/08/photometer_labels-768x837.jpg

[E15] MAST : Mikulski Archive for Space Telescopes.
https://mast.stsci.edu/portal/Mashup/Clients/Mast/Portal.html

[E16] Figure 1.1: Eclipsing binary light curve.
https://cdn.sci.esa.int/sci-images/be/eclipsing_binary.jpg

[E17] Figure 1.3: Hall, P. D., 2016 Contours of the Roche potential.
https://upload.wikimedia.org/wikipedia/commons/8/83/Roche_potential_contours_q%3D1.svg

[E18] Figure 2.1: Lagrange points.
https://www.researchgate.net/publication/379176584/figure/fig1/AS:11431281234044482@1712206133864/Position-of-the-Lagrange-points-L-1-to-L-5-Source-NASA.jpg

[E19] Sloan Digital Sky Survey data release 12.
https://skyserver.sdss.org/dr12/en/tools/toolshome.aspx

Appendix

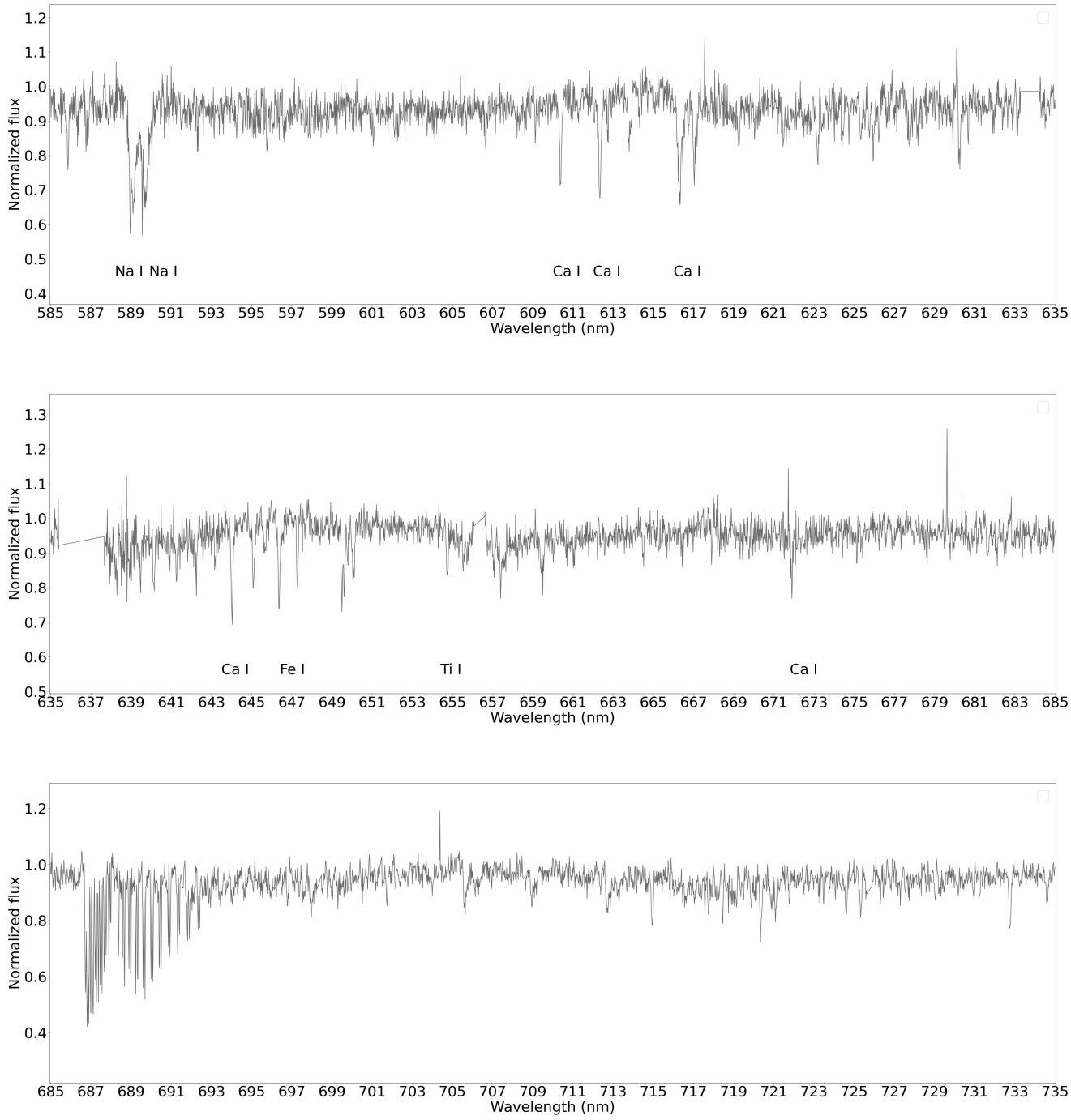

Figure 6.33: Spectral lines identification of GD 803 in 20 VIS spectrum.

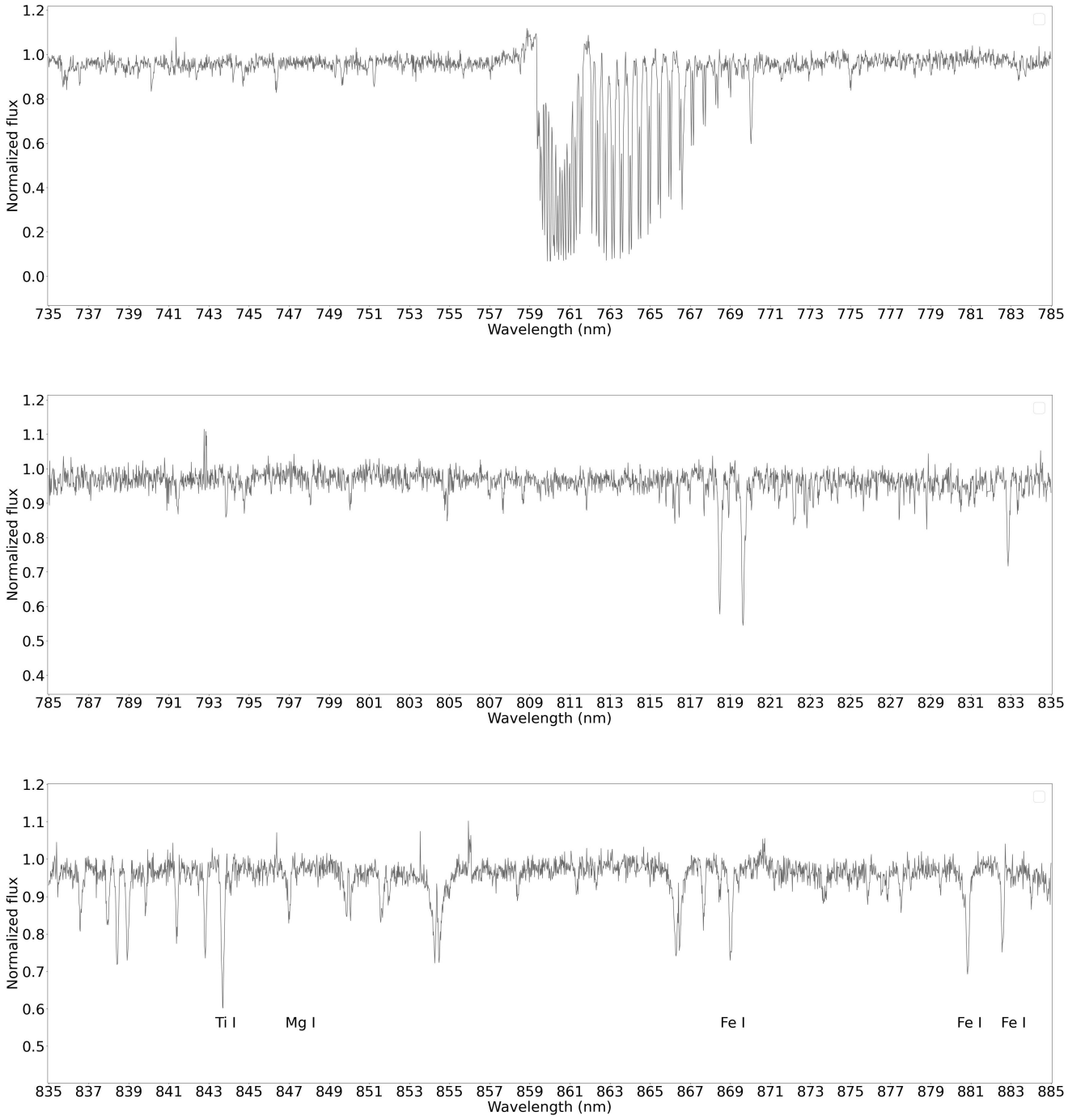

Figure 6.34: Spectral lines identification of GD 803 in 20 VIS spectrum - continued.

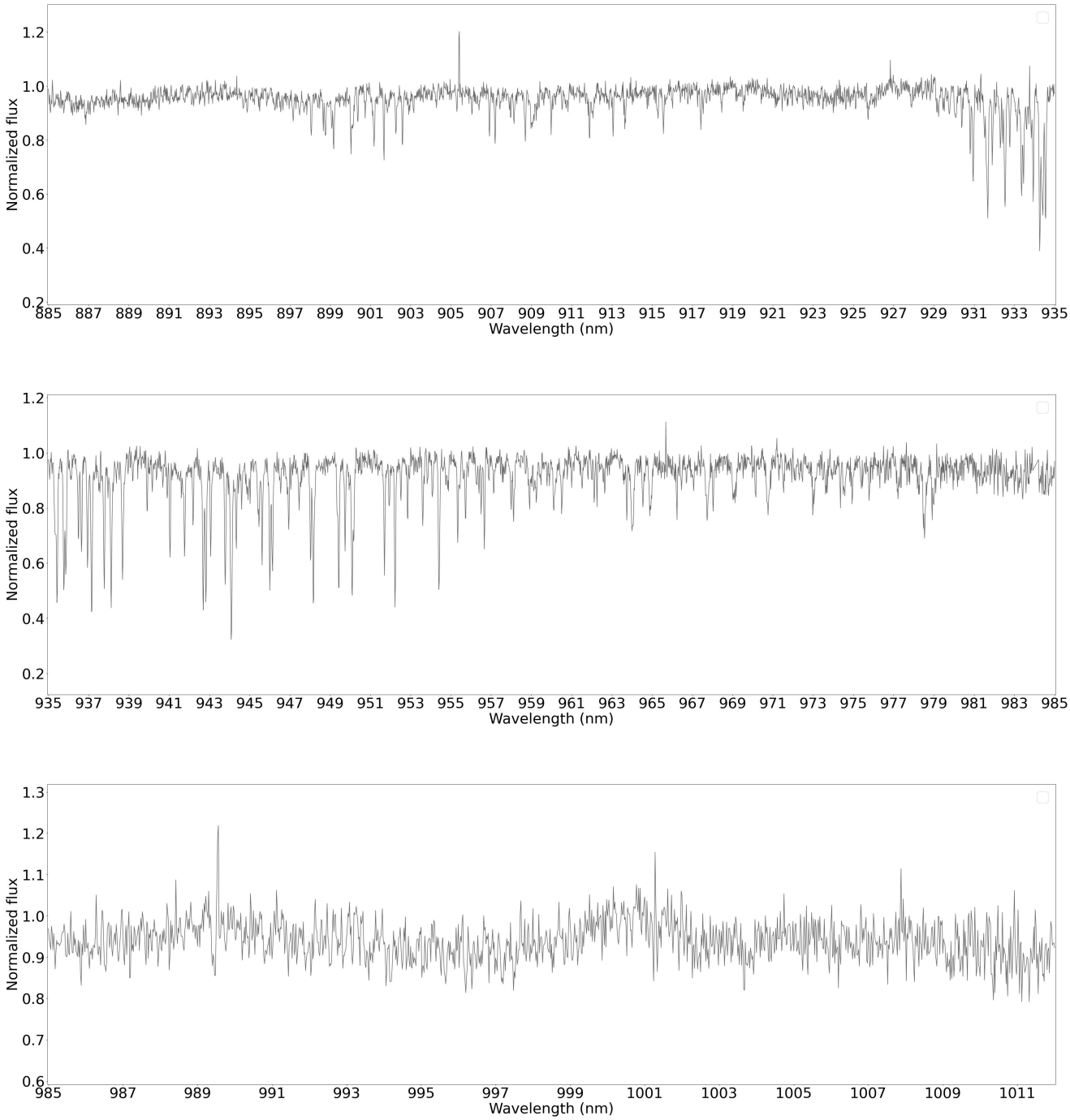

Figure 6.35: Spectral lines identification of GD 803 in 20 VIS spectrum - continued.

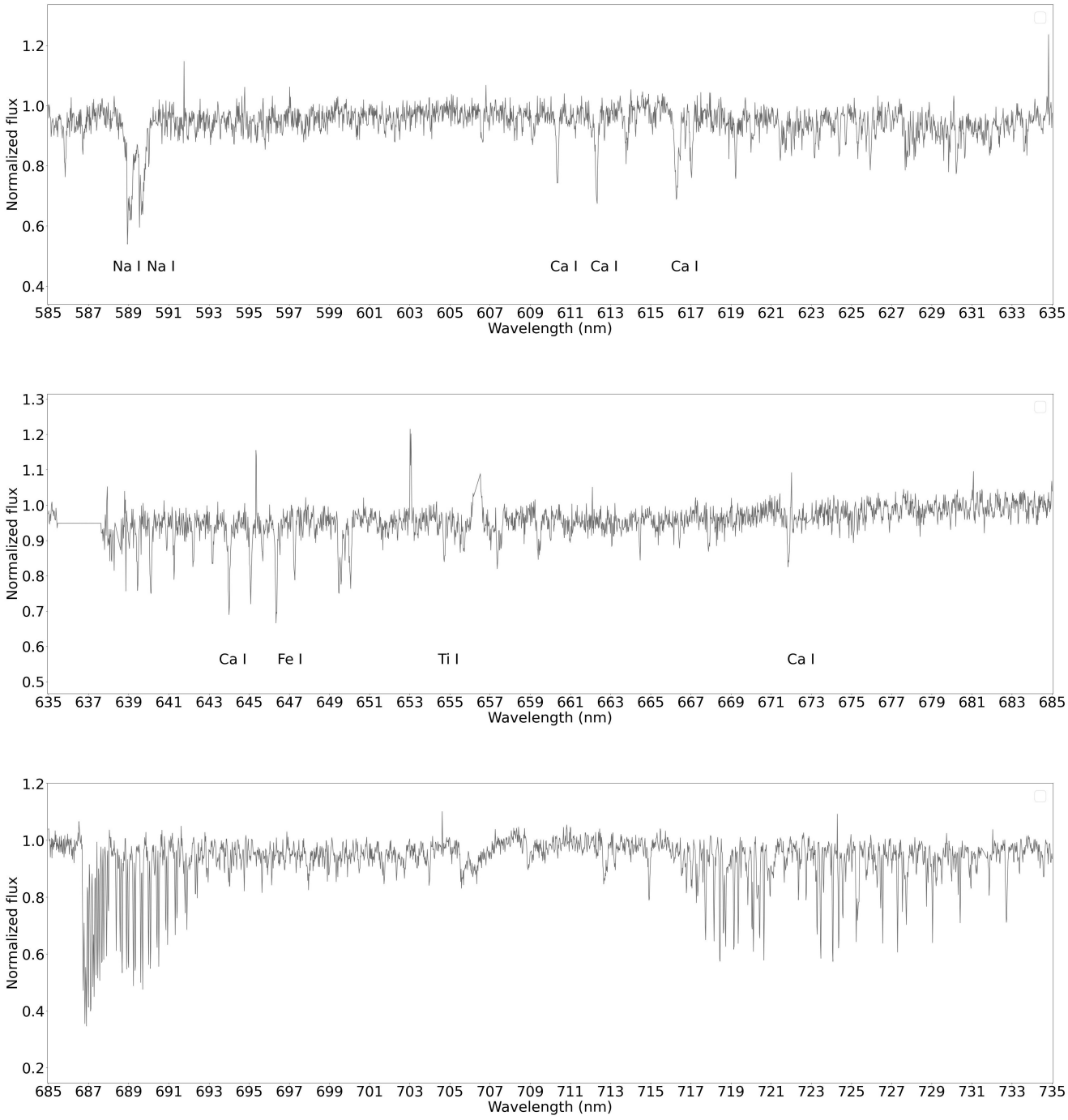

Figure 6.36: Spectral lines identification of GD 803 in 23 VIS spectrum.

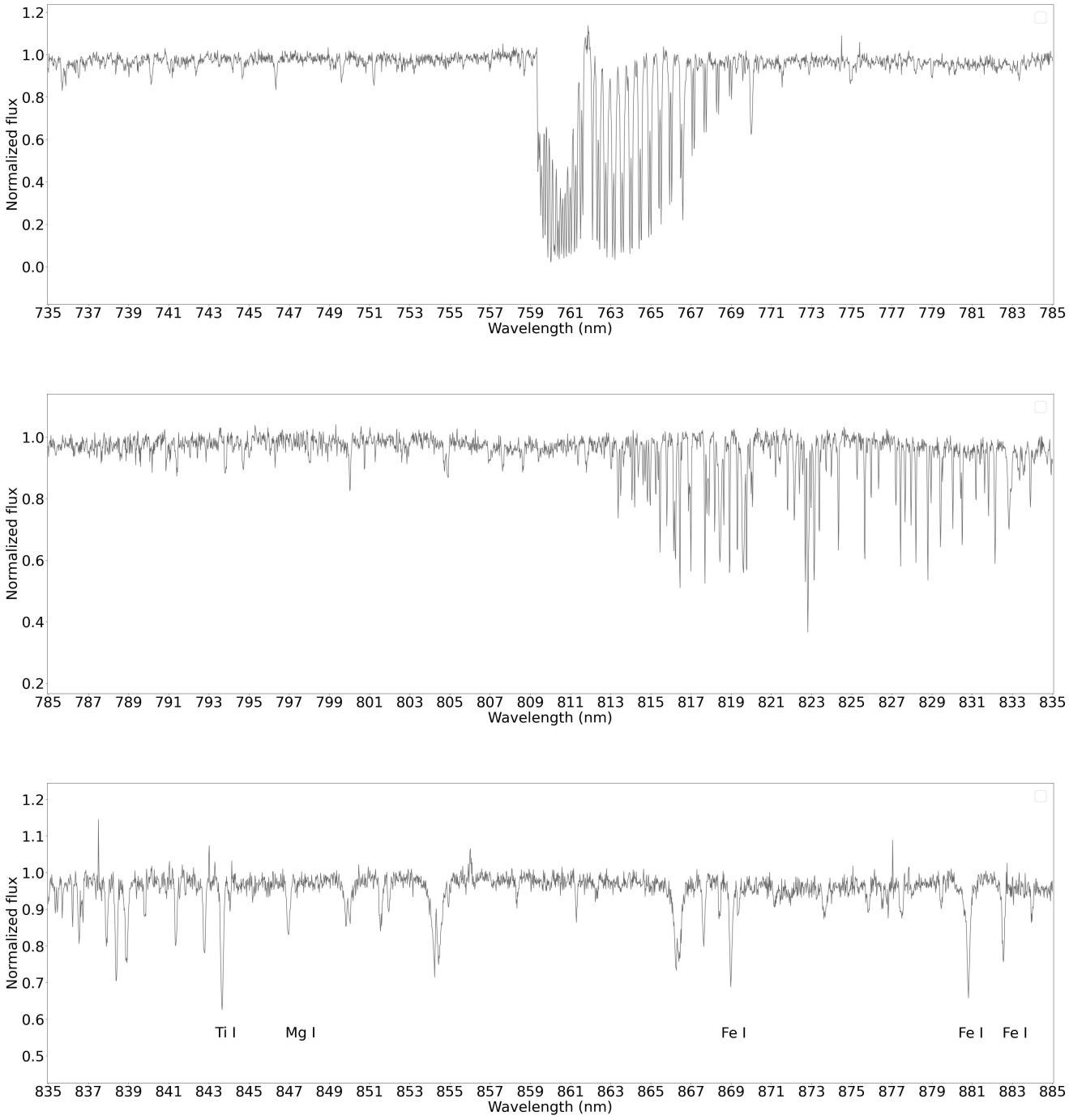

Figure 6.37: Spectral lines identification of GD 803 in 23 VIS spectrum - continued.

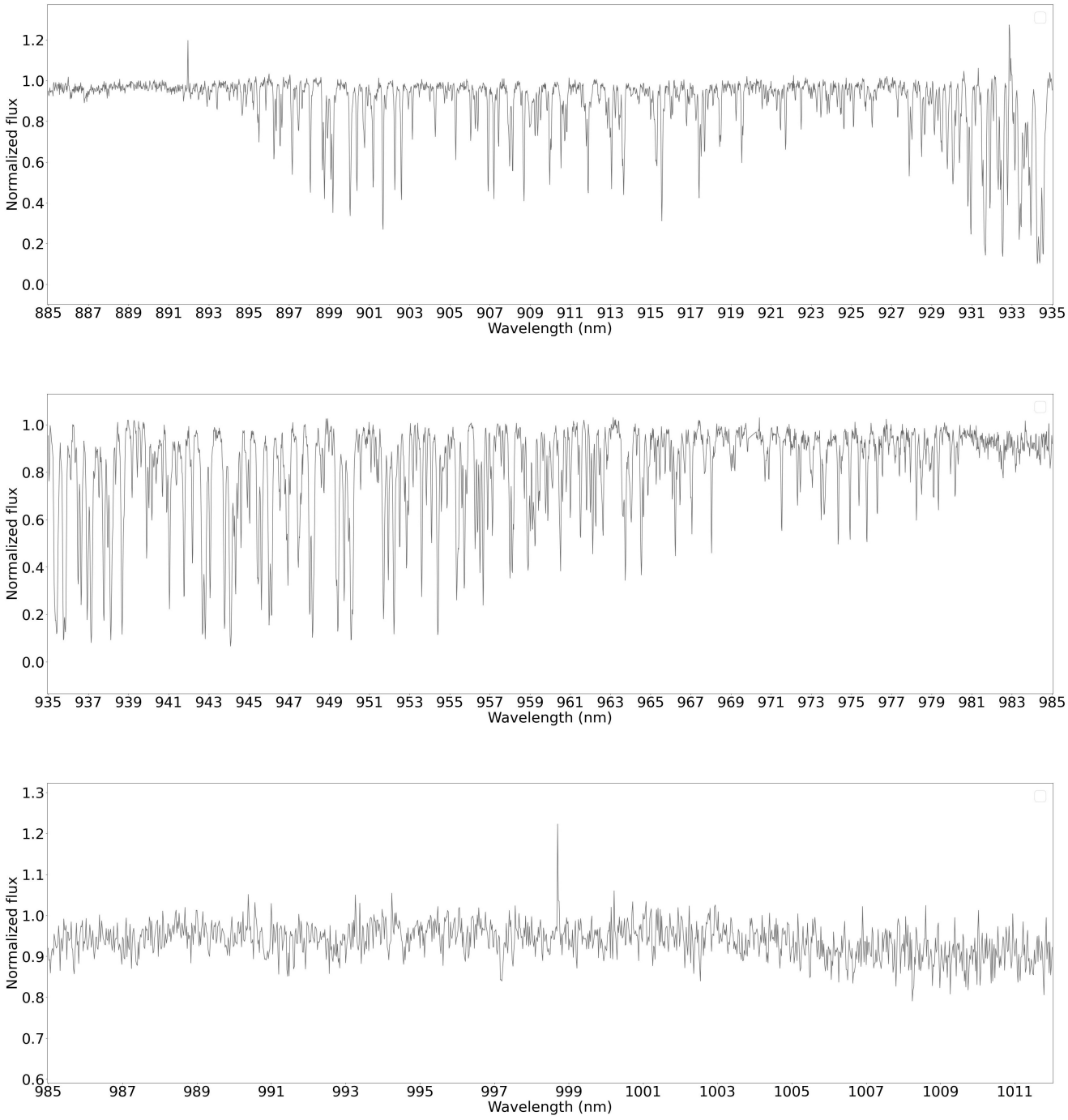

Figure 6.38: Spectral lines identification of GD 803 in 23 VIS spectrum - continued.

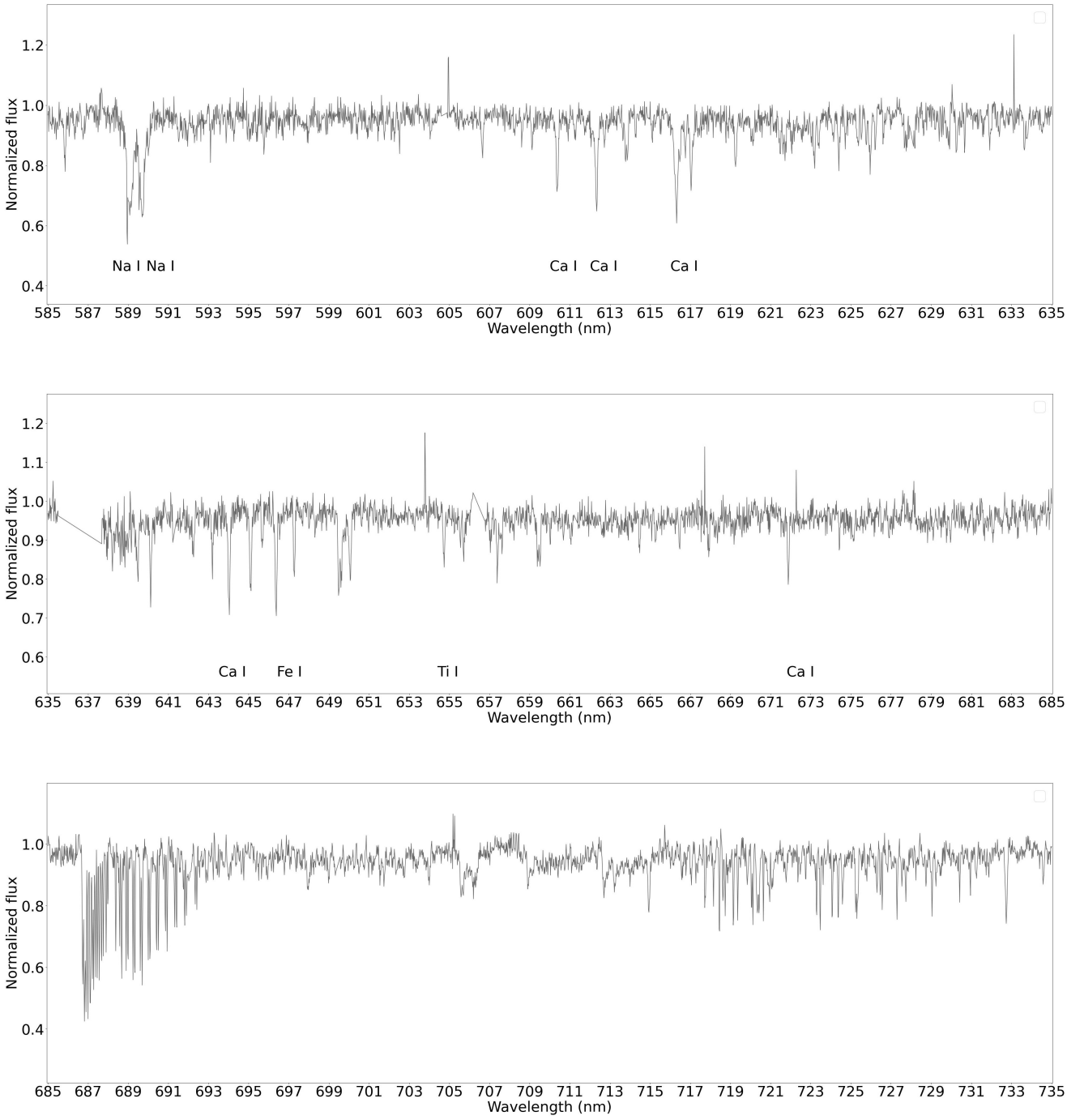

Figure 6.39: Spectral lines identification of GD 803 in 26 VIS spectrum.

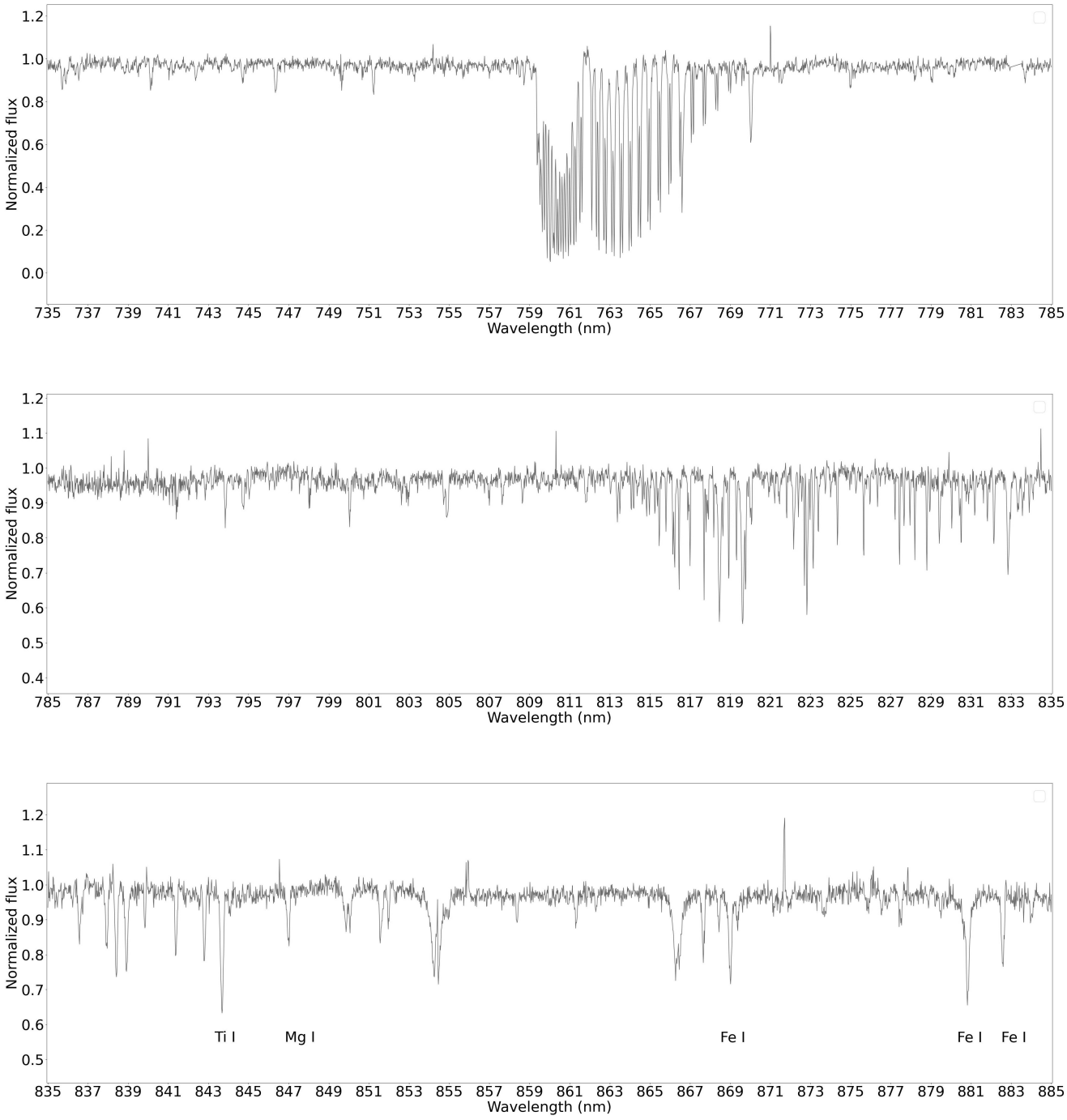

Figure 6.40: Spectral lines identification of GD 803 in 26 VIS spectrum - continued.

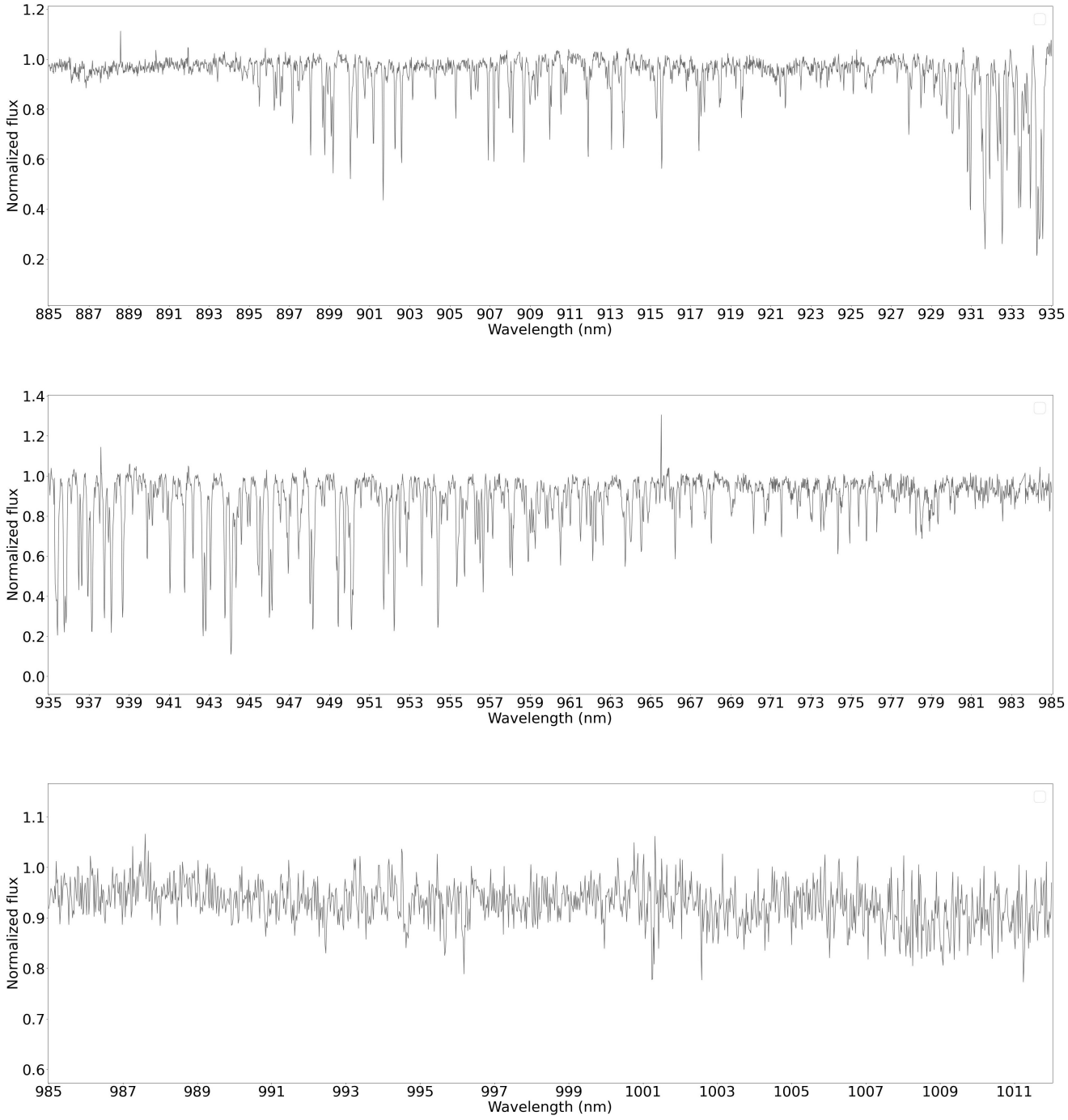

Figure 6.41: Spectral lines identification of GD 803 in 26 VIS spectrum - continued.

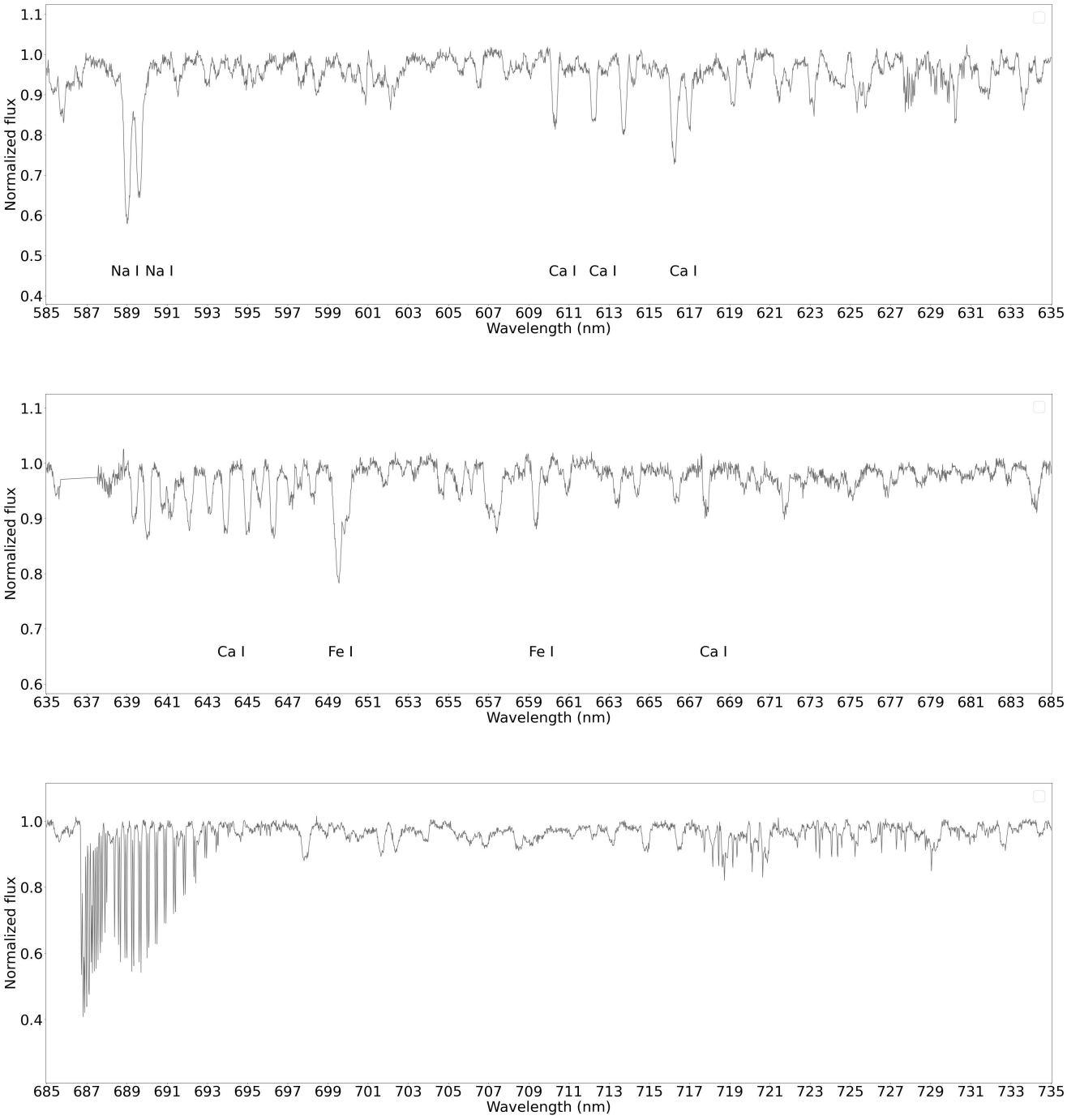

Figure 6.42: Spectral lines identification of BD+08 102 in 6 VIS spectrum.

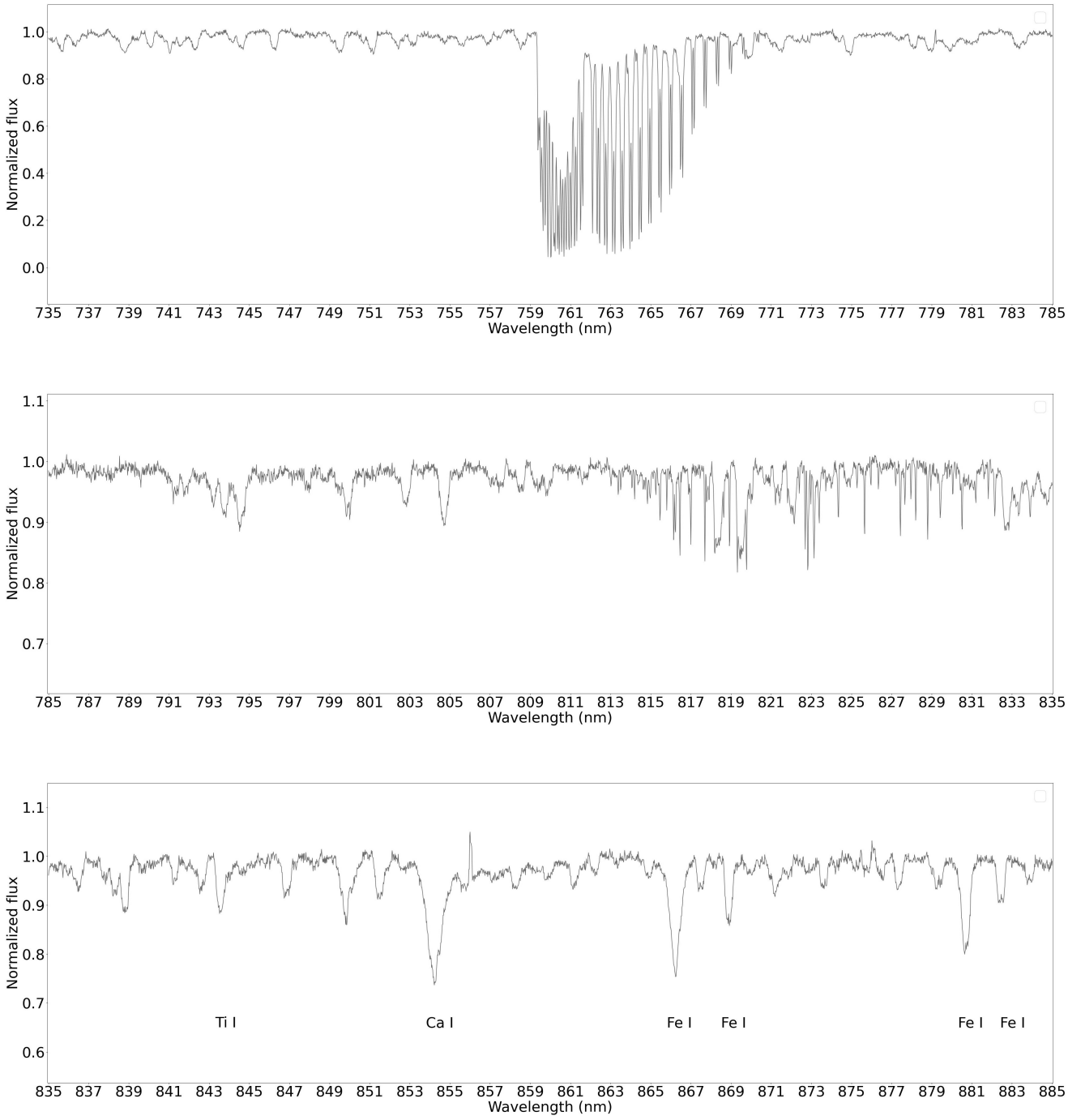

Figure 6.43: Spectral lines identification of BD+08 102 in 6 VIS spectrum - continued.

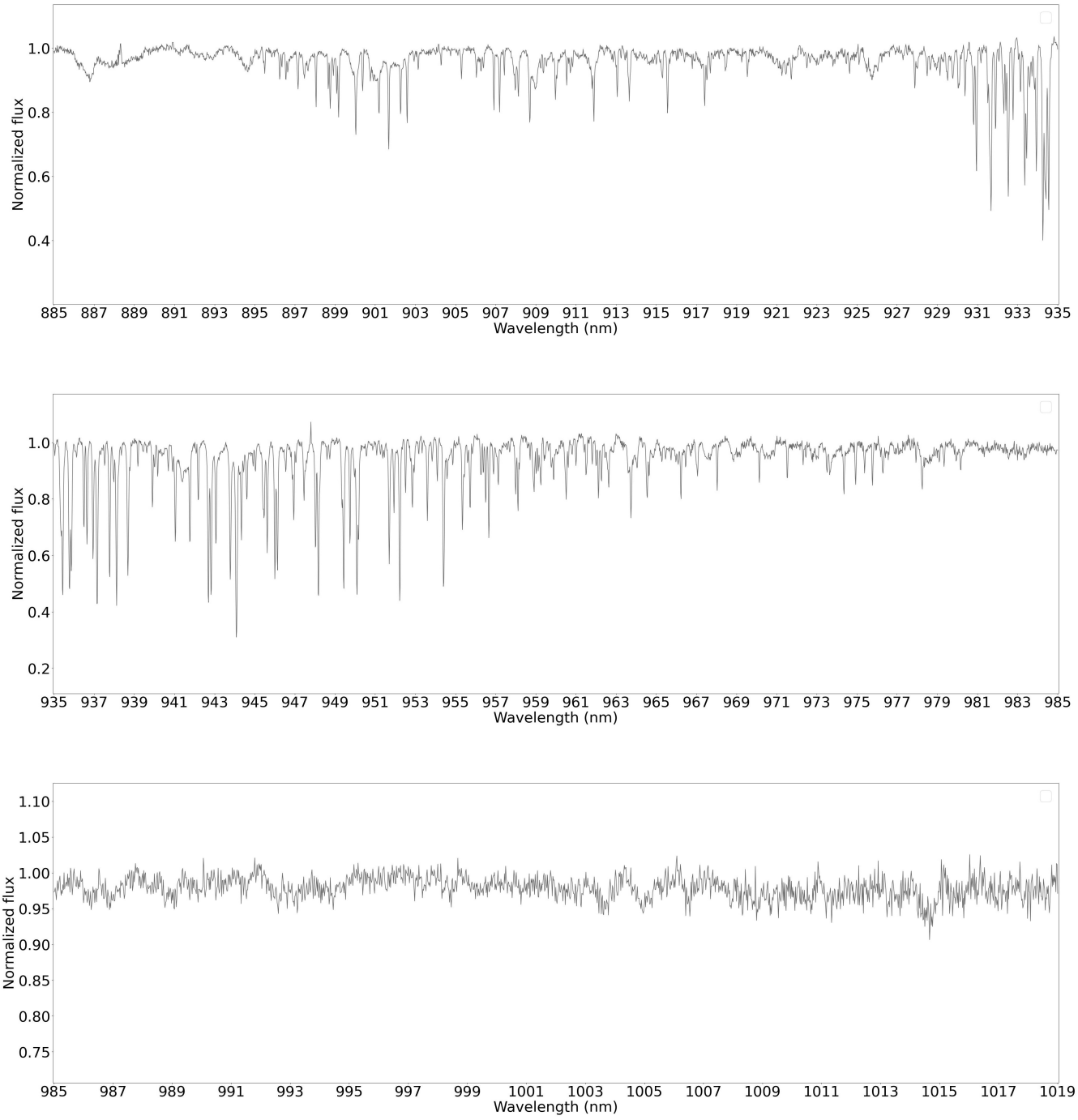

Figure 6.44: Spectral lines identification of BD+08 102 in 6 VIS spectrum - continued.

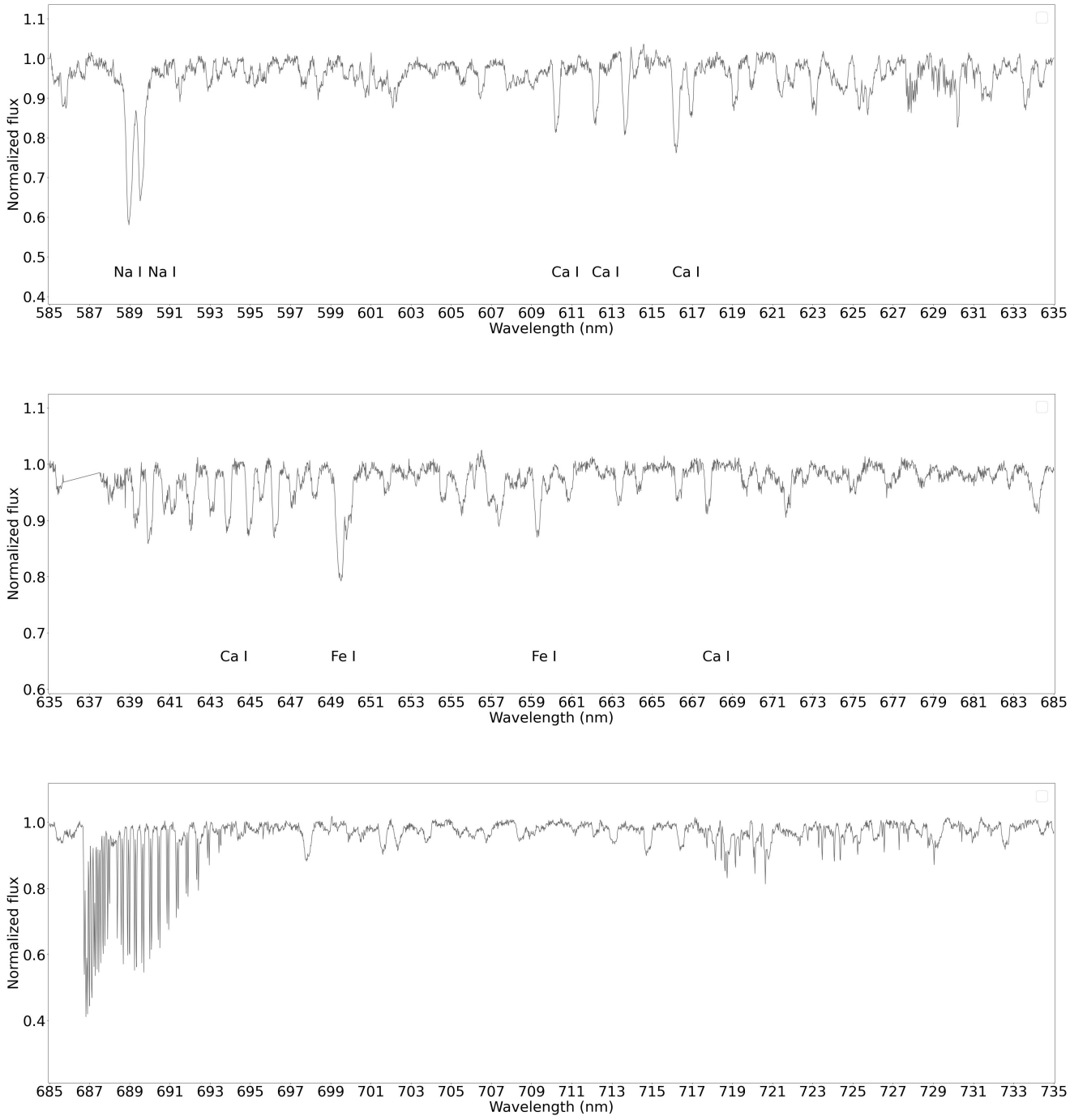

Figure 6.45: Spectral lines identification of BD+08 102 in 9 VIS spectrum.

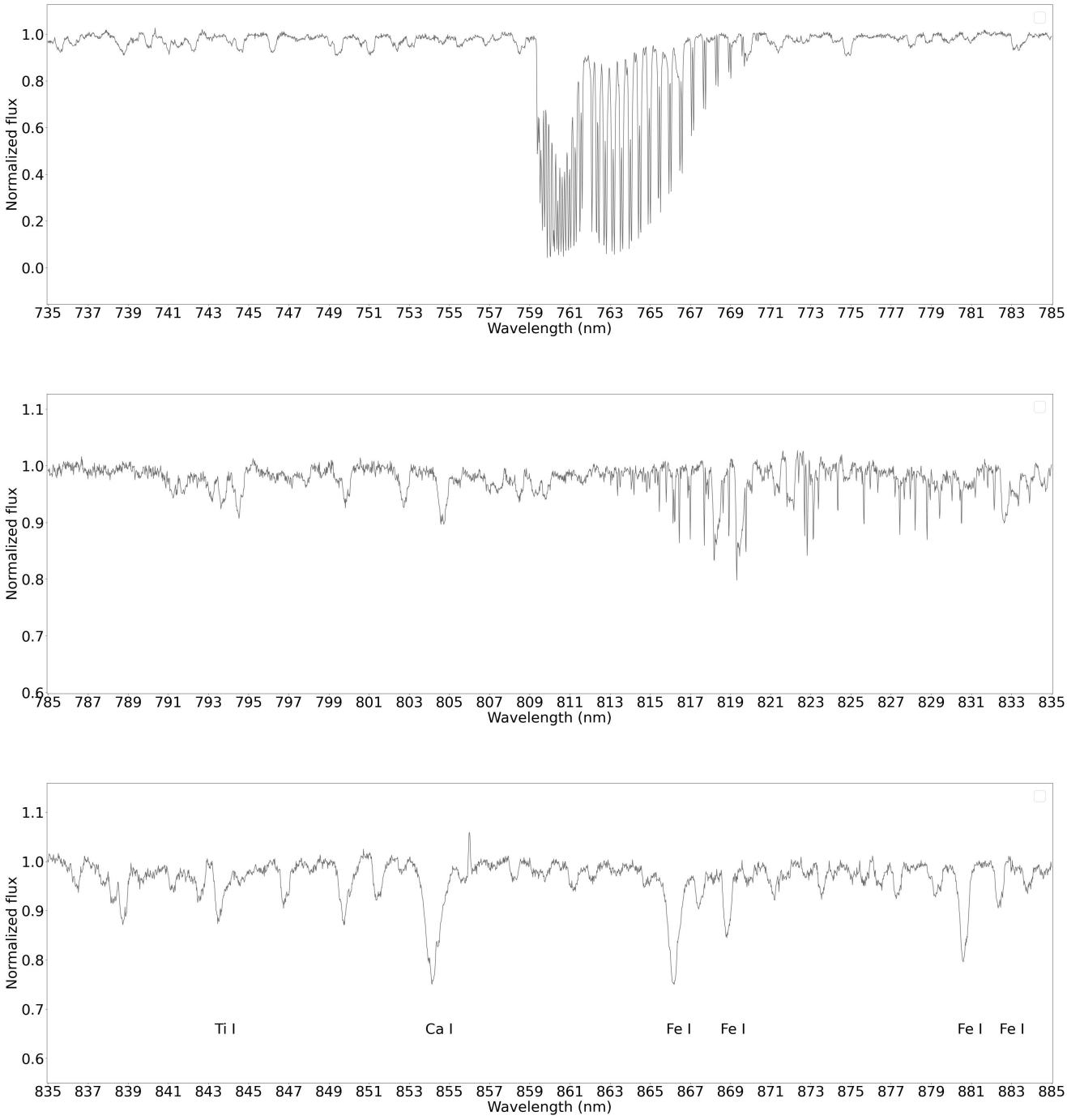

Figure 6.46: Spectral lines identification BD+08 102 in 9 VIS spectrum - continued.

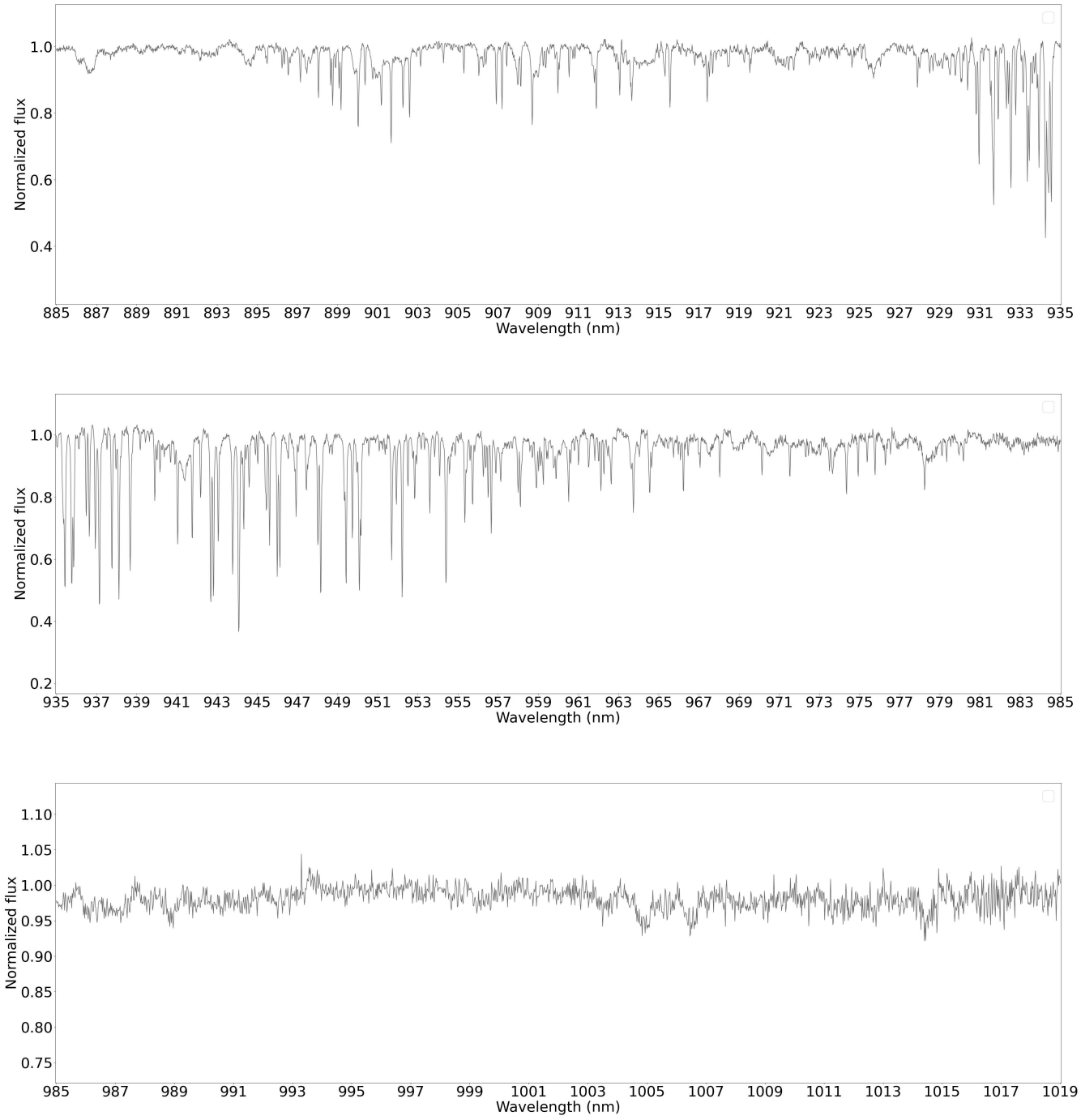

Figure 6.47: Spectral lines identification BD+08 102 in 9 VIS spectrum - continued.

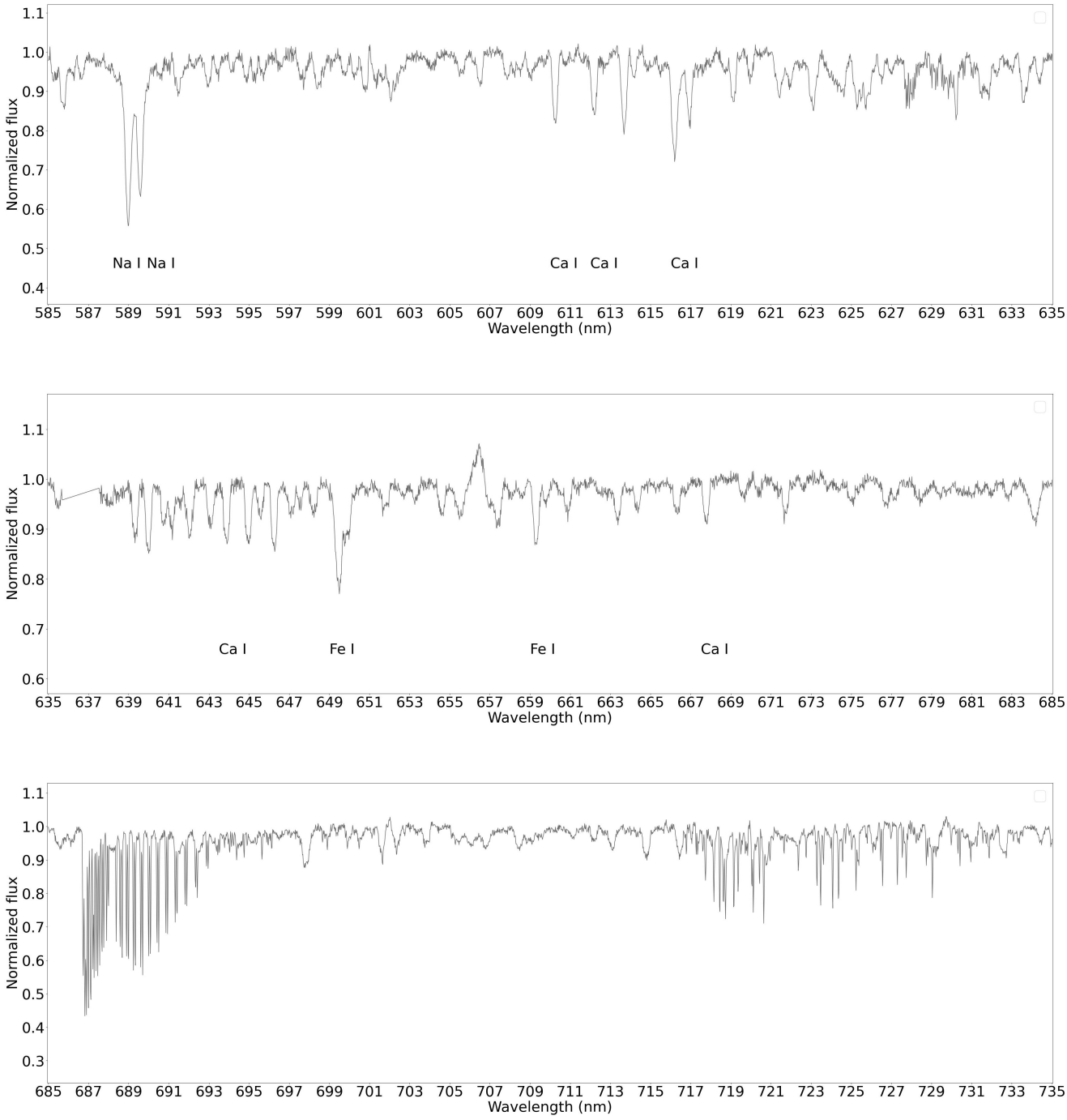

Figure 6.48: Spectral lines identification BD+08 102 in 12 VIS spectrum.

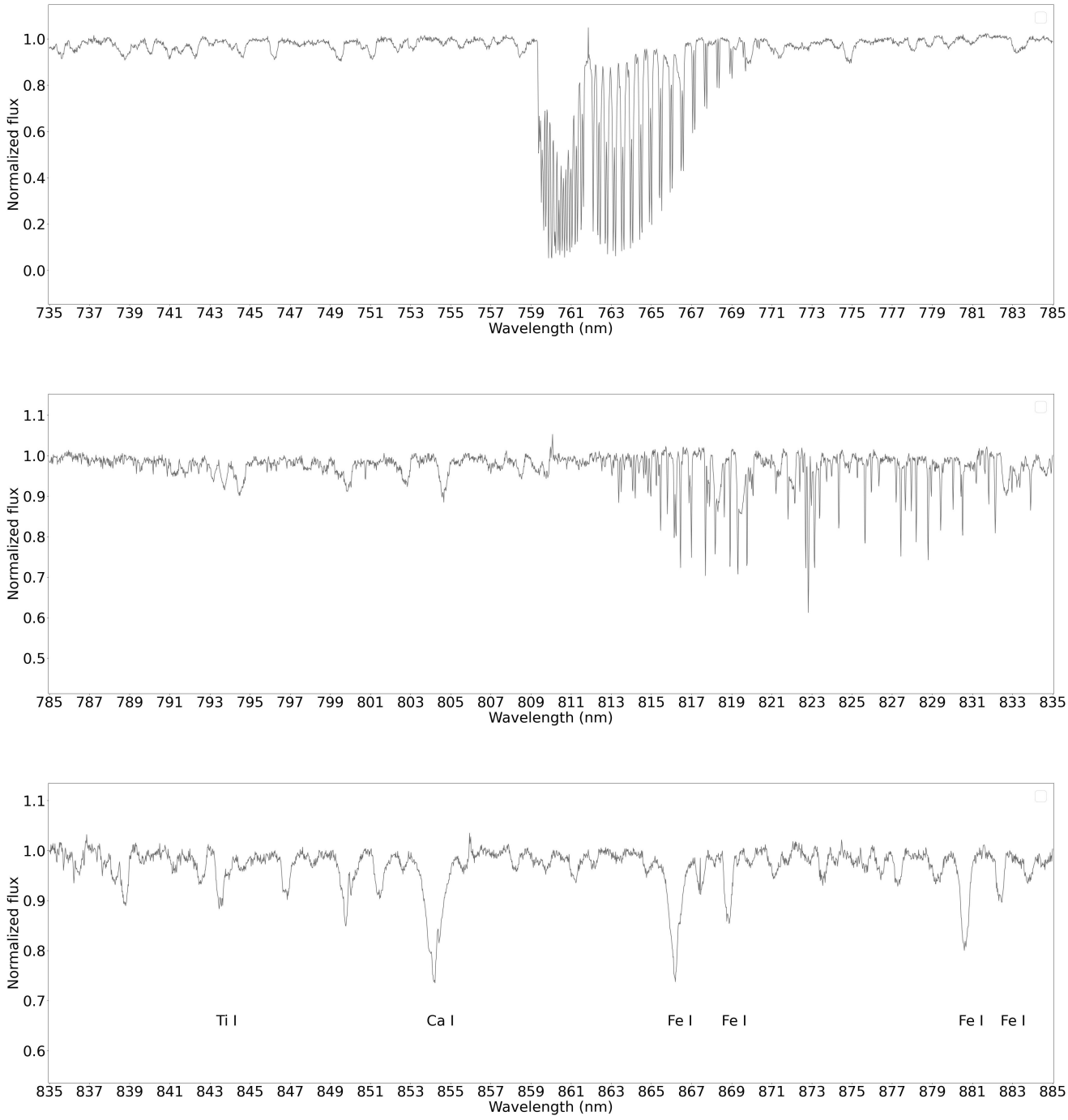

Figure 6.49: Spectral lines identification BD+08 102 in 12 VIS spectrum - continued.

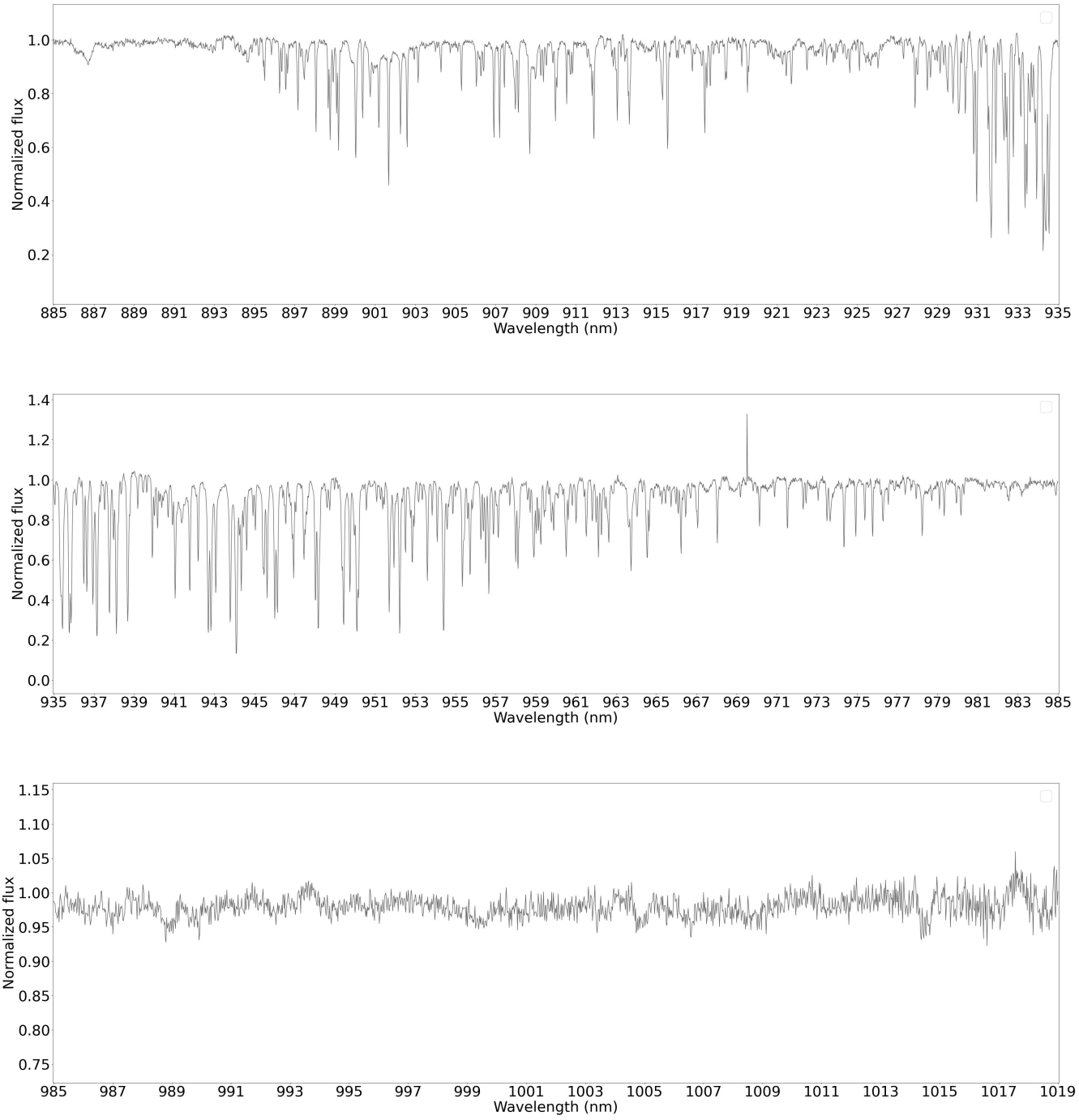

Figure 6.50: Spectral lines identification BD+08 102 in 12 VIS spectrum - continued.

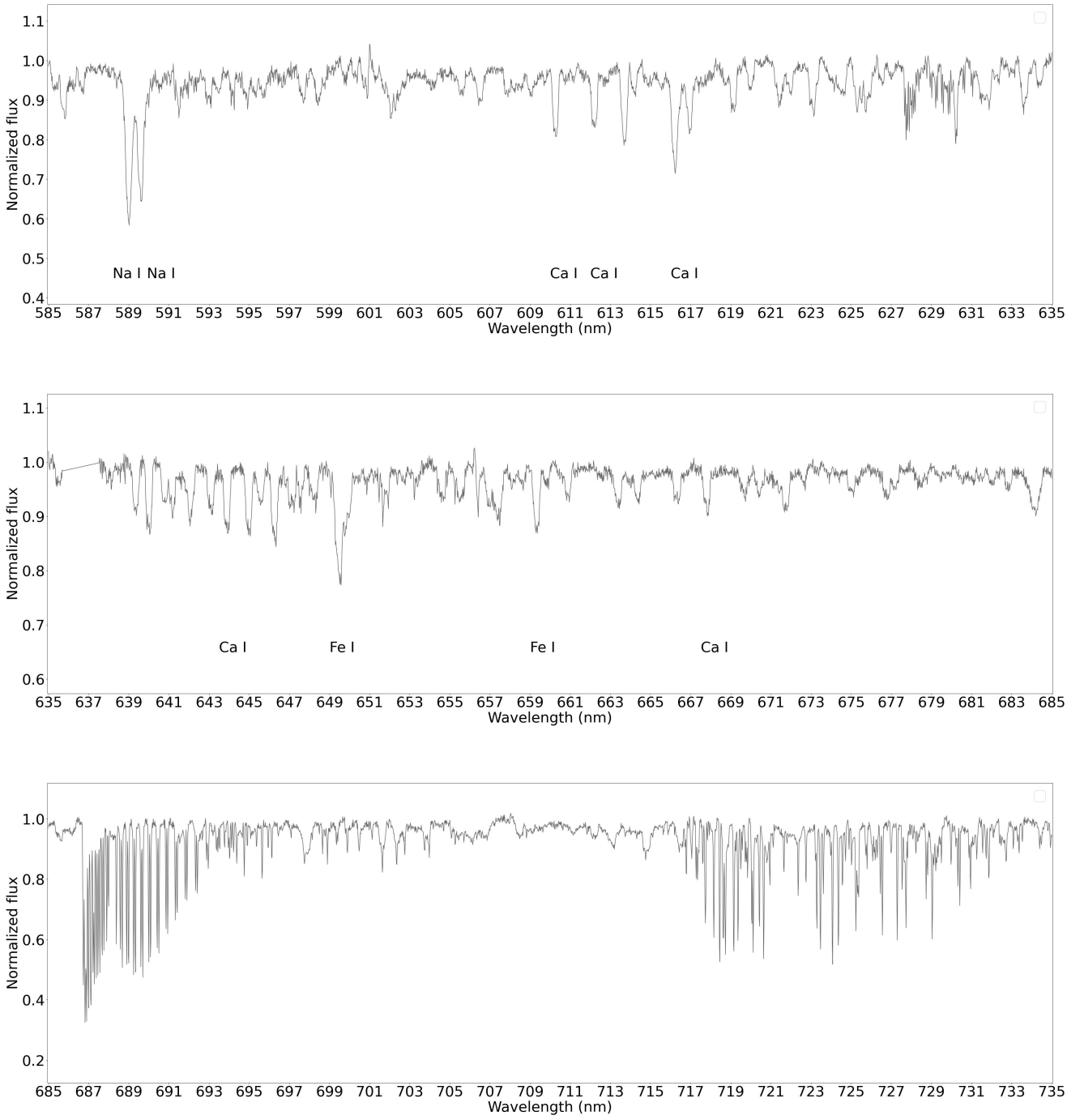

Figure 6.51: Spectral lines identification BD+08 102 in 15 VIS spectrum.

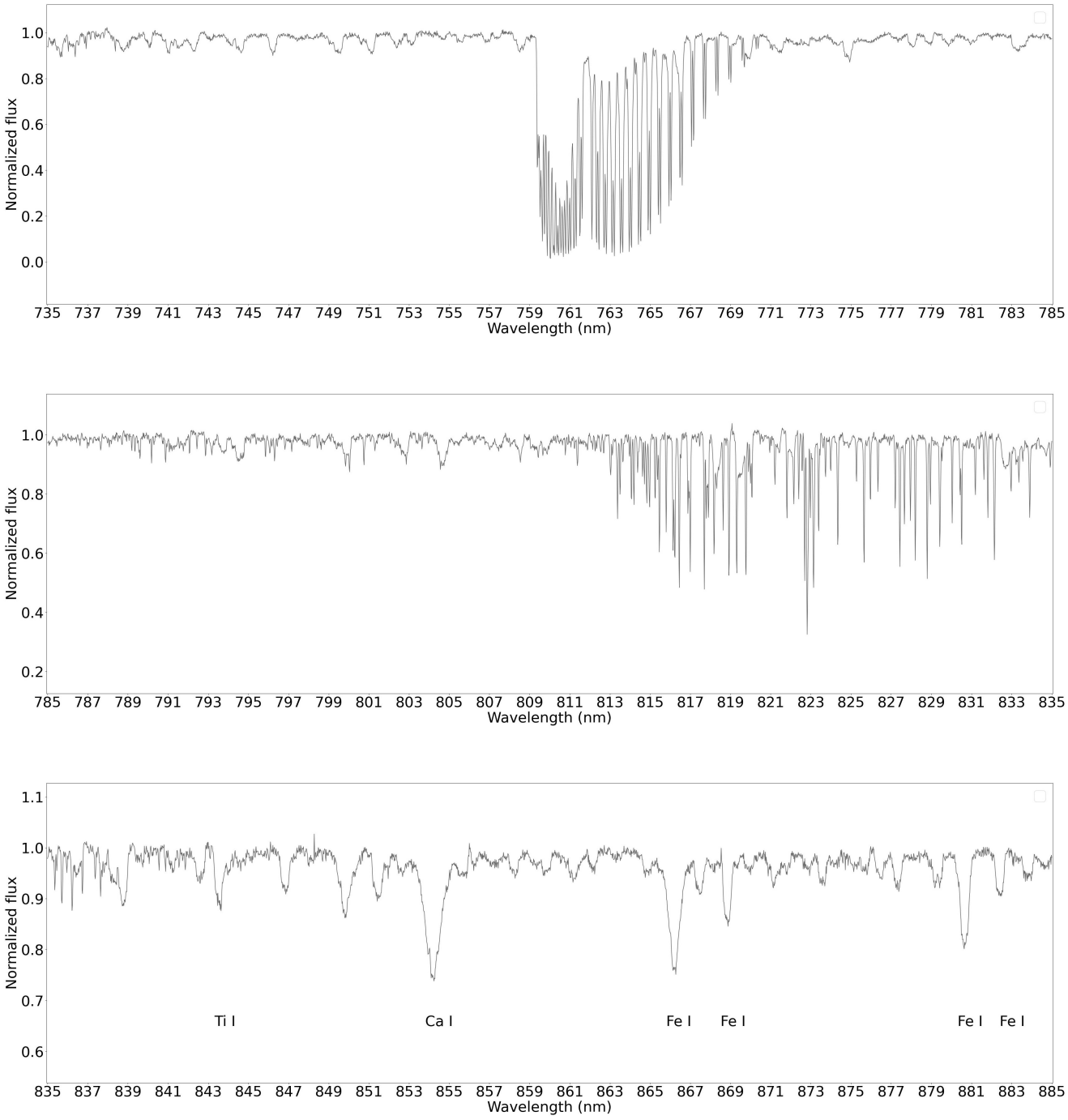

Figure 6.52: Spectral lines identification BD+08 102 in 15 VIS spectrum - continued.

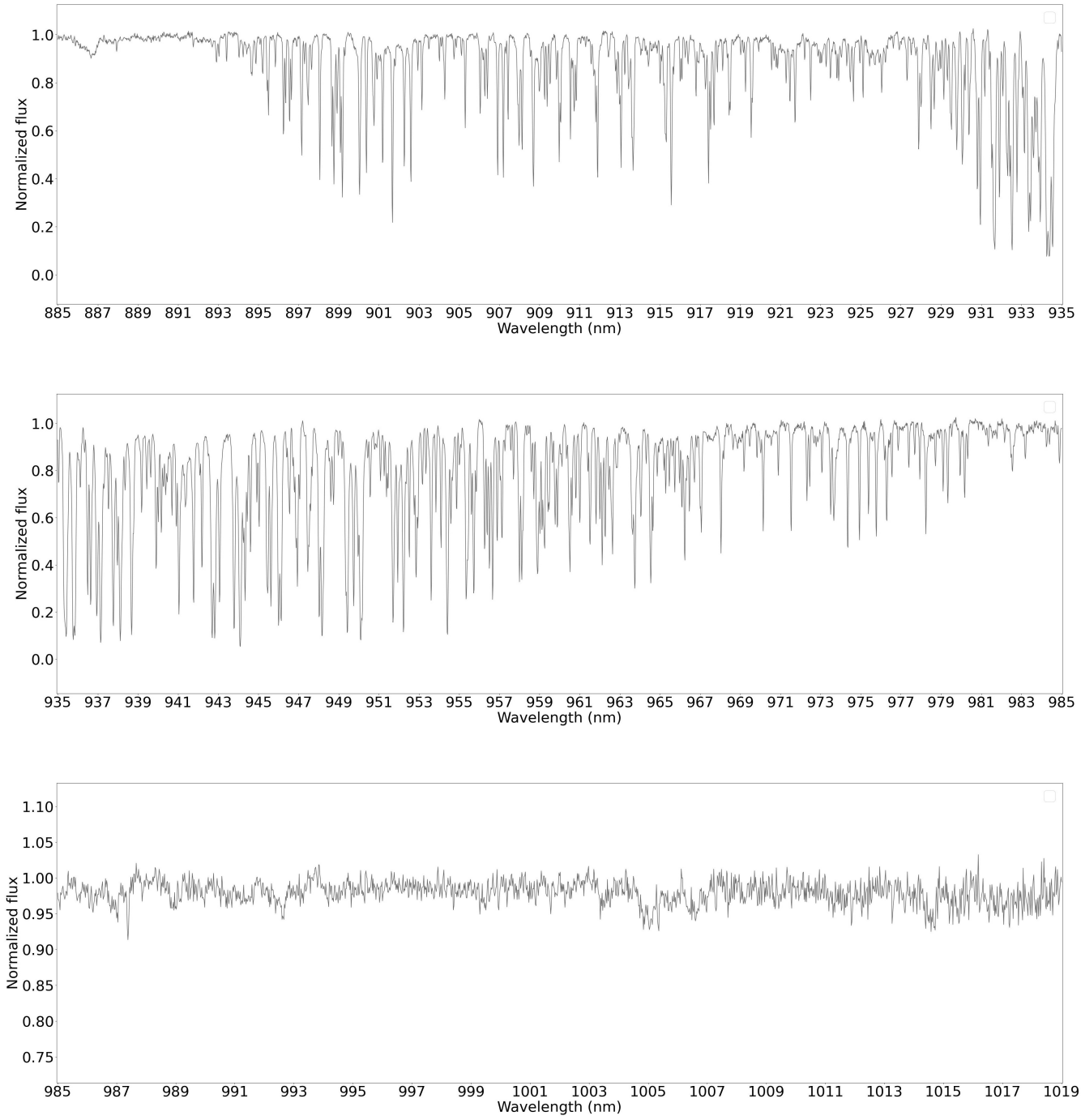

Figure 6.53: Spectral lines identification BD+08 102 in 15 VIS spectrum - continued.